Suzaku Study on the Ejecta of Galactic Evolved Supernova Remnants

Fumiyoshi Kamitsukasa
kamitsukasa@ess.sci.osaka-u.ac.jp

Department of Earth and Space Science, Graduate School of Science,
Osaka University,
1-1, Machikaneyama, Toyonaka, Osaka, 560-0043,
Japan

February 1, 2016

Abstract

Heavy elements in the Universe have been mainly generated by two types of supernova (SN) explosions. One is an explosive runaway of thermonuclear fusion (Type Ia SN), and the other is a gravitational core-collapse of massive stars (Core-collapse SN). A Type Ia SN produces a large amount of intermediate mass (Si–Ca) and Fe-group elements, whereas the major products of a core-collapse SN are light elements (C–Mg). Observation of optically-thin plasmas formed in supernova remnants (SNRs) is the most direct approach to understand these explosion mechanisms and nucleosynthesis.

In this thesis, we present the *Suzaku* study on the ejecta of the Galactic evolved SNRs, G292.0+1.8, G290.1−0.8, G272.2−3.2, and 3C397. Because SNRs consist of ejecta expelled from progenitors and interstellar medium (ISM) swept-up by blast waves, it is essential to discriminate these two components. In order to perform it, we employ the high quality X-ray spectra with *Suzaku*/XIS.

Thanks to the high detection efficiency of *Suzaku*, we discover Fe K-shell line emissions from G292.0+1.8 and G272.2−3.2 for the first time. Analyzing such high-quality spectra, we successfully separate the ejecta from the ISM component in three of above four SNRs (G292.0+1.8, G272.2−3.2, 3C397). The abundances and masses of the ejecta measured indicate a core-collapse origin for G292.0+1.8, but a Type Ia origin for G272.2−3.2. We cannot distinguish the explosion type of 3C397 because the abundances of light elements favor a core-collapse origin, while those of Fe-group elements favor a Type Ia origin. Although we cannot separate the ejecta from the ISM in the spectrum of G290.1−0.8, the abundances suggest a core-collapse origin for G290.1−0.8.

Combining our results with previous studies on other Galactic SNRs, we confirm that the abundances of light elements relative to intermediate mass elements in core-collapse SNRs are 10 times larger that those of Type Ia SNRs. The ejecta masses of core-collapse SNRs are also about 10 $M_{\odot}$, while those of Type Ia SNRs are about 1 $M_{\odot}$. On the other hand, the ionization ages of the Fe ejecta in the Type Ia SNRs are 15 times lower that those of the Si ejecta, while those in the core-collapse SNRs are roughly equal to each other. It indicates that the ejecta of Type Ia SNRs keep the stratified structure, whereas those of core-collapse SNRs are well mixed by a convection that maybe due to a hydrodynamical instability.

We discover a recombining plasma (RP) in the ejecta-dominant regions of G290.1−0.8. Including the RP SNRs discovered so far, we investigate a correlation between the distribution of RPs and ISM. We then find that the RPs become prominent toward the contact regions with cold molecular clouds. The plasma temperatures also decrease toward the contact regions. These facts clearly indicate that the RPs are formed with a thermal

conduction cooling by molecular clouds.

Contents

Chapter 1

Introduction

Supernovae (SNe) originate from two types of progenitors. One is an explosive runaway of thermonuclear fusion (Type Ia SN), and the other is a gravitational core-collapse of massive stars (Core-collapse SN). A Type Ia SN produces a large amount of intermediate mass (Si–Ca) and Fe-group elements, while the major products of a core-collapse SN are light elements (C–Mg). These two types of SNe have played a key role for the chemical evolution of the Universe. There are about 300 traces of SNe, i.e. supernova remnants (SNRs), in our Galaxy. These SNRs give us important opportunities to study the local population of Type Ia and core-collapse SNe, because the Galactic SN rate is relatively small ($2.5^{+0.8}_{-0.5}$ SNe per century; Tammann et al. 1994). In addition, SNRs are extended optically thin sources, which allow us to measure the amount and distributions of heavy elements directly, providing the insight for the basic natures of SNe, e.g., nucleosynthesis, explosion mechanisms, and circumstellar environments.

An X-ray spectroscopy is particularly essential for the observation of SNRs because the energies of fluorescent line emissions of main products are in the soft X-ray band (0.1–10 keV). SNRs have been extensively studied since the beginning of the X-ray astronomy. As a result, several typing methods on their progenitors are proposed. Observing the ejecta dominated SNRs in the Large Magellanic Cloud with *ASCA*, Hughes et al. (1995) showed that it is possible to distinguish their progenitors with the spectral feature around $E = 1$ keV; SNRs dominated by Fe L-shell emission with weak O and Ne lines are likely Type Ia, while those of vice versa are likely core-collapse origins. Lopez et al. (2009, 2011) argued that Type Ia SNRs have more symmetric morphology than those of core-collapse with the high resolution images by *Chandra*. Their result is consistent with the expectation that core-collapse SNRs are located in dense and complex environments where massive stars are born. Yang et al. (2009, 2013) focused on the nucleosynthesis yields in the Fe K-shell band (5–8 keV). They suggested that the ratio of the equivalent width (EW)

of the Cr emission line to that of Fe ($\gamma_{\rm Cr/Fe} \equiv {\rm EW(Cr)/EW(Fe)}$) provides a constrain on the SNR progenitors; SNRs with $\gamma_{\rm Cr/Fe} > 2\,\%$ favors a Type Ia origin, whereas SNRs with $\gamma_{\rm Cr/Fe} < 2\,\%$ could be of either core-collapse or Type Ia origin. Yamaguchi et al. (2014) also showed that the Fe K-shell lines of Type Ia candidates have lower center energies (6.4–6.5 keV) than those of core-collapse (6.6–6.7 keV). They considered that the Fe-K center energies, reflecting their ionization states, correlate with the ambient densities, characteristic for each type of SNRs.

In spite of these studies, the progenitor types of the Galactic SNRs are not identified in most cases. It is because the ejecta materials of SNe are not successfully extracted from the remnants that are contaminated by the interstellar medium (ISM) swept-up by blast waves. Although the nucleosynthesis yields in the Fe K-shell bands suggest the ejecta origin for these elements, the number of SNRs showing significant Fe-K line emission is small (only 16 sources out of 282 in our Galaxy). Therefore, we can not rely on this method. Thus, it is necessary to separate the ejecta from the ISM component in the broadband X-ray spectra. In order to perform it, it is essential to have a high sensitivity detector for the line emission. *Suzaku*, the Japan's fifth X-ray observatory, has the most suitable instrument, XIS, which has good energy resolution, high detection efficiency, and low background level for diffuse sources in the soft X-ray band of 0.4–10 keV.

In this thesis, we perform the X-ray spectroscopy on several Galactic SNRs utilizing the full effective band of *Suzaku*/XIS. Based on the careful data reduction and analysis, including the separation of the ejecta from the ISM, we discuss the connections between the ejecta and progenitor types. This thesis consists of the following components. We review the current understanding of the physical processes in the SNR in chapter 2 and the basic characteristics of the instruments on board *Suzaku* in chapter 3. In chapters 4–7, we present the analysis results on individual SNRs, G292.0+1.8, G290.1−0.8, G272.2−3.2, and 3C397. Combining these results with other previous studies, we discuss and summarize their indications in chapter 8 and 9.

Chapter 2

Review of Supernova Remnants

2.1 Supernovae

Supernovae (SNe), explosions of stars at the end of their lifetimes, are one of the most energetic events in the Universe. Their explosion energies typically reach $\sim 10^{51}$ erg, which is comparable to the rest mass energy of Jupiter. SN explosions are estimated to occur per $\sim$ 30yr in our Galaxy (Tammann et al. 1994). The shock waves generated by the explosions induce the star formation through the compression of the surrounding medium. SN explosions also synthesize heavy elements, and release them into the interstellar space. Therefore, SNe play an important role in the cycle of matters in the Universe. In this section, we summarize the basic characteristics of SNe.

2.1.1 Classification

The SNe have been observationally classified with their early-phase optical spectra and light curves (figure 2.1). The basic criterion of the classification is the absence (Type I) or presence (Type II) of absorption lines of Hydrogen Balmer series in the optical spectra. Such difference of the SN spectra was pointed out by Zwicky, Baade, and Minkowski in the late 1930s, and Minkowski (1941) first introduced this classification. Each type of SNe is further divided into several subclasses.

Type I SNe have three subclasses: Type Ia, Ib, and Ic. Type Ia and other two subclasses are classified according to the presence or absence of a strong Si II absorption feature at 6150 Å. Type Ib and Ic are further distinguished by the presence or absence of He absorption lines. On the other hand, the sub-classes of Type II SNe, Type II-P and II-L, are classified by the shape of light curves. Type II-P light curves contain "plateau", in which the optical brightness is almost constant for $\sim$ 100 days after the maximum

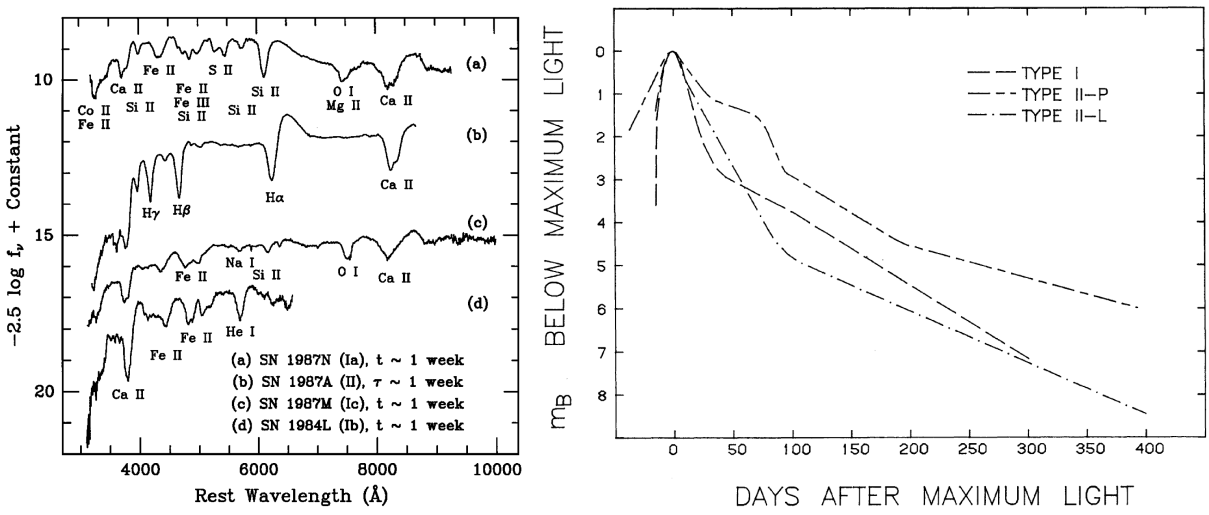

Figure 2.1: Left: the early-phase optical spectra of SNe (Filippenko 1997). Right: the mean blue light curves of Type I, II-P, and II-L SNe (Doggett & Branch 1985).

brightness, whereas those of Type II-L linealy decline in magnitude. Type II SNe also have another subclass, Type IIb, which is the intermediate class between Type Ib and Type II. Their optical spectra at the initial phase are very similar to those of Type II, but rapidly evolve to those of Type Ib.

The progenitors of Type Ia SNe are considered to be near-Chandrasekhar mass white dwars ($M \sim 1.4\,M_\odot$) , while Type II progenitors are massive stars ($M > 10\,M_\odot$). They are called thermonuclear SNe and core-collapse SNe, respectively, based on the explosion mechanisms. We describe some details of the explosion mechanisms in the following sections. Type Ib and Ic SNe are also thought to be core-collapse SNe because they have similar light curves as Type II and are preferentially observed in spiral galaxies and star forming regions. The lack of H absorption lines in the optical spectra indicates the loss of H-rich envelope likely due to the stellar wind from the progenitor stars. In the case of Type Ic, the stellar wind removes even He-rich layers of progenitor stars.

2.1.2 Type Ia Supernovae

Type Ia SNe are observed in all types of galaxies, also in the elliptical galaxies where the star formation has finished and no massive star remains. The lack of the hydrogen absorption lines in the Type Ia spectra also indicates that the progenitors have no hydrogen envelope. From these facts, thermonuclear explosion of C/O white dwarfs was believed as the most likely origin of Type Ia SNe.

Two major progenitor systems are currently proposed. One is the single-degenerate progenitor (Whelan & Iben 1973) where a white dwarf get the accretion from a main

sequence star or an evolved companion. The other is the double degenerate progenitor (Webbink 1984) where the violent merger of two white dwarfs takes place. In both systems, if the mass of white dwarfs exceeds the Chandrasekhar limit ($\sim 1.38\,M_{\odot}$), the core shrinks and reaches ignition temperature for the carbon fusion,

$$^{12}\mathrm{C} \ + \ ^{12}\mathrm{C} \rightarrow \begin{cases} ^{20}\mathrm{Ne} \ + \ ^{4}\mathrm{He} \\ ^{23}\mathrm{Na} \ + \ \mathrm{p} \\ ^{24}\mathrm{Mg} \ + \ \gamma \end{cases} \tag{2.1}$$

This reaction causes a thermonuclear runaway under high-pressure condition and releases enough energy to disrupt a white dwarf.

Three models are proposed for the way of the propagation of carbon burning: detonation, deflagration, and delayed detonation. In the detonation model (e.g., Arnett 1969), a supersonic shock wave propagates and causes an explosive nucleosynthesis (see section 2.1.4) in the white dwarf. However, this model, in which most of the white dwarf material is burned to iron-group elements, fails to reproduce the observed metal abundances of Type Ia SNe. It conflicts with the strong absorption line of Si observed in the optical spectra. In the deflagration model, the burning front propagates at subsonic speed. The subsonic burning front proceeds a nucleosynthesis by the convective motion, which carries the unburned material into the hot burning zone. Unlike the detonation model, since the deflagration model allows a part of the white dwarf to expand significantly before being burnt, a sufficient amount of intermediate elements (such as Si) is produced. This is needed to explain the Type Ia spectra. W7 model (Nomoto et al. 1984) is a well-known classical deflagration model. On the other hand, the pure deflagration model leaves some problem: it cannot reproduce the abundance stratification inferred from spectral evolution (e.g., Stehle et al. 2005) and also cannot reproduce the observed explosion energies. To account for these problems, the delayed detonation (DDT) model was proposed (Khokhlov 1991; Woosley & Weaver 1994). In the DDT model, the explosion starts as a deflagration, but turns to a detonation wave burning the remaining fuel into the intermediate mass elements. The DDT model can explain most of the nature of Type Ia SNe, although the turning mechanism from a deflagration to a detonation is still an open question.

2.1.3 Core-Collapse Supernovae

Core-collapse SNe originates in the massive stars with the main sequence masses of $M \geq 10M_{\odot}$. In these massive stars, the nucleosynthesis proceeds to produce Fe in the core and finally form an onion-like structure (figure 2.2) which leaves the trace of different burning stages. Since Fe is the most stable nuclei, the nuclear fusion in the core does not proceed

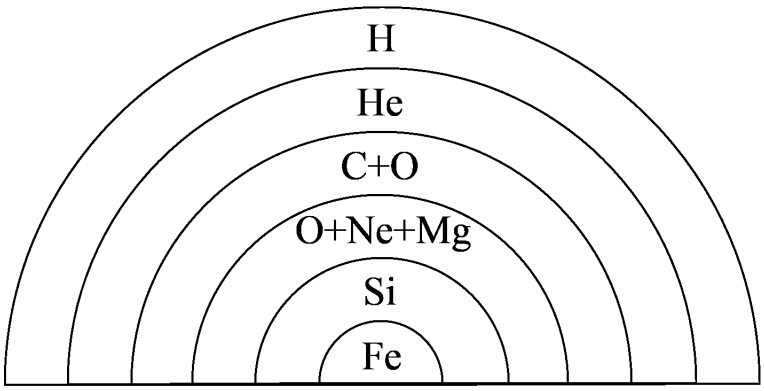

Figure 2.2: Onion-like structure in massive star just prior to core-collapse.

any more. The Fe is compressed and the temperature of the core exceeds $\simeq 3 \times 10^9$ K. Then, the following photo-disintegration of Fe nuclei takes place:

$$\begin{aligned} {}^{56}\mathrm{Fe} &\rightarrow 13\,{}^{4}\mathrm{He} + 4\mathrm{n} - 124.4\mathrm{MeV} \\ {}^{4}\mathrm{He} &\rightarrow 2\mathrm{p} + 2\mathrm{n} - 28.3\mathrm{MeV} \end{aligned}$$

Since this reaction absorbs the thermal energy, the core becomes to be unable to maintain the stellar gravity, then collapses into a neutron star (or a black hole).

The total energy of the gravitational collapse is $\sim 10^{53}$ ergs. Most of this energy is escaped in the form of neutrinos, which are confirmed with the detection by Kamiokande (Hirata et al. 1987) and Irvine-Michigan-Brookhaven (Bionta et al. 1987) Cherenkov detectors on SN1987A. On the other hand, the kinetic energy needed for a successful explosion is estimated to be $\sim 10^{51}$ ergs, but the mechanism of how to gain such a kinetic energy is not well understood.

One of the most studied explanations is the absorption of a fraction of the neutrino energy. In this scenario, the shock wave formed at the boundary between the neutron star and collapsing materials is energized by the neutrinos. Blondin et al. (2003) showed that the accretion instability, so-called non-spherically symmetric standing accretion shock instability (SASI; figure 2.3), enhances the efficiency of the neutrino absorption to the level of a successful explosion. The effect also contributes the kick of a neutron star, and may explain the mean pulsar birth velocity ($450 \pm 90\,\mathrm{kms}^{-1}$, Lyne & Lorimer 1994) observed in our galaxy. Burrows et al. (2006, 2007) suggested that the acoustic power, generated in the neutron star by the effect of SASI, eventually drives an explosion. On the other hand, Wheeler et al. (2002) proposed that the amplification of the stellar magnetic field mainly contributes to an explosion rather than the neutrino absorption. They argued that if the massive star is differentially rotating, the magnetic field is compressed around the rotation axis and gives the pressure to the pole directions. It forms the magneto-centrifugal jet,

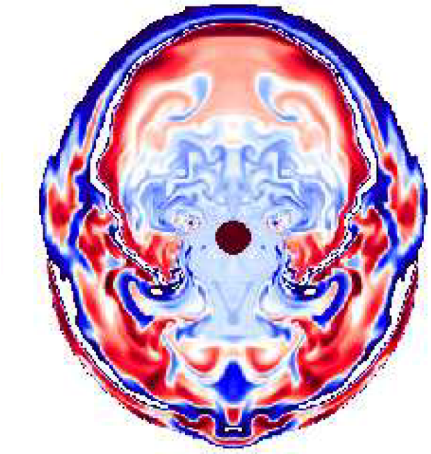

Figure 2.3: Entropy color map (red is higher than the equilibrium value, and blue is lower) on the effect of SASI. The image is taken from figure 6 of Blondin et al. (2003).

which leads to a successful explosion.

We note that all of the explosion mechanisms given above depend on the aspherical effects, and the explosions themselves should also be asymmetric. This must be the answer why none of the one-dimensional core-collapse simulations has been successful so far (e.g., Rampp & Janka 2000; Liebendörfer et al. 2001; Thompson et al. 2003; Sumiyoshi et al. 2005).

2.1.4 Nucleosynthesis

SN explosions eject the material nucleosynthesized in the stellar core into the space. At this moment, the shock wave penetrating the stellar mantle further proceeds the nucleosynthesis. This process is called the explosive nucleosynthesis, and occurs in either core-collapse or Type Ia SNe. In the explosive nucleosynthesis, various heavy elements are synthesized by different burning processes depending on the temperature. The temperature T at a radius r in the SN is roughly evaluated as follows,

$$E \sim \frac{4\pi}{3} r^3 a T^4 \tag{2.2}$$

where E is the explosion energy. Equation 2.2 shows that the produced elements vary depending on the depth where they are located. Although the equation seems slightly too simplified for the core-collapse SNe which need the aspherical effect for explosions, stratified structures expected by the explosive burning are observed in Type Ia SNe (Stehle et al. 2005). The explosive nucleosyntheses are summarized in Table 2.1.

In the explosive nucleosynthesis, a large amount of ^{56}Ni is created. Since ^{56}Ni is an

Table 2.1: Explosive nucleosynthesis.

Burning site	Main products	Temperature [10^9 K]
C/Ne burning	O, Ne, Mg, Si	~ 2.1
O burning	O, Si, S, Ar, Ca	~ 3.3
Incomplete Si burning	Si, S, Ar, Ca, ^{56}Ni, Fe, Mn, Cr	~ 4
Complete Si burning	^{56}Ni, Ti, ^{64}Zn, Co	> 5

unstable nucleus, it is converted to the stable ^{56}Fe by the following nuclear decays

$$^{56}\mathrm{Ni} \xrightarrow[\tau=6.077\mathrm{d}]{} ^{56}\mathrm{Co} \xrightarrow[\tau=77.23\mathrm{d}]{} ^{56}\mathrm{Fe\ (stable)} \tag{2.3}$$

where τ is a half-life of the nuclide.

Figure 2.4 shows the resultant supernova yields for core-collapse and Type Ia. The yields of core-collapse SNe are generally dominated by C, O, Ne, and Mg, which are products of the nucleosynthsis in the stellar evolution. Especially, the amount of O is quite striking, and it increases depending on the progenitor mass. The Fe-group yields of core-collapse SNe, on the other hand, are much less than those of Type Ia. This is because in core-collapse SNe the Fe core falls into a neutron star or a black hole, while the Type Ia progenitor is completely disrupted.

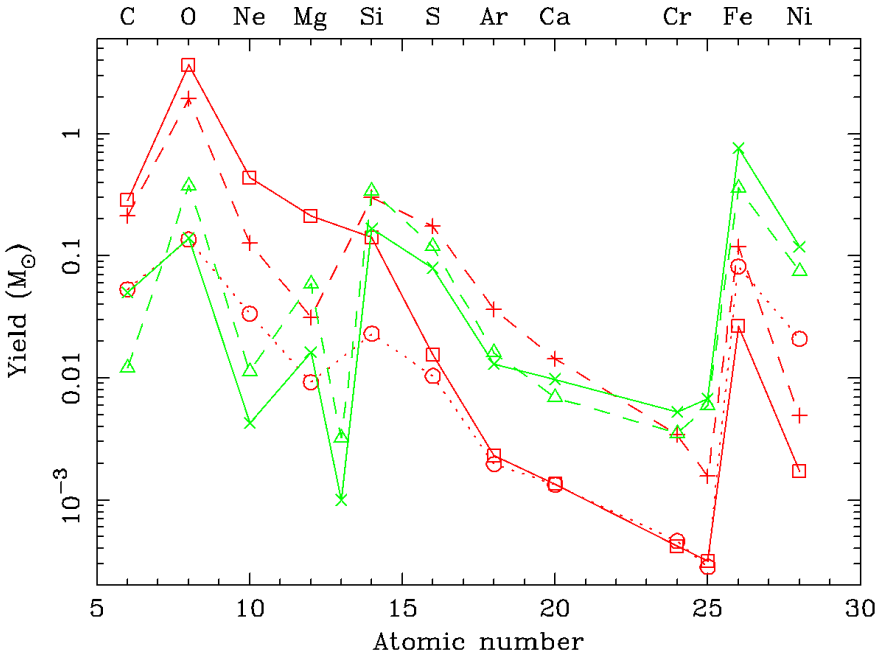

Figure 2.4: Predicted masses of heavy elements nucleosynthesized in SNe. The red lines indicate the yields for core-collapse SNe with different progenitor masses (dotted line: 11 $M_\odot$, dashed line: 20 $M_\odot$, solid line: 30 $M_\odot$) by Woosley & Weaver (1995), whereas the green lines indicate those of Type Ia SNe (solid line: W7, dashed line: CDDT) by Maeda et al. (2010).

2.2 Supernova Remnants

The shocked wave formed by the SNe heats up both the surrounding interstellar medium (ISM) and the ejecta spewed out from the progenitors. The material heated up forms a plasma called supernova remnant (SNR). The SNRs have a variety of morphologies due to the distribution of the ISM and the asymmetry of the explosion. Green (2014) identified and listed 298 SNRs in our galaxy based on the radio observations. About a half of them are observed in X-rays. In this section, we explain the classification, shock heating process, and evolution of SNRs.

2.2.1 Classification

Based on the radio wavelength morphology, SNRs are classified into three types: shell, plerion, and composite type. Green (2014) argued that 68 %, 3 %, and 7 % of the Galactic SNRs were classified as shell type, plerion type, and composite type, respectively. The types of the other Galactic SNRs (22 %) are not well determined. Addition to these categories, Rho & Petre (1998) proposed a new morphological class, called “mixed-

morphology" SNRs. Mixed-morphology type consists of a shell type morphology in radio band, and a center-filled morhology in X-rays.

Shell Type

Shell type has a limb brightened morphology in both radio and X-rays (figure 2.5 (a)). The radio emission is mainly the synchrotron radiation from relativistic electrons accelerated up to the energy of GeV by the blast wave. The X-ray emission is mainly thermal, originates from the hot plasma of the ISM and the ejecta heated by the blast wave and reverse shock, respectively (Chevalier 1982). Cassiopeia A, Tycho's SNR, and Kepler's SNR are classified in this group. Some of shell type SNRs, such as SN1006 and RX J1713.7−3946, also have non-thermal X-rays, which is emitted by electrons accelerated to the energy of TeV.

Plerion Type

Plerion type has center-filled morphology in radio band (figure 2.5 (b)). The name of plerion is derived from the Greek word for "full" (Weiler & Panagia 1978). This type of SNRs is also called Crab-like or filled center SNRs. The origin of the central emission is the pulsar wind nebula powered by a rapidly rotating neutron star (pulsar). The rotating pulsar loses its energy with a rate of $\dot{E} = I\Omega\dot{\Omega} = 4\pi I\dot{P}/P^3$, where Ω, P, and I represent the angular frequency, rotational period, and moment of inertia, respectively. This energy causes the wind of relativistic electrons and positrons, which radiates a synchrotron radiation by interacting with the magnetic field of the pulsar. It is called a pulsar wind nebula. The Crab nebula, CTB87, and 3C58 are classified as the plerion type. Since the plerion type has a neutron star, this type of SNRs should originate from a core-collapse SN.

Composite Type

Composite type has both the central component (plerion) and the shell component (figure 2.5 (c)). The shell component is a thermal origin as those of the shell type SNRs, while the central component is non-thermal origin as those of the plerion type. The core-collapse SNRs with ages less than $\sim 20,000$ yr are expected to have pulsars and pulsar wind nebula in the shell. Examples of composite type SNRs are CTB 109, Vela SNR, and G11.2−0.3.

Mixed-Morphology Type

Mixed-morphology (MM) type is, unlike other categories, classified based on both radio and X-ray morphologies. The radio emission distributes like a shell type, while the X-ray emission mainly comes from the center (figure 2.5 (d)). This type is also called thermal composite type (Shelton et al. 1999). The X-ray emission from the center of these SNRs is not powered by pulsars, but originates from hot plasmas. About 10 % of all the Galactic SNRs, and 25 % of the X-ray detected Galactic SNRs are classified as MM SNRs (Rho & Petre 1998). W44, W28, and 3C 391 belong to this class. Most of the MM SNRs are associated with molecular clouds, and often contain OH (1720 MHz) maser sources (e.g., Yusef-Zadeh et al. 2003). Some MM SNRs exhibit the TeV/GeV gamma-ray emissions, indicating the presence of high energy protons interacting with molecular clouds (e.g., Abdo et al. 2010). These dense and complex environments might affect the evolution of the morphologies; e.g., many small clouds slowly evaporate and emit X-rays after the passage of the blast wave (cloud evaporation scenario; White & Long 1991), or preexisting dense clouds cool the outer shell of the remnants at the not-detectable temperature (thermal conduction scenario; Petruk 2001).

(a) Shell type

(b) Plerion type

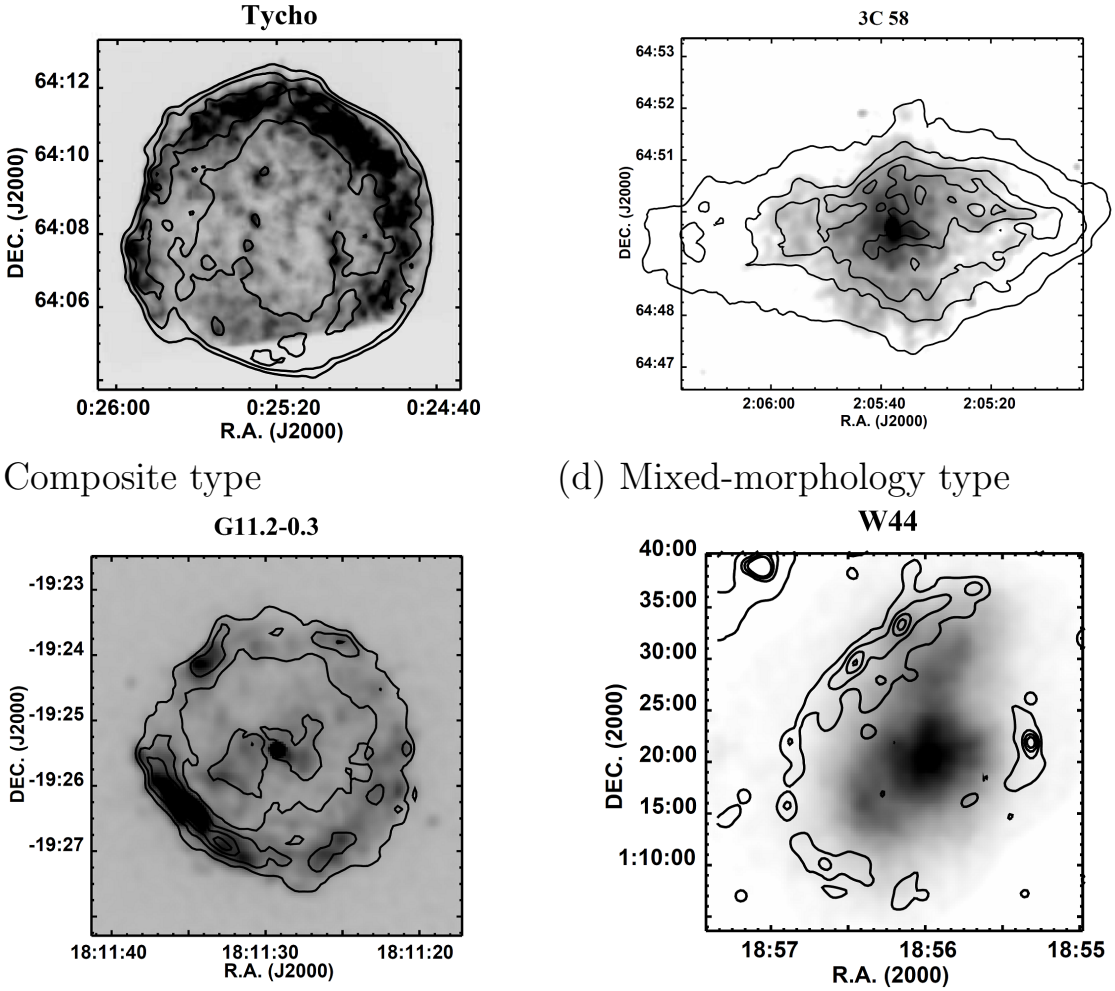

(c) Composite type

(d) Mixed-morphology type

Figure 2.5: *Chandra* X-ray images (0.3–10 keV) of four types of SNRs. Black contours represent the radio images with VLA 1.375 GHz for Tycho's SNR, VLA 21 cm for 3C 58 and G11.2−0.3, and VLA 1.4 GHz for W44, respectively. These images are taken from Kawasaki (2003)

2.2.2 Shock Wave Heating

A shock wave is formed in a supersonically compressive motion. As the shock wave passes, the material is compressed and heated up. The properties of the shock wave are expressed in the following equations,

$$\rho_0 v_0 = \rho_1 v_1 \tag{2.4}$$

$$\rho_0 v_0^2 + p_0 = \rho_1 v_1^2 + p_1^2 \tag{2.5}$$

$$\frac{1}{2}v_0^2 + w_0 = \frac{1}{2}v_1^2 + w_1 \tag{2.6}$$

where ρ, v, p, and w represent the density, velocity, pressure, and enthalpy per mass unit ($w = \gamma p/p(\gamma - 1)$, where γ is a specific-heat ratio). The subscripts of 0 and 1 correspond to the upstream and downstream, respectively. Noth that the velocity is defined at the rest frame of the shock wave. The upstream side corresponds to the outer side of the SNR shell. These equations represent the conservation of mass flux, momentum flux, and energy flux at the shock front. From the fluid equations, we can obtain Rankin & Hugoniot relations as follows,

$$\frac{\rho_0}{\rho_1} = \frac{v_1}{v_0} = \frac{(\gamma+1)p_0 + (\gamma-1)p_1}{(\gamma-1)p_0 + (\gamma+1)p_1} \tag{2.7}$$

$$\frac{T_0}{T_1} = \frac{p_1}{p_0}\frac{(\gamma+1)p_0 + (\gamma-1)p_1}{(\gamma-1)p_0 + (\gamma+1)p_1} \tag{2.8}$$

where T represents the temperature.

We can rewrite the equations (2.7) and (2.8) by using the Mach number, $M_0 = v_0/C_0$, where $C = \gamma p/\rho$ is the sound velocity,

$$\frac{\rho_1}{\rho_0} = \frac{(\gamma+1)M_0^2}{(\gamma-1)M_0^2 + 2} \tag{2.9}$$

$$\frac{T_0}{T_1} = \frac{(2\gamma M_1^2 - (\gamma-1))((\gamma-1)M_1^2 + 2)}{(\gamma+1)^2 M_1^2} \tag{2.10}$$

In the case of mono-atomic gas ($\gamma = 5/3$), these equations give $\rho_1/\rho_0 \simeq 4$ and $T_0/T_1 \simeq 5/16M_0^2$.

The velocities are written by,

$$v_0^2 = \frac{1}{2}(\gamma+1)\frac{p_1}{\rho_0} \tag{2.11}$$

$$v_1^2 = \frac{1}{2}\frac{(\gamma-1)^2 p_1}{(\gamma+1)\rho_0} \tag{2.12}$$

Using the equation of state, the post-shock temperature T_s is expressed by the following equation,

$$kT_s = \frac{3}{16}\mu m_{\rm H} v_s^2 \tag{2.13}$$

where k, μ, and $m_{\rm H}$ represent the Boltzman constant, the mean atomic mass, and the mass of a hydrogen atom, respectively. In the case of a full ionized solar-metallicity plasma ($n_{\rm He} = 0.1 n_{\rm H}$; e.g., citealtAnders1989a), μ is 0.61.

2.2.3 Evolution

The evolution of SNRs is classified into four phases: free expansion phase, adiabatic phase, radiative cooling phase and disappearance phase.

Free Expansion Phase

A shock wave (also called forward shock) is instantaneously formed by the expanding ejecta. The mass of the ejecta is much larger than that of the swept-up ISM in the initial phase of of the evolution. Therefore, the forward shock propagates with constant momentum (free expansion). The forward shock heats up the surrounding ISM. At this phase, the shock radius R_0 and the shock velocity v_s give the following equations,

$$R_s = v_s t \tag{2.14}$$

$$E_0 = \frac{1}{2} M_0 v_s^2 \tag{2.15}$$

where E_0 and M_0 represent the initial kinematic energy of the SN explosion and the total mass of the ejecta. Assuming $E_0 \simeq 10^{51}\,{\rm erg}$ and $M_0 \simeq 10\,M_\odot$, the above equations bring about $v_s \sim 10^8\,{\rm cm\ s^{-1}}$. The free expansion lasts until the mass of the swept up ISM ($M = 4/3\pi R_s^3 n_0$) becomes comparable to the ejecta mass. Therefore, in a typical ISM density of $n_0 \simeq 1\,{\rm cm^{-3}}$, the duration is estimated to be $t \simeq 1,000\,{\rm yr}$.

As the mass of the swept up ISM becomes large, the forward shock is gradually decelerated. The decelerated forward shock evoke another shock (also called reverse shock) that propagates toward the center of the SNR in the rest frame of the forward shock. The reverse shock heats up the ejecta inside the shell (McKee 1974). The boundary between the ISM and the ejecta is called a contact discontinuity. The theoretical growths of the forward shock, reverse shock, and contact discontinuity are shown in figure 2.6. The growth curves are based on the one-dimensional hydrodynamic simulation by Wang & Chevalier (2002). In the plot, the radius and the time are normalized by the following parameters:

$$t' = \left(\frac{t}{1271\,{\rm yr}}\right)\left(\frac{M_0}{10\,M_\odot}\right)^{-5/6}\left(\frac{E_0}{10^{51}\,{\rm erg}}\right)^{1/2}\left(\frac{n_0}{1\,{\rm cm^{-3}}}\right)^{1/3} \tag{2.16}$$

$$r' = \left(\frac{r}{4.1\,{\rm pc}}\right)\left(\frac{M_0}{10\,M_\odot}\right)^{-1/3}\left(\frac{n_0}{1\,{\rm cm^{-3}}}\right)^{1/3} \tag{2.17}$$

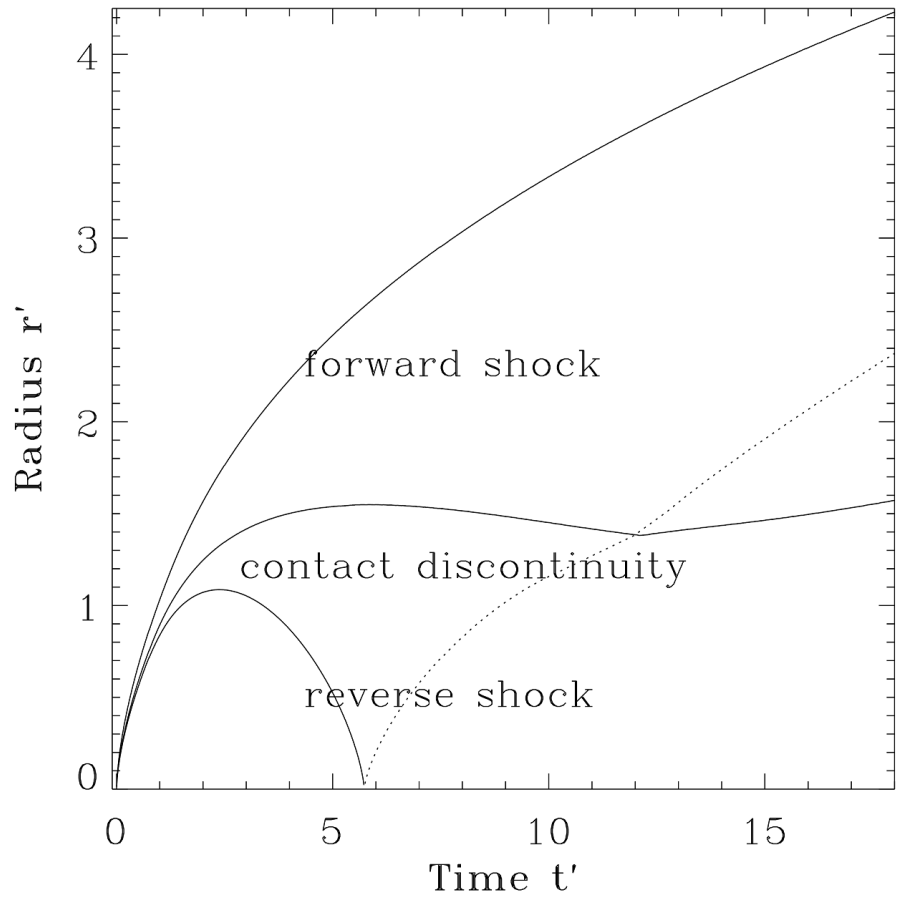

Figure 2.6: Evolution of the forward shock, the contact discontinuity, and the reverse shock radius. The dashed line represents the outgoing weak shock wave caused by the reflection of the reverse shock at the center. The units are normalized by the equation of 2.16 and 2.17 (figure 1 of Wang & Chevalier 2002).

Adiabatic Phase

When the mass of the swept up ISM becomes larger than that of the ejecta, the evolution shifts to the next stage that is called the adiabatic phase (or Sedov phase). Since the time scale of the cooling of the heated gas is much larger than that of the expansion, the blast wave expands adiabatically in this phase. The gas flow is characterized by the two parameters of E_0 and n_0. The radius R_s and the velocity v_s of the blast wave, and mean temperature just behind the shock front T_s are given as

$$R_s = 13 \left(\frac{E_0}{10^{51}\,\mathrm{erg}} \right)^{1/5} \left(\frac{n_0}{1\,\mathrm{cm}^{-3}} \right)^{-1/5} \left(\frac{t}{10000\,\mathrm{yr}} \right)^{2/5} \mathrm{pc} \tag{2.18}$$

$$T_s = 0.28 \left(\frac{E_0}{10^{51}\,\mathrm{erg}} \right)^{2/5} \left(\frac{n_0}{1\,\mathrm{cm}^{-3}} \right)^{-2/5} \left(\frac{t}{10000\,\mathrm{yr}} \right)^{-6/5} \mathrm{keV} \tag{2.19}$$

$$v_s = 490 \left(\frac{E_0}{10^{51}\,\mathrm{erg}}\right)^{1/5} \left(\frac{n_0}{1\,\mathrm{cm}^{-3}}\right)^{-1/5} \left(\frac{t}{10000\,\mathrm{yr}}\right)^{-3/5} \mathrm{km\ s}^{-1} \tag{2.20}$$

In this phase, the density of the swept up ISM is much higher than that of the ejecta. The Sedov phase lasts 10,000–20,000 yr, and $\sim 70\,\%$ of the initial kinematic energy of the explosion is transformed into the thermal energy of the swept up ISM (Chevalier 1974).

Radiative Cooling Phase

When the shell of the SNR cools down to $\sim 10^6$ K, the cooling rate increases by enhanced emissivities of line emissions from heavy elements. In this stage, the radiative cooling is not negligible, and the expansion is no longer adiabatic (radiative cooling phase). The material behind the blast wave, where the density is high compared to that of the inner region, cools more efficiently than those at inner regions. However, the pressure equilibrium is kept inner the shell, and the shell expands by the internal gas pressure. This stage is called pressure-driven snowplow (PDS) phase. The time dependencies of the radius and the velocity of the blast wave are describes as follows (McKee & Ostriker 1977):

$$R_s \propto t^{2/7} \tag{2.21}$$

$$v_s \propto t^{-5/7} \tag{2.22}$$

If the pressure of the internal material becomes comparable to that of the surrounding ISM, the shell expansion is driven only by the remaining momentum. At this so-called momentum-conserving snowplow (MCS) stage (Cioffi et al. 1988), the relations between the radius, temperature, and time are expressed as follows:

$$R_s \propto t^{1/4} \tag{2.23}$$

$$v_s \propto t^{-3/4} \tag{2.24}$$

The radiative cooling phase lasts a few thousand years.

Disappearance Phase

About millions years after the SN explosion, the expansion speed drops to the sound speed in the ISM, and the shock wave no longer lasts. Due to the random motion of the ISM (10–20 kms^{-1}), the material in the shell is merged into the ISM, and the remnant becomes indistinguishable.

2.3 Thermal X-rays from Supernova Remnants

The shock wave heating forms an optically thin hot plasma, which consists of the ejecta and the swept up ISM. In this section, we describe the thermal X-ray emissions from the SNR plasma.

2.3.1 Continuum Emission

The continuum emission from the SNR plasma consists of 3 components: bremsstrahlung, radiative recombination continuum (RRC), and 2-photon decay. These are also categorized by the transitions of electrons as follows: free-free (bremsstrahlung), free-bound (RRC), bound-bound (2-photon decay and fluorescent lines) emission.

Free-Free Emission: Bremsstrahlung

Free electrons in the plasma emit photons by the Coulomb interaction with ions. The emission is called bremsstrahlung. The emissivity of the bremsstrahlung for electrons with a Maxwellian energy distribution is given by

$$\varepsilon_{ff} = \frac{2^5\pi e^6}{3m_{\rm e}c^3}\left(\frac{2\pi}{3km_{\rm e}}\right)^{1/2} g_{ff}(T_{\rm e})T_{\rm e}^{-1/2}\exp\left(-\frac{h\nu}{kT_{\rm e}}\right) n_{\rm e}n_i Z_i^2 \ {\rm ergs}^{-1}{\rm cm}^{-3}{\rm Hz}^{-1} \qquad (2.25)$$

where e, c, Z, $n_{\rm e}$, n_i, and g_{ff} are the electron charge, light speed, ion charge, electron and ion densities, and gaunt factor (e.g., Rybicki & Lightman 1979). Since the spectral shape of the bremsstrahlung (see figure 2.7) only depends on $T_{\rm e}$, we can estimate the electron temperature from this component.

In the case of the solar metallicity plasma, since the bremsstrahlung from hydrogen and the helium ions is dominant, the spectral fitting codes usually treat the normalization with $\int n_{\rm e}n_{\rm H}dV$. It is called the emission measure (EM). The spectral fitting code XSPEC, which we use in this thesis, uses the normalization factor called the volume emission measure, $\int n_{\rm e}n_{\rm H}dV/(4\pi d^2)$, where d is the distance to the source.

Free-Bound Emission: Radiative Recombination Continuum

When a free electron is captured by one of the atomic shells, RRC emission arises. The energy of emitted photons is described as $h\nu_n = E_{\rm e} + \chi_n$, where $E_{\rm e}$ and χ_n are the energy of the free electron and the binding energy for an electron in level n. Since the electron energy is not uniquely determined in the thermal plasma, the spectral shape of the RRC becomes a continuum, but with a sharp edge at the binding energy of the levels (see figure

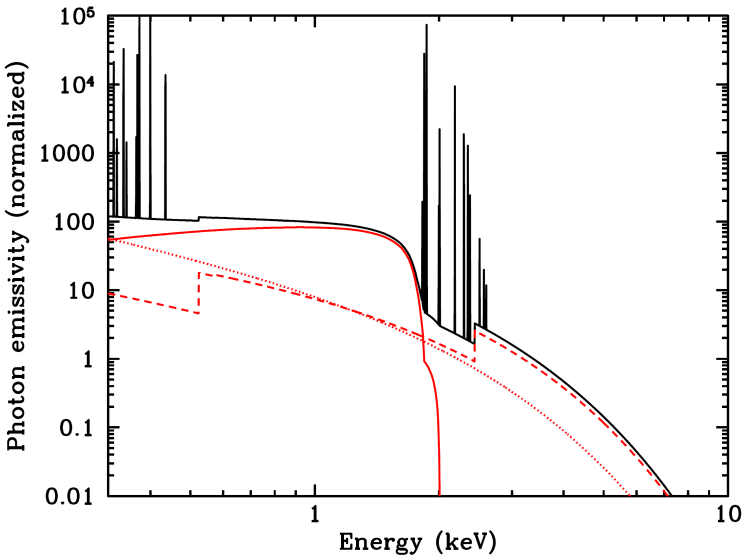

Figure 2.7: Thermal emissions from a pure silicon plasma ($kT_\mathrm{e} = 1\,\mathrm{keV}$, $n_\mathrm{e}t = 5 \times 10^{10}\mathrm{cm}^{-3}\mathrm{s}$). The red solid, dashed, and dotted lines represent the emissivities of the bremsstrahlung, radiative recombination continuum, and 2-photon emission. In the total emissivity (black), the line emissions from ions of silicon are also included (figure 10 of Vink 2012).

2.7). The emissivity of the RRC is given by

$$\varepsilon_{bf} = 4 n_\mathrm{e} n_{i+1} h\nu \left(\frac{h\nu - \chi_n}{kT_\mathrm{e}}\right) \left(\frac{1}{2\pi m_\mathrm{e} kT_\mathrm{e}}\right)^{1/2} \sigma_n^\mathrm{rec}(h\nu - \chi_n) \exp\left(-\frac{h\nu - \chi_n}{kT_\mathrm{e}}\right) \tag{2.26}$$

where n_{i+1} and σ_n^rec are the density of a ion with charge $i+1$ and the recombination cross section to the level n at the given electron energy, respectively.

In the case of a solar metallicity plasma, the RRC emission does not stand out, since the bremsstrahlung from light elements (such as H and He) is usually dominant. However, if the plasma is overionized (details are given in section 2.3.3), the edge structure of the RRC can be identified.

Bound-Bound Emission: 2-Photon Emission

When the direct transition between two bound states is forbidden by a selection rule, 2-photon process occurs. In such a case, although the sum of the energy of emitted 2 photons is conserved, the energy of the each photon is not uniquely determined. Therefore, the 2-photon processes form a continuous spectrum (see figure 2.7).

2.3.2 Line Emission

The bound-bound transition between two quantum levels emits line emissions. A H-like ion, which contain only one electron per ion, radiates the line emission with the energy of

$$E \sim A^2 R_y \left(\frac{1}{n^2} - \frac{1}{n'^2} \right) \tag{2.27}$$

where A, R_y, n, and n' are the atomic number, the Rydberg constant (13.6 eV), and the principal quantum number of before and after transition, respectively. The emission lines are called Lyα (H-like Kα; $2p \rightarrow 1s$), Lyβ (H-like Kβ; $3p \rightarrow 1s$), Lyγ (H-like Kγ; $4p \rightarrow 1s$), and so on. In the case of He-like ion, which contain only two electron per ion, we also call Heα (He-like Kα; $2 \rightarrow 1$), Heβ (He-like Kβ; $3 \rightarrow 1$), Heγ (He-like Kγ; $4 \rightarrow 1$). The line energies of the major elements in SNRs are summarized in table 2.2.

Table 2.2: Energies (eV) of K-shell transition lines from H-like and He-like ions.

	Lyα	Lyβ	Lyγ		Heα		Heβ	Heγ
				res.*	forb.*	int.*		
O	654	775	817	574	561	569	665	698
Ne	1022	1211	1277	922	905	915	1072	1127
Mg	1472	1745	1840	1352	1330	1343	1579	1660
Si	2006	2377	2506	1865	1840	1854	2183	2294
S	2623	3107	3277	2461	2431	2447	2884	3033
Ar	3323	3936	4151	3140	3104	3124	3685	3875
Ca	4106	4864	5130	3908	3845	3892	4582	4819
Fe	6966	8266	8732	6702	6641	6670	7798	8217
Ni	8077	9590	10107	7806	7744	7766	9190	9680

* res., forb., and int. indicate resonance, forbidden, and inter-combination lines, respectively.

The Heα line consists of three fine structures: resonance ($1s2p\ ^1\mathrm{P}_1 \rightarrow 1s^2\ ^1\mathrm{S}_0$), forbidden ($1s2s\ ^3\mathrm{S}_1 \rightarrow 1s^2\ ^1\mathrm{S}_0$), and inter-combination ($1s2p\ ^3\mathrm{P}_{2,1} \rightarrow 1s^2\ ^1\mathrm{S}_0$). The detail of emission mechanisms are given in Porquet et al. (2001).

The ionization states of ions vary depending on the plasma conditions. The ionization states are parametrized as a function of the ionization temperature as shown in figure 2.8. The ionization temperature (kT_z) is equal to the electron temperature (kT_e) in the collisional ionization equilibrium (CIE) plasma, in which the ionization rate is equivalent to the recombining rate, although it is not a usual case in the SNR (see section 2.3.3).

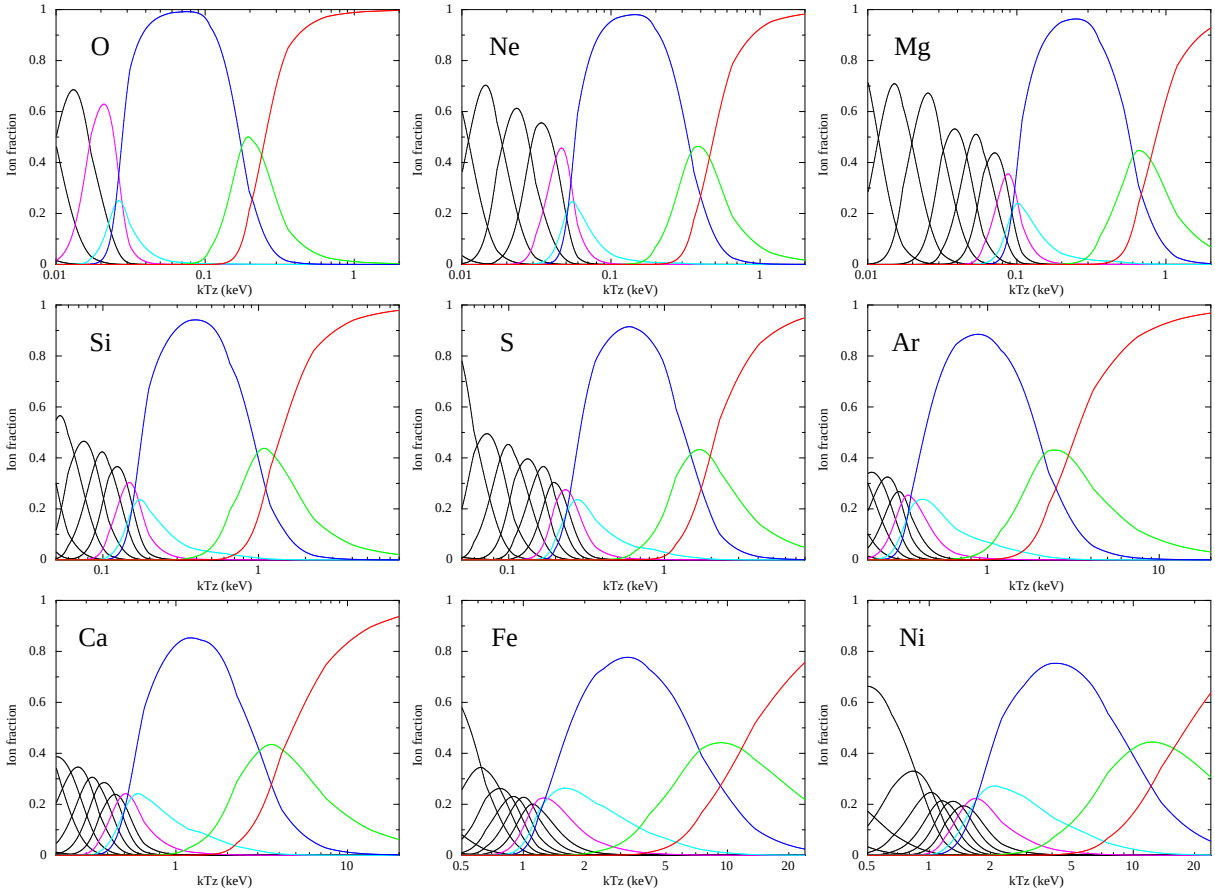

Figure 2.8: Ion fraction of heavy elements as a function of ionization temperature. Red, green, blue, light blue, magenta, and black lines corresponds to fully-ionized, H-, He-, Li-, Be-like, and lower ionized ions, respectively. The data are extracted from the plasma code (APEC) in XSPEC.

The weighted center energy of line emissions from each element increases depending on the ionization degree. It is a useful tool to estimate the ionization state directly. Figure 2.9 shows the line center energies of Fe K-shell lines as a function of the ion charge. The line center energy varies from 6.4 keV (Fe I) to 6.7 keV (Fe XXVIII), and can be discriminated with the energy resolution ($\sim$ 200 eV) of recent X-ray CCD detectors.

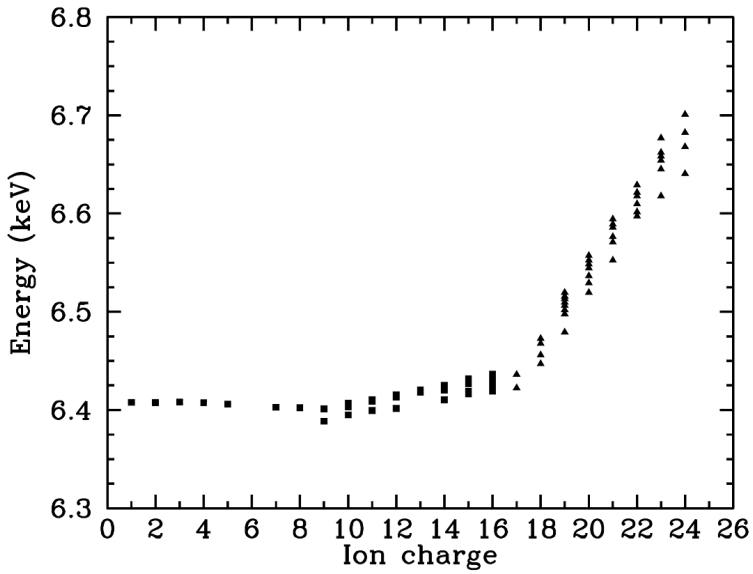

Figure 2.9: The line energies of Fe K-shell transitions determined theoretically (squares, Fe II–Fe XVII, Palmeri et al. 2003, Mendoza et al. 2004) and observationally (triangles, Fe XVIII–Fe XXV, Beiersdorfer et al. 1993). This figure is taken from Vink (2012).

2.3.3 Non-Equilibrium Ionization

The shock heating process of SNRs converts the translational motion of the swept up material into the random thermal motion. Therefore, the particles behind the shock wave obtain the temperature of $T_{\rm i} \propto m_{\rm i} V_s^2$. Because of the mass of the particles, the temperature non-quilibrium between electrons and protons arises ($T_{\rm i} \simeq 2000 T_{\rm e}$), and then becomes moderate by the particle interaction. The equilibration timescales of electron-proton and electron-electron interactions are described as follows (Zeldovich & Raizer 1966),

$$\tau_{\rm ep} \simeq 3.1 \times 10^{11} n_{\rm p}^{-1} \left(\frac{kT}{1\,{\rm keV}} \right)^{3/2} \left(\frac{\ln\Lambda}{30.9} \right) \ {\rm s} \tag{2.28}$$

$$\tau_{\rm ee} \simeq 4.9 \times 10^{8} n_{\rm e}^{-1} \left(\frac{kT}{1\,{\rm keV}} \right)^{3/2} \left(\frac{\ln\Lambda}{30.9} \right) \ {\rm s} \tag{2.29}$$

where $\ln\Lambda$ is the Coulomb logarithm ($\simeq 30.9$ in X-ray emitting plasma of $n_{\rm e} \simeq 1$). On the other hand, the timescale required to reach an ionization equilibrium is estimated as (Masai 1984),

$$\tau_{\rm ion} = \sum_{j=1}^{Z} (n_{\rm e} S_j)^{-1} = n_{\rm e}^{-1} [\min(S_i)]^{-1} \simeq 10^{12} n_{\rm e}^{-1} \ {\rm s} \tag{2.30}$$

where S_j is the ionization rate coefficient from the jth ion. Therefore, these three timescales are compared as

$$\tau_{\rm ee} \ll \tau_{\rm ep} < \tau_{\rm ion} \tag{2.31}$$

This relation is interpreted that the electrons heated by protons ionize ions. Since the ionization timescale is comparable to the SNR ages, the plasmas in most young SNRs are in the non-equilibrium ionization state (NEI). In the NEI plasma, the ionization temperature lower than the electron temperature is observed ($kT_{\rm e} > kT_{\rm z}$). We call this plasma the ionizing plasma (IP) in the sense that the ionizing process is more predominant than the recombining process. These plasmas approach to the collisional ionization equilibrium (CIE; $kT_{\rm e} = kT_{\rm z}$) in the last stage of the SNR evolutions.

However, the recombining plasmas (RPs) are recently discovered in some of MM SNRs (e.g., Ozawa et al. 2009; Yamaguchi et al. 2009). In these plasmas, the ionization temperatures are higher than the electron temperatures ($kT_{\rm e} < kT_{\rm z}$), so that the recombining process is predominant. These ionization states conflict with those expected in the standard SNR evolution ($kT_{\rm e} > kT_{\rm z}$). There are two major scenarios for the formation of RPs. One is the selective ionization, in which the ionization is advanced independently by such as a photo ionization with strong X-ray sources (Nakashima et al. 2013) or a collisional ionization with high energy cosmic-rays (Tanaka 1986). The other is the electron cooling, in which only the electron temperature is dropped down by such as a thermal conduction cooling with molecular clouds (Kawasaki et al. 2002) or an adiabatic rarefaction (Itoh & Masai 1989; Yamaguchi et al. 2009). It is still unclear which formation process is true. We note that since RPs are often found in MM SNRs, the characteristic environment of these SNRs would play the key role for the formation of the RP.

2.4 Progenitor Studies on Supernova Remnants

Several previous studies have proposed the discriminating method of progenitor types of SNRs. In this section, we review main results of these studies.

2.4.1 Morphological Analysis

The morphologies of SNRs are dependent on both of the SN explosions and the circumstellar environments. If the ejecta or ISM distributes non-uniformly, the SNR morphology is distorted. It is generally expected that core-collapse SNRs have more distorted morphologies than Type Ia SNRs. One of the reason is that asymmetric explosions are expected in core-collapse SNRs by the SN simulations as explained in section 2.1.3. The core-collapse ejecta are also expected to be well mixed due to the hydrodynamical instability. Another reason is that core-collapse SNe occur in dense and complex region where massive stars born.

Lopez et al. (2009, 2011) proposed the discriminating method of progenitor types, focusing on these facts. Left panel of figure 2.10 shows the *Chandra*/ACIS images of several extended SNRs. They analyzed these images with a multipole expansion method and wavelet-transform method, and then they obtained the mirror symmetry P_2/P_0 and circular symmetry P_3/P_0 as shown in right panel of figure 2.10. Consistent with the above expectation, the SNRs that are likely Type Ia origin have more symmetric morphologies than core-collapse, which is consistent with the above expectations. However, we note that since Type Ia SNe can also take place in dense and complex regions, typing with this morphological method is not sure.

2.4.2 Overall Spectral Features

Nucleosynthesis yields are different between core-collapse and Type Ia SNe. Core-collapse SNe produce large amount of light elements, such as O, Ne, and Mg, whereas main products of Type Ia are intermediate mass and Fe-group elements.

Figure 2.11 shows the examples of X-ray spectra for core-collapse (Cas A) and Type Ia (Kepler) SNRs obtained with *Suzaku*. These X-ray spectra contain strong K-shell emissions from the alpha elements (O, Ne, Mg, Si, S, Ar, Ca) and Fe-group elements, main products of SNe. The depression in the soft energy bands are due to the interstellar absorption along the direction to the sources. We see a distinct bump around 1 keV only in the Type Ia spectrum. This feature is the L-shell emission of the Fe-group elements that cannot be resolved by the current X-ray CCDs. The strong Fe-L emission is characteristic

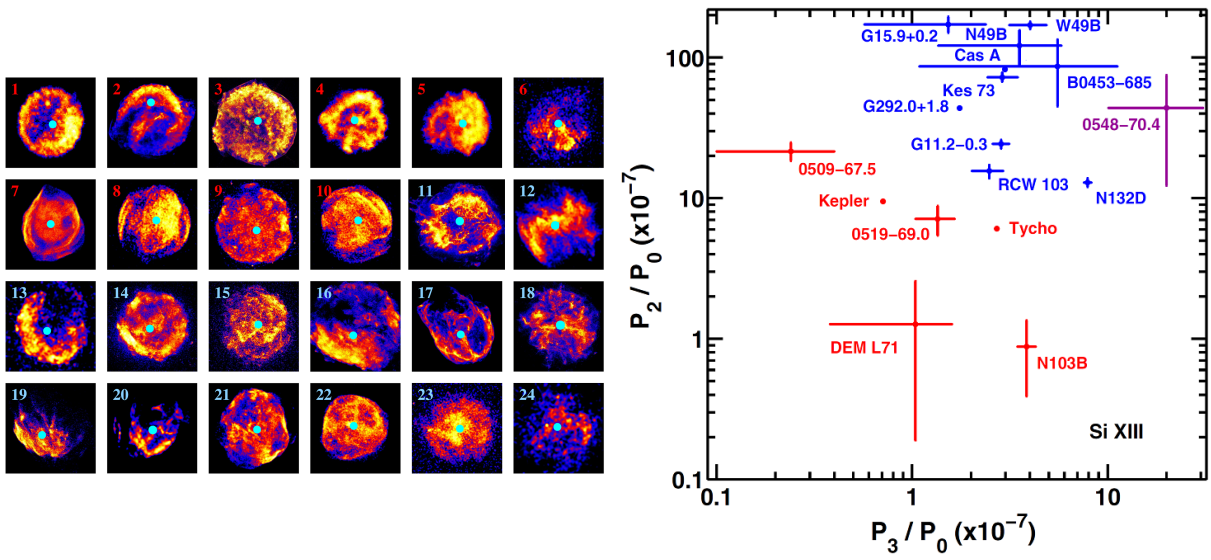

Figure 2.10: Morphological symmetry of core-collapse (red) and Type Ia SNRs. Left: *Chandra* soft-band (0.5–2.1 keV) images of 24 SNRs. Right: mirror symmetry P_2/P_0 vs. the circular symmetry P_3/P_0 of the Si K-shell emission images for SNRs listed in the left panel. These images are taken from Lopez et al. (2011).

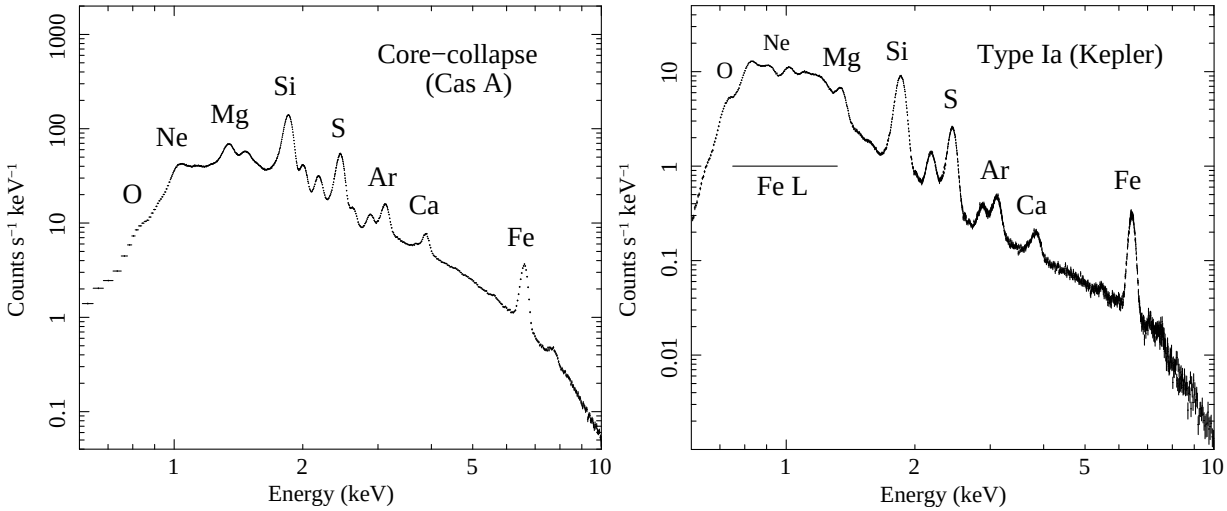

Figure 2.11: *Suzaku* spectra of core-collapse (Cas A) and Type Ia (Kepler) SNRs.

for the Type Ia SNRs (Hughes et al. 1995). Although Hughes et al. (1995) also argued that core-collapse SNRs have strong K-shell lines of light elements (O, Ne, Mg), it is not always the case as seen in figure 2.11. It is because the line emissivities largely depend on the electron temperatures and ionization states. Since the SNR spectra also consist both of the ejecta and ISM, in order to determine the progenitor types, we need to analyze the spectra with a plasma model such as NEI in XSPEC.

2.4.3 Ionization States of Fe K-shell Emission

Yamaguchi et al. (2014), on the other hand, proposed a new typing method using the center energy of Fe K-shell emission line. As mentioned in section 2.3.2, the center energies of Fe K-shell emission line largely vary depending on their ionization states. Since the variation width (6.4–6.7 keV) is enough larger than the energy resolution (typically ~ 200 eV) of the X-ray CCDs, we can accurately derive the ionization states. Yamaguchi et al. (2014) found the empirical laws that the Fe K emissions of Type Ia SNRs have lower center energies ($\sim$ 6.4 keV) than those of core-collapse SNRs ($\sim$ 6.6 keV). Since their samples of core-collapse and Type Ia SNRs have similar ages and radii, they considered that the difference of the center energies was due to significantly higher ambient medium densities in the core-collapse SNRs, which cause the early arrival time of the reverse shocks to inner Fe-rich regions. The idea is consistent with the expectations that the progenitors of core-collapse SNRs exist in dense star forming regions, although those of Type Ia SNRs can be in similar environments.

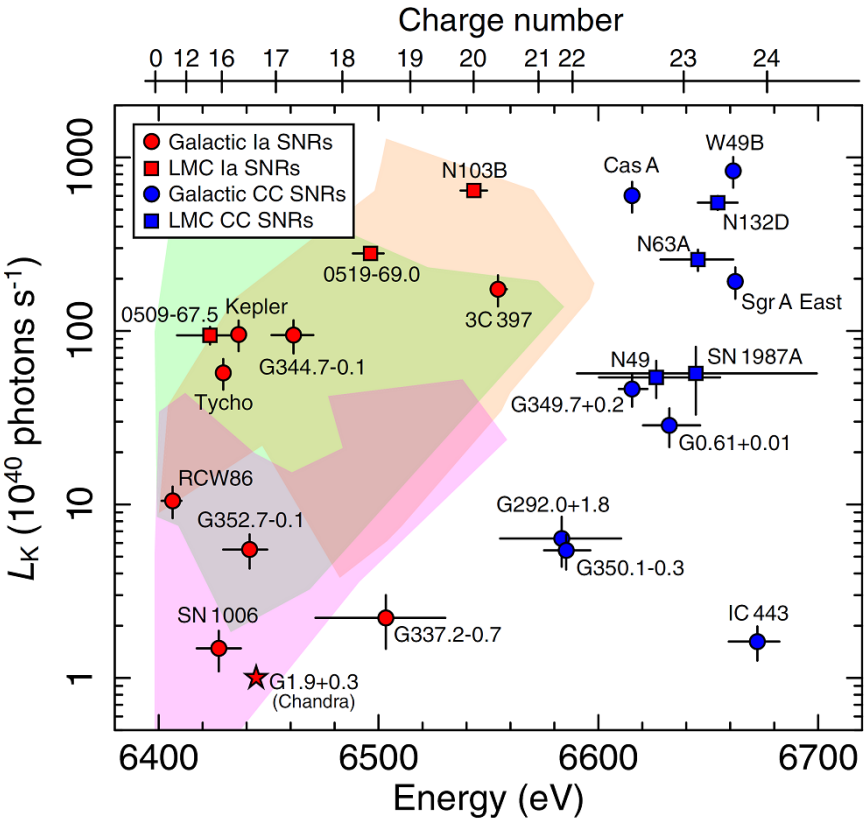

Figure 2.12: Center energies and line luminosities of Fe K-shell emission. This figure is taken from Yamaguchi et al. (2014).

Chapter 3

Suzaku

Suzaku is the Japan's fifth X-ray observatory. The X-ray sensitive silicon CCD camera (XIS) onboard *Suzaku* has good energy resolution, high efficiency, and low and stable background, which are essential for the accurate observations of SNRs. We then mainly use the data obtained with the *Suzaku* XIS throughout this thesis. In this chapter, we gives the overviews of the *Suzaku* satellite and onboard instruments.

3.1 Overview

Suzaku (Mitsuda et al. 2007) was developed by the Institute of Space and Astronautical Science (ISAS) of Japan Aerospace Exploration Agency (JAXA) in collaboration with the National Aeronautics and Space Administration's Goddard Space Flight Center (NASA/GSFC) and many other institutions. It was launched with the M-V launch vehicle from the Uchinoura Space Center (USC) on 2005 July 10, and has observed X-ray celestial sources until 2015 May 30. It was put into the orbit at a 570 km altitude with an inclination angle of 31°, and the orbital period is about 96 minutes. Figure 3.1 shows the schematic view of *Suzaku*.

Suzaku carries three scientific instruments: the X-ray Imaging Spectrometer (XIS; Koyama et al. 2007), the Hard X-ray Detector (HXD; Takahashi et al. 2007), and the X-ray Spectrometer (XRS; Kelley et al. 2007). The XIS and XRS are soft X-ray imaging detectors (< 12 keV) located at the focal plane of the corresponding X-ray Telescope modules (XRT; Serlemitsos et al. 2007), whereas the HXD is a non-imaging, collimated detector, which covers the higher energy band (10–600 keV). Although the XRS has a superior energy resolution (7 eV), the system became inoperable due to a thermal short between the helium and neon tanks, which resulted in the evaporation of the liquid helium. The capabilities of the active instruments are summarized in table 3.1.

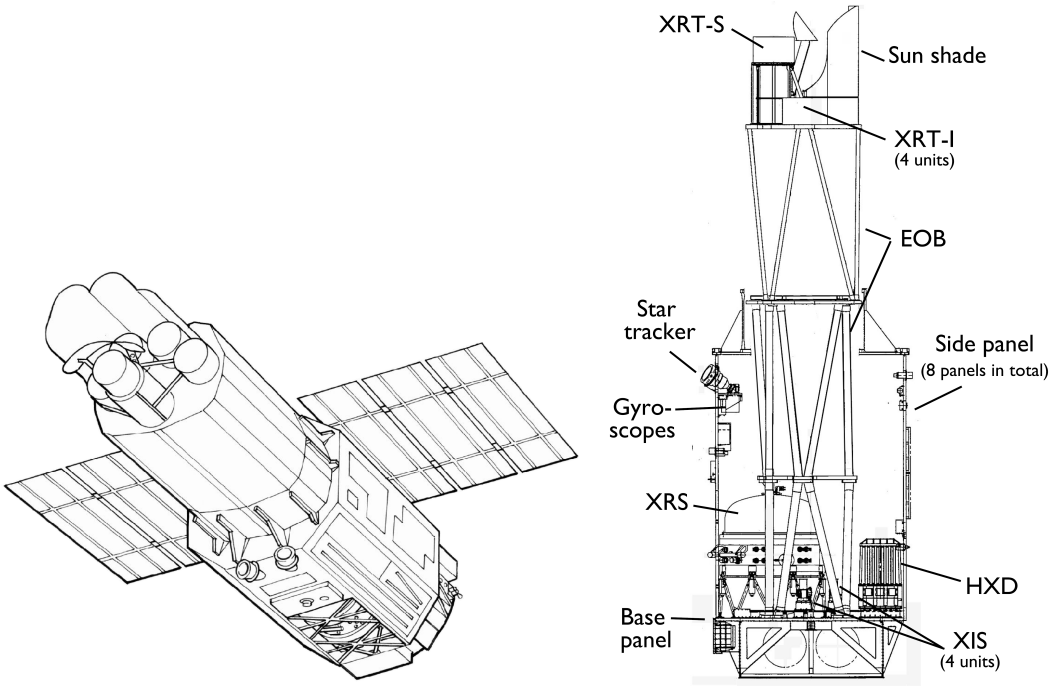

Figure 3.1: Schematic views of *Suzaku* (figure 1 and 2 of Mitsuda et al. 2007).

Table 3.1: Overview of *Suzaku* capabilities (Mitsuda et al. 2007).

XRT	Focal length	4.75 m
	Field of view	$17'$ at 1.5 keV / $13'$ at 8 keV
	Effective area	440 cm^2 at 1.5 keV / 250 cm^2 at 8 keV
	Angular resolution	$2'$ (Half power diameter)
XIS	Field of view	$17'.8 \times 17'.8$
	Energy range	0.2–12 keV
	Pixel grid / size	1024×1024 / 24 μm × 24 μm
	Energy resolution	$\sim$ 130 eV at 6 keV (FWHM)
	Effective area	330 cm^2 (FI), 370 cm^2 (BI) at 1.5 keV
	(including XRT)	160 cm^2 (FI), 110 cm^2 (BI) at 8 keV
HXD	Field of view	$34' \times 34'$ ($\lesssim$ 100 keV) and $4.^\circ5 \times 4.^\circ5$ ($\gtrsim$ 100 keV)
	Energy range	$10 - 600$ keV

3.2 Onboard Instruments

3.2.1 X-ray Telescope

Suzaku has five XRT modules (figure 3.2); one (XRT-S) is equipped for the XRS, and the others (XRT-I) are for the XIS. All five XRTs are co-aligned to image the same region of the sky. This telescope is configured to form a Wolter-I grazing-incidence reflective optics (Wolter 1952). Incident X-rays are reflected twice by the parabolic and the hyperbolic mirrors, and are condensed to the focal plane, when their incident angle is less than $\sim 1^\circ$. In order to increase the effective area, each XRT module has 175 nested foil layers. Because it is difficult to construct a precise Wolter geometry with the foils, both the primary and secondary reflectors are approximated by simple cones.

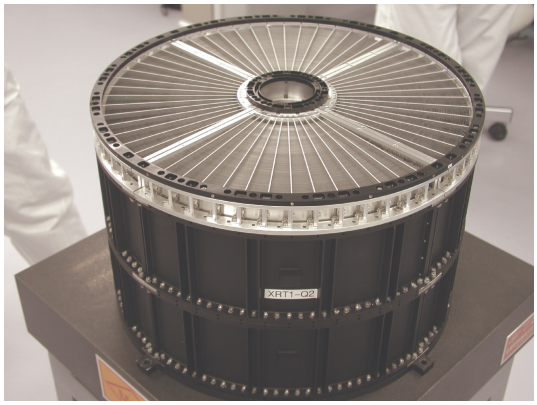

Figure 3.2: Picture of the XRT (figure 2 of Serlemitsos et al. 2007).

Figure 3.3 shows the energy dependence of the total on-axis effective are of the four XRTs, including the detector efficiency. It is compared with those of other X-ray missions. The XRT provides a large efficiency in the energy range of 0.2–12 keV. The effective area of the four XRT modules is larger than *Chandra* in most energy band, and comparable to *XMM-Newton* above ~ 5 keV. As shown in figure 3.3, the effective area is a function of the off-axis angle. This effect is called "vignetting". The point spread function (PSF) of the XRT is $\sim 2'$ in a half power diameter (HPD). The PSF is larger than those of *Chandra* ($\sim 0.5''$; Weisskopf et al. 2002) and *XMM-Newton* ($\sim 10''$; Aschenbach 2002).

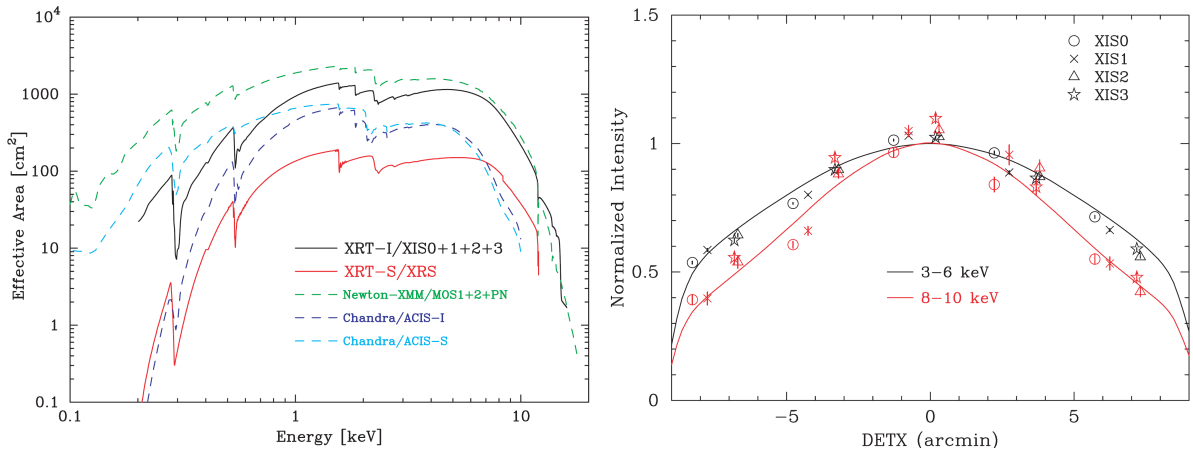

Figure 3.3: Effective area of the XRT. Left: the total effective area of the XRT (combined with XRT). Those of other X-ray satellites (*XMM-Newton* and *Chandra*) are also shown. Right: Off-axis angle dependence of the effective are normalized at the on-axis. Data points are the Crab nebula data, and solid lines are the simulated model (figure 3 and 11 of Serlemitsos et al. 2007).

3.2.2 X-ray Imaging Spectrometer

The XIS was developed through the collaboration among the Center for Space Research at Massachusetts Institute of Technology (MIT), ISAS/JAXA, Osaka University, Kyoto University, Rikkyo University, Kogauin University, and Ehime University. It consists of four sensors (XIS 0, 1, 2 and 3), and each sensor has a sensitive silicon charge-coupled device (CCD), which is operated in a photon counting mode, similar to that used in the *ASCA* SIS (Burke et al. 1993), *Chandra* ACIS (Weisskopf et al. 2002), and *XMM-Newton* EPIC (Lumb et al. 2000).

The schematic views of the XIS are shown in figure 3.4. Each CCD camera has a single chip with an array of 1024×1024 pixels, and covers an $17'.8 \times 17'.8$ region of the sky combined with the XRT. One pixel is 24 μm square, then the size of the CCD is 25 mm×25 mm. Three sensors (XIS 0, 2, and 3) employ front-illuminated (FI) CCDs, and the other (XIS 1) has a back-illuminated (BI) CCD. Figure 3.5 shows the quantum efficiency and effective area of the XIS. Since the depletion layer of the BI CCD ($\sim 42\mu$m) is thinner than that of the FI CCD ($\sim 65\mu$m), the quantum efficiency at high energy of the BI is lower than FI.

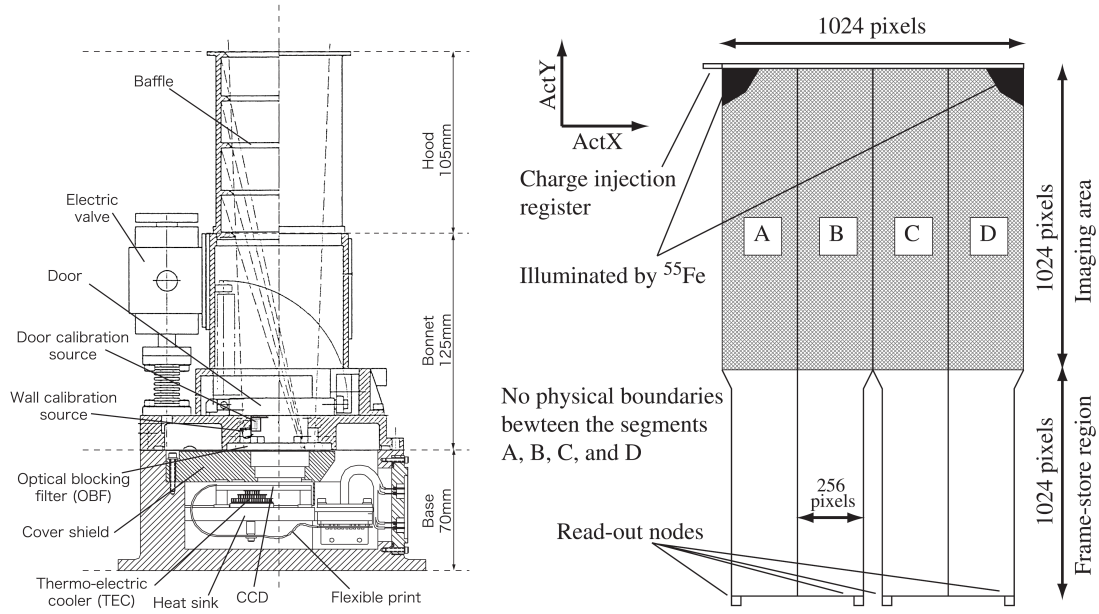

Figure 3.4: Picture (left panel) and side view (right panel) of the *Suzaku* XIS (figure 1 and 2 of Koyama et al. 2007)

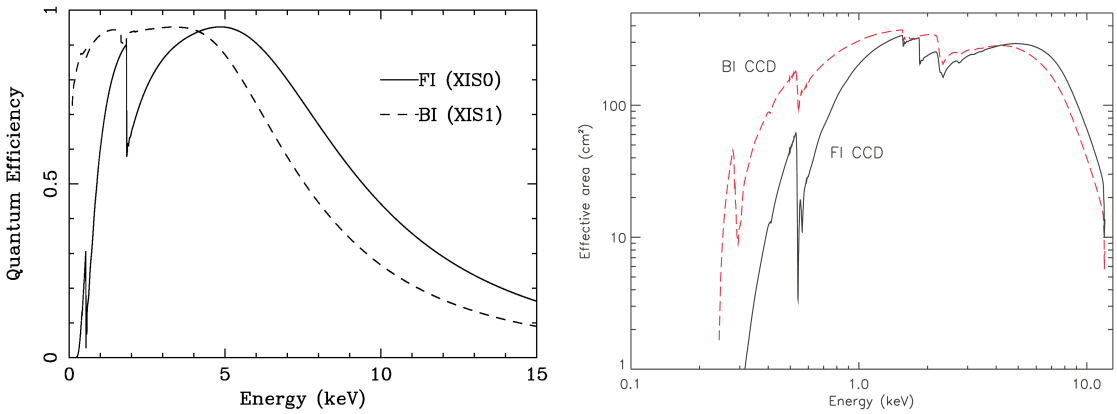

Figure 3.5: Quantum efficiency (left panel) and effective are (right panel) of the *Suzaku* XIS, for both the FI and BI CCDs (figure 4 of Koyama et al. 2007 and figure 3 of Mitsuda et al. 2007).

We show the background count rate of X-ray astronomy CCDs in figure 3.6. The background contains both of the X-ray background (XB) and non X-ray background (NXB), and is normalized with the effective area and the field of view. Since the orbit of *Suzaku* is much lower than that of *Chandra* and *XMM-Newton*, *Suzaku* is less influenced by solar flares and keeps the very stable NXB level. Thus the XIS is sensitive for the observation of spatially extended sources.

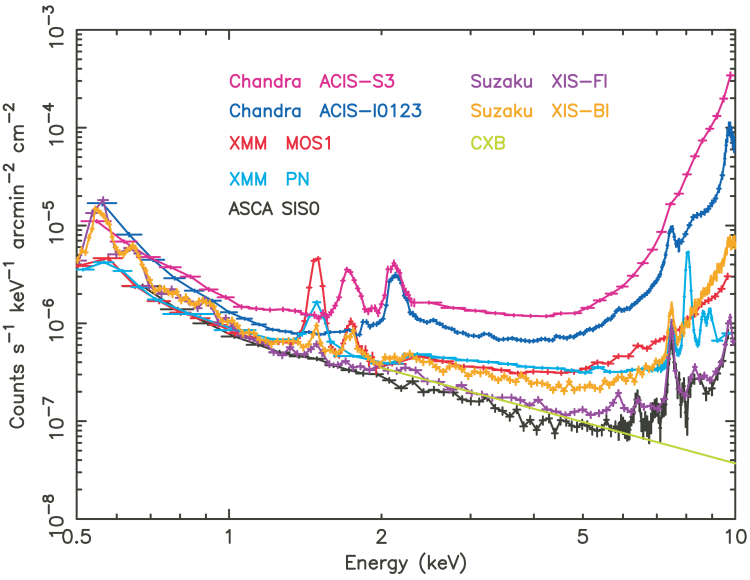

Figure 3.6: The background count rate of CCD detectors onboard recent X-ray satellites. The background is normalized with the effective area and the field of view (figure 5 of Mitsuda et al. 2007).

The XIS 2 was damaged on 2006 November 9, 1:03 UT by a micrometeorite. About 2/3 of the imaging area became out of function. The anomalous area was flooded with a large amount of charge, which leaked somewhere in the imaging region. In spite of efforts by the *Suzaku* team, XIS 2 has not yet recovered. Furthermore, a part of XIS 0 also showed anomaly in Segment A in 2009 June. Therefore, we use data obtained from the XIS 1, 3, and the remaining part of XIS 0 in this thesis.

3.3 Calibration Softwares

The spectra of celestial sources are converted to another forms, depending on the individual detector response. In the case of the XRT + XIS system, the conversion relation between the spectral of celestial sources $M(E)$ and the spectra obtained with the detectors $D(PH)$ is as follows:

$$D(PH) = \int S\, A(E)\, R(E, PH)\, M(E)\, dE \tag{3.1}$$

where S is the geometrical area of the XRT. The term of $A(E)\, R(E, PH)$ is called "response function". Individually, $R(E, PH)$ represents the spectral redistribution matrix from energy to PH, which includes the effect of the transmission of the OBF and the quantum efficiency of the XIS. On the other hand, $A(E)$ is the detection efficiency, which is influenced by the efficiency of the XRT and the thickness of the XIS contamination. In this section, we present the overview of the calibration softwares which generate the response functions.

xisrmfgen

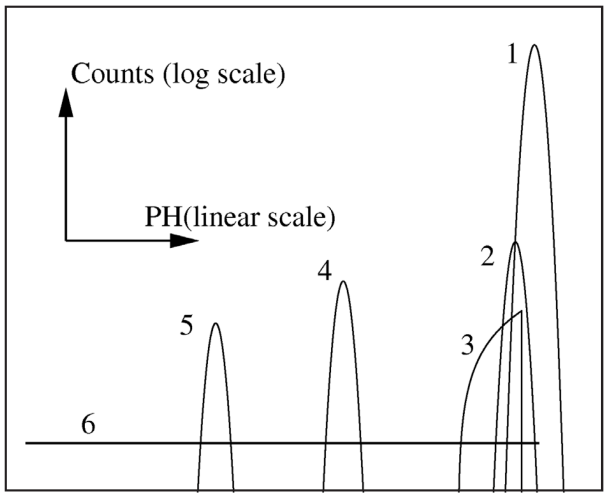

Figure 3.7: Schematic picture of the response function of the XIS. It consists of (1) main peak, (2) sub peak, (3) triangle component, (4) Si escape peak, (5) Si fluorescent peak, and (6) constant component (figure 8 of Koyama et al. 2007).

Figure 3.7 shows the schematic picture of the XIS response to monochromatic X-rays. The monochromatic X-rays are broadened with the energy resolution of the XIS, but the spectral shape is not a simple Gaussian. It consists of (1) main peak, (2) sub peak, (3) triangle component, (4) Si escape peak, (5) Si fluorescent peak, and (6) constant

component. The physical interpretations of these structures are discussed in Matsumoto et al. (2006). These are empirically modeled and included in response matrix files (RMFs), which are generated with *xisrmfgen* (Ishisaki et al. 2007). Since the energy resolution and the quantum efficiency of the XIS change in accordance with the time and the observation mode (SCI on/off), we must choose the optimal RMF for the observation.

xissimarfgen

As we mentioned in section 3.2.1, the XRT has a still larger PSF ($\sim 2'$) than those of *Chandra* and *XMM-Newton*. The sight through the XRT is also influenced by the vignetting. Thus the detection efficiency $A(E)$ is affected by both of the spatial distribution of the celestial sources on the sky, and the accumulation region of the event on the detector (figure 3.8). For the calculation of $A(E)$, the ray-tracing simulator *xissimarfgen* (Ishisaki et al. 2007) is generally employed. *xissimarfgen* calculates the detected photons ($N_{\rm det}$) for a given input ($N_{\rm in}$) by a Monte Callo simulation, and then $A(E)$ is simply described as $N_{\rm det}/N_{\rm in}$. The data of the detection efficiency are included in Ancillary Response Files (ARFs).

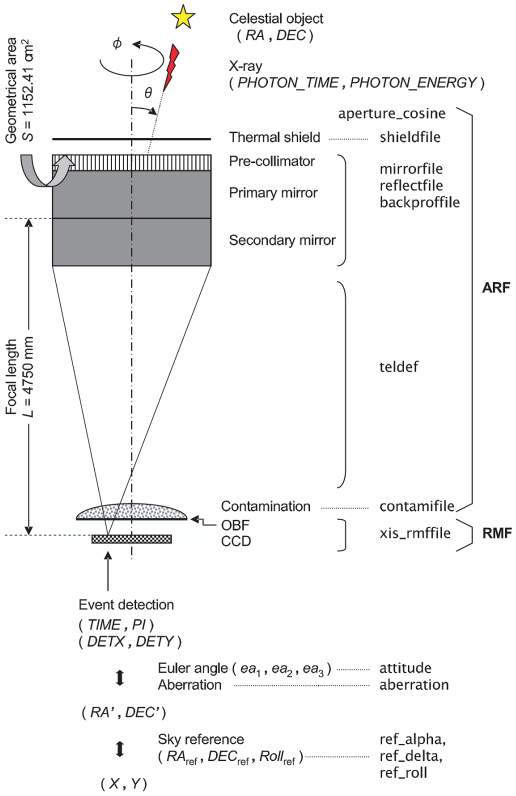

Figure 3.8: Schematic structure of the ARF simulation. (figure 1 of Ishisaki et al. 2007).

Chapter 4

G292.0+1.8

4.1 Previous Results

G292.0+1.8 is a rare source whose SN type is clearly determined as a core-collapse. The first evidence for a core-collapse is that G292.0+1.8 belongs to oxygen-rich SNRs. Optical (Goss et al. 1979) and X-ray (Gonzalez & Safi-Harb 2003; Park et al. 2004) observations measured the large overabundance of oxygen in this SNR, which must be synthesized in a most massive progenitor ($M > 18\,M_{\odot}$). Secondary, G292.0+1.8 has an associated pulsar and pulsar wind nebula (PWN) in the shell (Hughes et al. 2001, 2003; Camilo et al. 2002; Gaensler & Wallace 2003). The spin down age of the pulsar is $\sim$2900 yr (Camilo et al. 2002), consistent with the kinematic age of the SNR (2990 ± 60 yr) estimated with the proper motion of the ejecta filaments (Winkler et al. 2009). The distance to the source was estimated as 6 kpc (Gaensler & Wallace 2003).

The morphology of G292.0+1.8 consists of many small knots and the central belt-like filaments running from the east to the west as shown in figure 4.1 (Park et al. 2007). The central filaments have a normal solar-type composition, suggesting that these are the shocked circumstellar medium (CSM) which was blown out from the progenitor star. Lee et al. (2010) reproduced the intensity profile of the outer CSM region by a slow wind from a red supergiant (RSG) star with the total mass of the wind of 15–40 $M_{\odot}$. The implied progenitor mass ($M > 20\,M_{\odot}$) was in plausible agreement with the previous estimates (Hughes & Singh 1994; Gonzalez & Safi-Harb 2003; Park et al. 2004). The knots have an enhanced metallicity; Si is enhanced in north-northeast, O is enhanced primarily in southeast, Ne is in northwest and southeast, and Mg is in northwest (Park et al. 2002). These knots are probably ejecta origin. The asymmetric distribution of the ejecta elements is interpreted to be non-uniform thermodynamic conditions of the X-ray-emitting ejecta (Park et al. 2007).

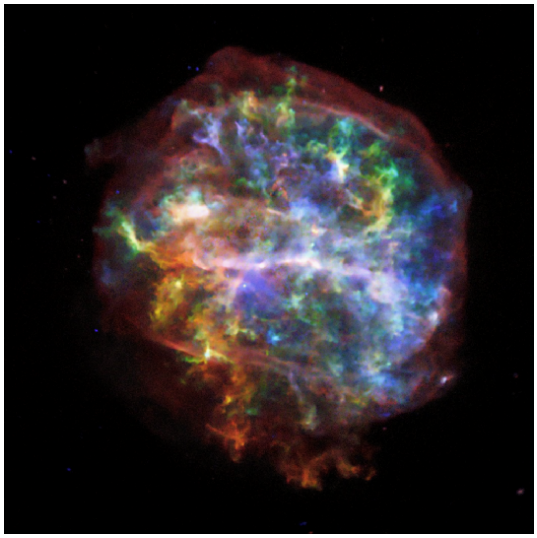

Figure 4.1: *Chandra*/ACIS image of G292.0+1.8. Red, orange, green, and blue colors correspond to narrow energy bands of 0.58–0.71 & 0.88–0.95 keV, 0.98–1.1 keV, 1.28–1.43 keV, and 1.81–2.05 & 2.40–2.62 keV (figure 1 of Park et al. 2007).

The observed emission lines have been limited up to sulfur (S) K-shell line, and the K-shell lines of Ar, Ca, and Fe are not observed yet. Park et al. (2004) proposed that the ejecta are strongly stratified by composition and the reverse shock has not propagated to the inner regions, although the X-ray spectra reported so far are faint in the hard band (except for that of PWN). Therefore, it is important to obtain a broadband spectrum from this SNR with high sensitivity of *Suzaku*.

4.2 Observation and Data Reduction

The Suzaku satellite observed G292.0+1.8 on 2011 July 22-23 with the XIS. The observation log is given in table 4.1. Three of the XISs (XIS 0, 1 ,3) were operated in the normal full-clocking mode with a SCI technique. The amount of the injection charge was 2 keV for the FI CCDs (XIS 0, 3), while it was 6 keV for the BI CCD (XIS 3). The XIS data were reprocessed with the calibration data base (CALDB) released in 2013 September. We used the HEASOFT version 6.9 for the data reduction and XSPEC version 12.8.1 for the spectral analysis. The total exposure time, after the standard screening[1], is about 44 ks.

Table 4.1: Observation log of G292.0+1.8.

Target	Obs. ID	Obs. Date	R.A.	Dec.	Exposure
			(J2000.0)		(ks)
G292.0+1.8	506062010	2011-July-22	$11^{h}24^{m}35.7^{s}$	$-59\,°16\,'20.3\,''$	43.7

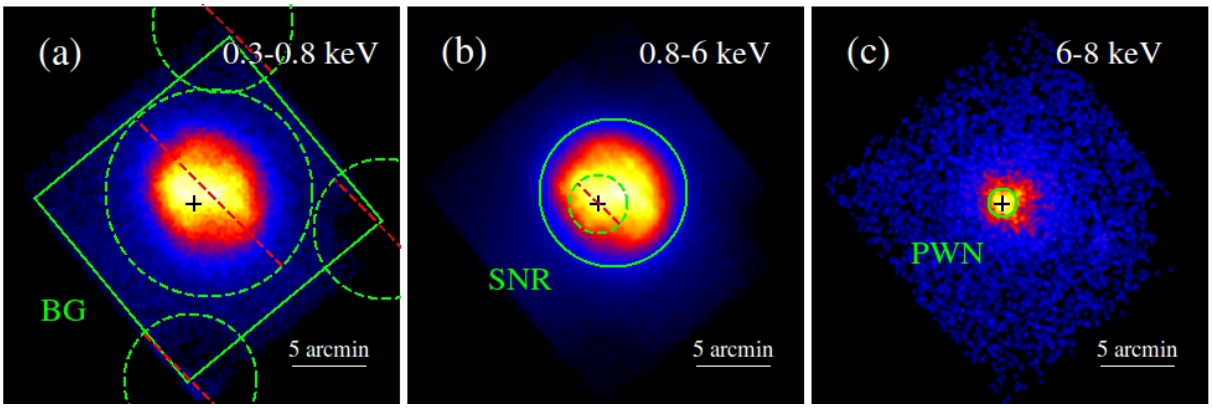

Figure 4.2: XIS images of G292.0+1.8 in the energy bands of (a) 0.3–0.8 keV, (b) 0.8–6 keV, and (c) 6–8 keV, respectively. The geometric center of the PWN (pulsar) is shown with cross marks. In each image, the spectral extraction regions are shown by the green solid and dashed lines.

[1] http://heasarc.nasa.gov/docs/suzaku/processing/criteria_xis.html

4.3 Analyses and Results

4.3.1 Imaging Analysis

Figure 4.2 (a)-(c) shows XIS images in the 0.3–0.8 keV, 0.8–6 keV and 6–8 keV energy bands. We exclude the region of calibration sources, which are located in the XIS corner, and merge the all XIS data to maximize photon statistics. The images are binned with $2\farcs1 \times 2\farcs1$ and smoothed with a Gaussian kernel of $\sigma = 0\farcm45$.

The soft energy band images (figure 4.2 (a) and (b)) show no clear difference each other, but we can barely see a belt-like structure around the equatorial of this SNR, which was formerly reported by the *Chandra* observations (e.g., Park et al. 2007). In the hard energy band above 6 keV (figure 4.2 (c)), we also see a compact X-ray source at (R.A., Dec.) = ($11^{\rm h}24^{\rm m}39^{\rm s}$, $-59^\circ16'20''$). This source corresponds to the pulsar/PWN (Hughes et al. 2001, 2003; Camilo et al. 2002; Gaensler & Wallace 2003).

4.3.2 Spectral Analysis

Combined Analysis of SNR and PWN Spectra

Since the thermal emission from the SNR plasma and the non-thermal emission from the pulsar/PWN coexist in G292.0+1.8, we make two source spectra from different regions. One is extracted from the solid circle (radius of $1'$) as shown in figure 4.2 (c) (here PWN region), and the other is from the solid circle (radius of $5'$) excluding the dashed circle (radius of $2'$) as shown in figure 4.2 (b) (here SNR region). We also make the background (BG) spectrum from the whole FOV of the XIS (solid square), excluding the dashed circle (radius of $7'$) as shown in figure 4.2 (a) (here BG region). This larger radius than that of the SNR region is employed to avoid the contamination from the SNR because of the PSF of the *Suzaku*/XRT ($\sim 2'$). We also exclude the region of calibration sources, which are shown by the dashed circles in the XIS corner. For all the regions of the PWN, SNR, and BG, we separately make the NXB spectra using *xisnxbgen* in the HEASOFT package.

We make an X-ray background (XB) spectrum from the BG region by subtracting the relevant NXB. The spectra from the SNR and PWN regions are also made by subtraction of relevant NXBs for these regions. From these spectra, we subtract the XB spectrum assuming the uniform distribution within the FOV of the XIS after the correction of the vignetting effect. The resulting spectra of the SNR and the PWN regions in figure 4.3 show many emission lines. From the center energy of these lines, we identify them to be O Lyα, Ne Heα, Ne Lyα, Mg Heα, Mg Lyα, Si Heα, and S Heα. Thus the spectra should be composed of an optically thin hot plasma with the temperature of $kT_{\rm e} = 1$ keV

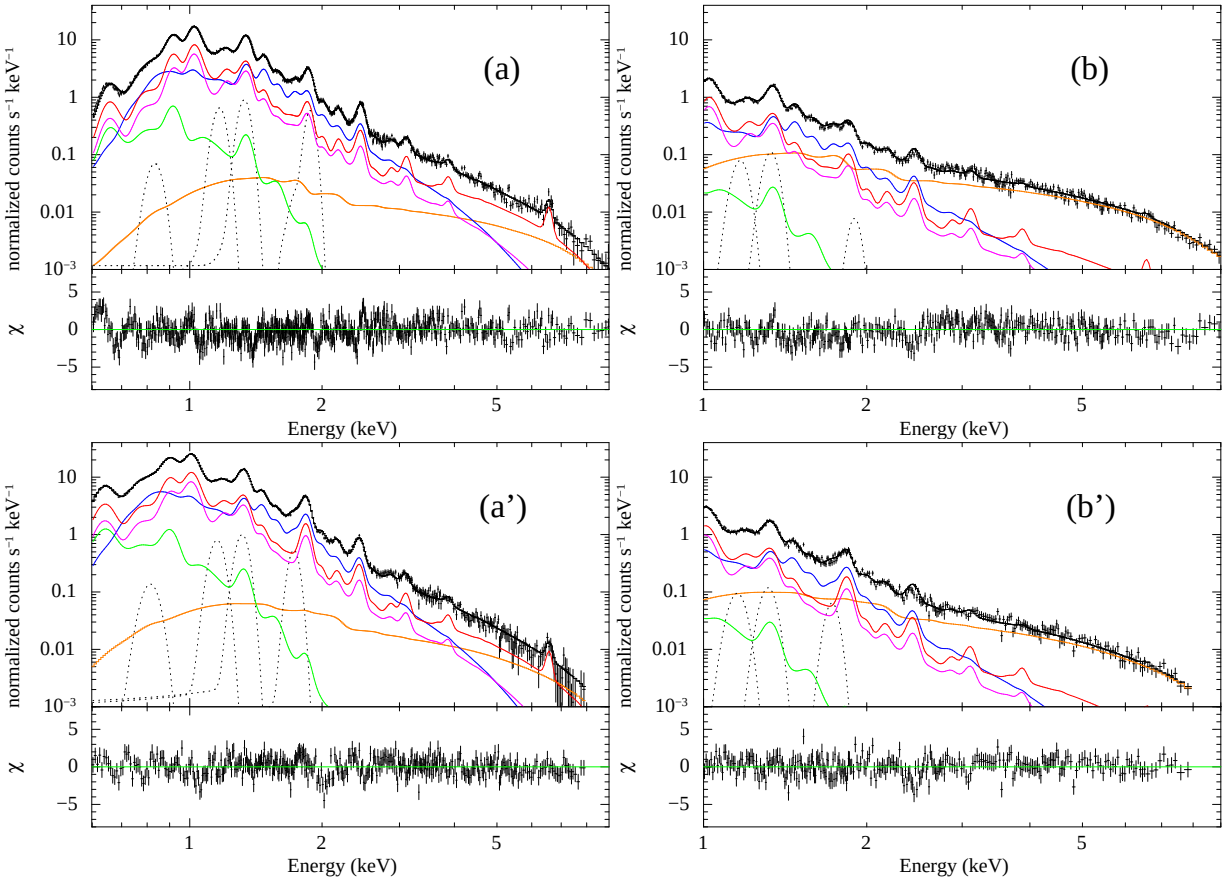

Figure 4.3: Spectra obtained from the SNR and PWN regions of G292.0+1.8. (a) and (a') are the SNR region spectra for FI and BI, respectively. (b) and (b') are the same panels but for the PWN region. The red and magenta lines are the best-fit 2-VPSHOCK, while the blue and green lines are the best-fit 2-APEC. The orange line and the dotted lines are the power-law and the Gaussian lines. The residuals are shown in the lower panel.

(Gonzalez & Safi-Harb 2003; Park et al. 2004; Lee et al. 2010). In the spectrum of the SNR region, we find line-like features ad 3.1, 3.9, and 6.6 keV, which are likely K-shell transition lines of Ar, Ca, and Fe. The Fe line at 6.6 keV is particularly clear. Therefore, in addition to the 1 keV plasma (low-kT_e plasma), a higher temperature plasma (high-kT_e plasma) to emit K-shell lines of Ar, Ca, and Fe should be prevailing in the SNR region. We call these two plasmas the SNR components. The X-rays of the SNR components distribute not only in the SNR region but also in the PWN region. On the other hand, according to the observation with *Chandra*, the PWN is compact of 30″–45″(Gonzalez & Safi-Harb 2003), and the spectrum is fitted with a power-law model of $\Gamma \sim 1.7$ (Hughes et al. 2001), indicating its non-thermal nature. We call this power-law emission the PWN component. The spectrum extracted from the PWN region contains both the SNR component and the PWN component. The spectrum from the SNR region, on the other

hand, is contaminated by X-rays of the PWN component due to the PSF of the *Suzaku* XRT. We hence simultaneously fit the spectra in the SNR and the PWN regions with the combined model, SNR plus PWN components. The ARFs employed in the fit are generated with *xissimarfgen*. The ARF for the PWN component is generated from the *Chandra* image in the 4–7 keV band, while that for the SNR component is made using the thermal emission of the *Chandra* image (0.6–2.0 keV), where the emissions of the PWN component are excluded. The energy range of the PWN and the SNR regions are 1–9 keV and 0.6–9 keV, respectively. The former energy band is selected because the contamination of the SNR component in the PWN region becomes large below 1 keV. Considering the background level, we also ignore the energy band upper than 9 keV for the FI, while 8 keV for the BI.

Park et al. (2004) and Gonzalez & Safi-Harb (2003) reported that the spectra are significantly different from position to position. Therefore, the integrated spectrum from the entire SNR cannot be described by any single component model fit. We thus search for a many components model, starting from one component model then adding another component one by one, monitoring how much χ^2 is reduced. We use VPSHOCK (Borkowski et al. 2001) to represent multi-$n_{\rm e}t$ non equilibrium ionization (NEI) plasma, where $n_{\rm e}$ and t are the plasma density and elapsed time after shock heating. In order to fine-tune the calibration errors, between XIS 0, 1 and 3, the gains and normalizations are set to be independent parameters for each XIS.

A 1-VPSHOCK model fails with extreme large χ^2_ν (d.o.f.) = 7.25 (2071). A 2-VPSHOCK model is largely improved the fitting with χ^2_ν (d.o.f.) = 2.62 (2060), but still unacceptable. We thus add the third VPSHOCK component (VPSHOCK 1, 2, and 3), then χ^2_ν (d.o.f.) is improved to 2.48 (2049). Although the decrease of χ^2_ν is only $\delta = 0.14$, the decrease of χ^2 is 324, which is statistically highly significant. In fact, we check the significance using an F-test tool in the XSPEC package, then this process is significant with better than 0.01 % level. Although errors are large, the best-fit abundances in VPSHOCK 1 and 2 are the same with each other. We hence link the abundances in these two VPSHOCK components. Also abundances of Ni and Ca are linked to Fe and Ar, respectively. Since $n_{\rm e}t$ of VPSHOCK 3 is 10^{12-13} cm^{-3}s^{-1}, we replace this model by an APEC model (CIE model). The χ^2_ν (d.o.f.) of this fit is 2.51 (2062), leaving large residuals in the low energy band. We thus add another APEC component linking the abundances to the APEC component in the 3 component model. This another APEC improve the χ^2_ν (d.o.f.) to 2.34 (2060), the F-test statistical significant is even better than the previous process. Though this χ^2_ν is still large from a statistical point of view, its value would be due to non-negligible systematic errors. In fact, we find line-like residuals

at about 0.82, 1.2, 1.3 and 1.8 keV for both FI and BI, and 1.7 keV for BI. The 1.7 and 1.8 keV line structures are due to the well-known problem of the response function near the neutral Si K-edge energy at 1.84 keV (e.g., Yamaguchi et al. 2009). The other line structures would be due to the incompleteness of the VPSHOCK model code. The lines at 0.82, 1.2, and 1.3 keV correspond to Fe-L complex (e.g., Uchida et al. 2013; Nakashima et al. 2013). We thus add extra 5 Gaussians to compensate these line-like residuals. The normalization factors of these Gaussians are linked between FI and BI, but that of the 1.7 and 1.8 keV lines are treated as an independent parameters between FI and BI (Suchy et al. 2011). The calibration errors of the contamination on the optical blocking filter has some problems in the low energy band[2]. For a fine-tuning of the cross errors between the FI and BI CCDs, we allow the $N_{\rm H}$ value in the BI CCD to be independent from the FI CCDs. This results of the combined fits by this model are shown in figure 4.3. The best-fit parameters are given in table 4.2. We finally improve the χ^2_ν (d.o.f.) to 1.39 (2059). The F-test statistical significance is better than 0.01 %. Thus, we regard that this model (2-VPSHOCK + 2-APEC + PL + 5-Gaussians) is a reasonable approximation for the SNR and PWN spectra, and apply in the following analysis and discussion.

[2]http://www.astro.isas.jaxa.jp/suzaku/doc/suzaku_td/

Table 4.2: Best-fit parameters for the combined analysis of the SNR and PWN regions of G292.0+1.8.

Component	Parameter	Value
Absorption	$N_{\rm H}$ (10^{21} cm^{-2})	4.44±0.19 (FI)
		4.11±0.19 (BI)
Power-Law	Photon index	1.91±0.03
	Absorbed flux†	3.71±0.17
	Unabsorbed flux†	3.80±0.18
APEC 1	kT_e (keV)	0.17±0.04
	O	0.58±0.30
	Ne	0.74±0.56
	Mg	1.69±0.27
	Si	0.80±0.16
	S	0.83±0.50
	Ar (=Ca)	< 1.21
	Fe (=Ni)	0.36±0.09
	VEM (10^{11} cm^{-5})‡	230±160
APEC 2	kT_e (keV)	0.72±0.01
	VEM (10^{11} cm^{-5})‡	105±15
VPSHOCK 1	kT_e (keV)	1.07±0.19
	O	8.5±3.5
	Ne	17.8±6.1
	Mg	6.3±2.4
	Si	3.1±1.0
	S	2.9±1.4
	Ar (=Ca)	5.2±2.4
	Fe (=Ni)	1.7±0.5
	$n_e t$ (10^{11} cm^{-3} s)	3.0±2.6
	VEM (10^{11} cm^{-5})‡	6.3±2.3
VPSHOCK 2	kT_e (keV)	2.67±0.41
	$n_e t$ (10^{11} cm^{-3} s)	0.86±0.19
	VEM (10^{11} cm^{-5})‡	5.2±2.0
χ^2_ν (d.o.f.)		1.39 (2059)

Notes. Abundances are in units of solar.

† Flux (10^{-4} photons s^{-1} cm^{-2}) in the 4–8 keV band.

‡ Volume emission measure, $\int n_e n_{\rm H} dV/(4\pi D^2)$, where V and D are the emitting volume (cm^3) and the distance to the source (cm), respectively.

Analysis of Spatially Resolved Spectra

In order to examine spatial asymmetry of the elements in the SNR, we make spatially-resolved spectra. Since the spatial resolution of Suzaku is limited compared to the size of G292.0+1.8 ($\sim 9' \times 9'$), we crudely divide the SNR into three: the center, north and south regions as shown in figure 4.4 by the solid lines. The spectra are given in figure 4.5. We find no significant differences, except a hint of Fe Kα flux variations among the 3 regions. For quantitative estimate, we fit with the same model and the method given in subsection 4.3.2.1, but $N_{\rm H}$s are fixed to the best-fit values in table 4.2. We obtain a nice fit with χ^2_ν (d.o.f.) of 1.32 (973), 1.32 (1055) and 1.35 (1022), for the north, center and south regions, respectively. The best-fit spectra are given in figure 4.5 by the solid histograms. The best-fit parameters, including abundances, show no spatial-difference within their large errors (typical errors for the abundances are $\sim$50%). The only spatial-difference is found in the Fe abundances of the NEI plasma (2-VPSHOCK), which are 1.7$\pm$0.5, 0.75$\pm$0.22 and 1.0$\pm$0.4, for the north, center and south regions, respectively.

The Fe abundance in the NEI plasma may be affected by the flux of the power-law component (PWN component), because the continuum emission of the ejecta is equal or even less than the power-law emission except the north region (see figure 4.5). We therefore re-fit the spatially-resolved spectra, changing the normalizations of the PWN component by $\pm$5% of the value in table 4.2, and fixing the photon index of $\Gamma = 1.91$. The fit gives no essential changes of the Fe abundances from those of the original value.

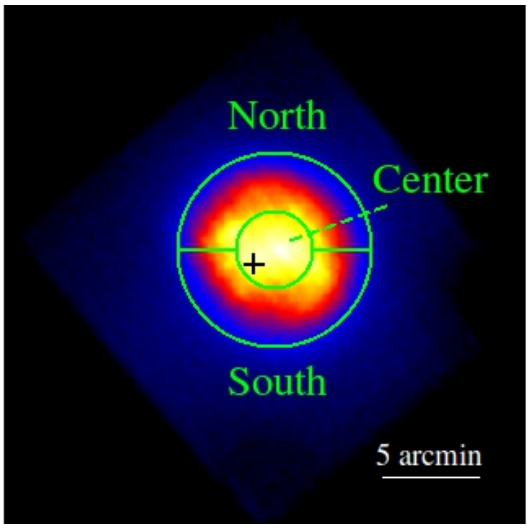

Figure 4.4: Region definition for the spatial analysis of G292.0+1.8. Each region is shown in the green solid line.

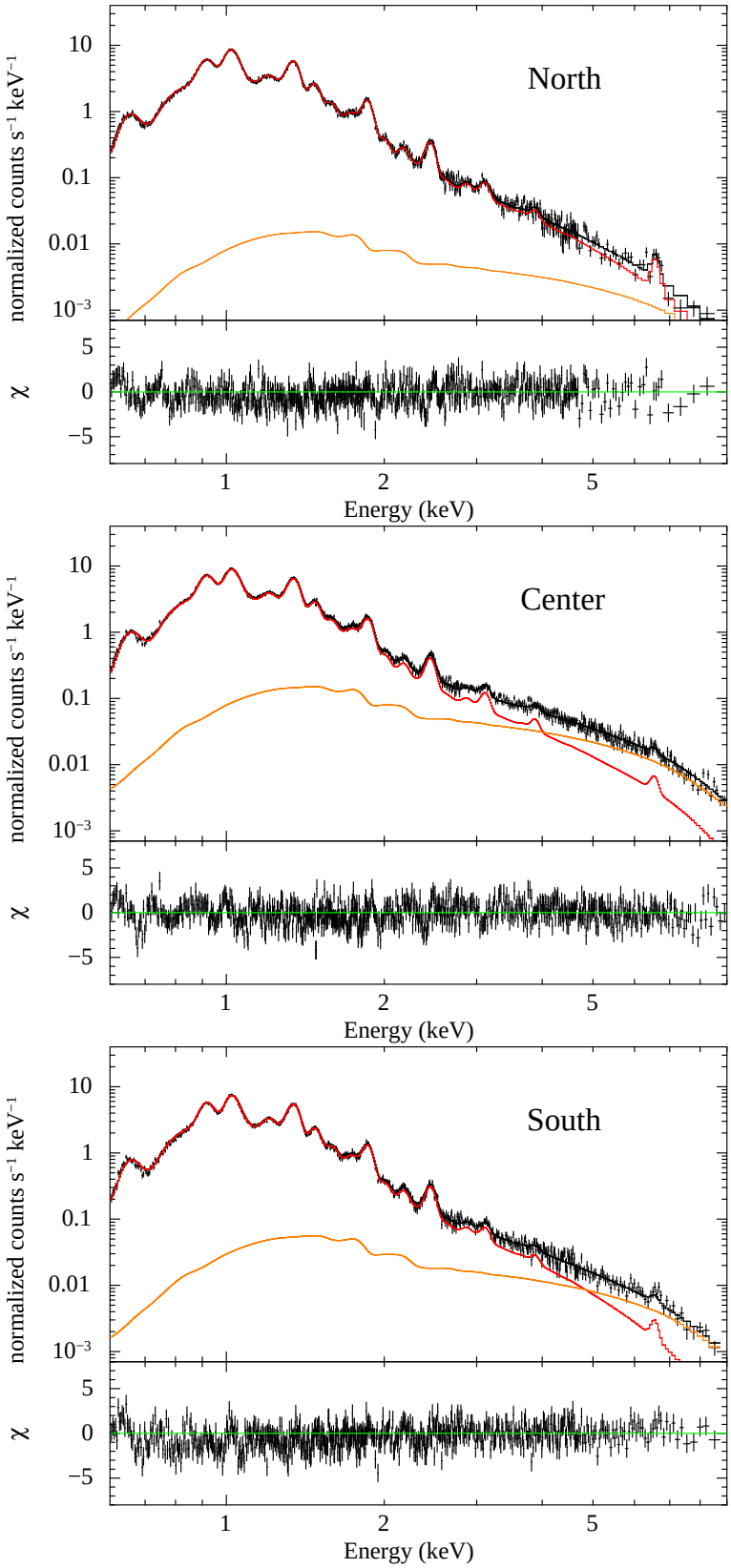

Figure 4.5: Spectra obtained from the North, Center, and South regions of G292.0+1.8. Only the FI spectra are shown. Each spectrum is fitted with the same model as the combined analysis of the SNR and PWN with adding the best-fit PWN spectrum. The red and orange lines represent the SNR and PWN component, respectively.

4.4 Discussion

4.4.1 Origin of the Plasma Components

In the spectral fitting of G292.0+1.8, we find two type plasmas in CIE and NEI conditions; the 2-APEC ($kT_{\rm e} \sim 0.2$ and 0.7 keV) and the 2-VPSHOCK ($kT_{\rm e} \sim 1$ and 2.5 keV) plasmas. We call these two type plasmas, the low-$kT_{\rm e}$ plasma and the high-$kT_{\rm e}$ plasma, respectively. Since the low-$kT_{\rm e}$ plasma has nearly solar abundances for all elements and the high-$kT_{\rm e}$ plasma has super-solar abundances (see table 4.2), these would be the CSM plus ISM and the ejecta origin of a core-collapse SN, respectively. *Chandra* spectra from many selected regions of bright small spots are described by 1-VPSHOCK model with super-solar abundances (Park et al. 2004), while those from the faint outer-most shell are 1 or 2-VPSHOCK model with sub-solar to solar abundances (Gonzalez & Safi-Harb 2003; Lee et al. 2010). These results of "no-CIE" plasma are in contrast to the existence of CIE ($\sim$ solar) components in the *Suzaku* spectra. Since the *Chandra* results are from selected spots or filaments and those of *Suzaku* are from the entire SNR region, we suspect that our CIE plasmas are prevailing over the entire SNR except the outer-most shell, while the bright spots are dominated by the VPSHOCK plasma.

4.4.2 Fe K-shell Line

We discover Fe K-shell line at 6.6 keV in the eject plasma for the first time. The energy indicates that ionization state of Fe is around B-like. This medium ionization state is similar to another young core-collapse SNR, Cas A, but is in contrast to nearly Ne-like states in young well known Type Ia SNRs, Tycho, Kepler, and SN 1006.

4.4.3 Relative Abundances and Mass of the Ejecta

Figure 4.6 is the abundance plot of the ejecta for O, Ne, Mg, Si, S, Ar and Fe relative to Si (from table 4.2) together with those of the core-collapse SN model in various progenitor masses (Woosley & Weaver 1995). We see that the observed abundance pattern is globally in agreement with the model of 30–35 $M_{\odot}$. These mass range of the progenitor star confirm the previous report of 30–40 $M_{\odot}$ (Gonzalez & Safi-Harb 2003), which was estimated based on the limited information of non-detection of the explosively synthesized heavy elements such as Ar, Ca and Fe. Assuming the plasma volume as $6.0 \times 10^{58}\,{\rm cm}^3$, the ejecta mass is estimated to be $\sim 29\, f^{0.5}\, M_{\odot}$, where f is a filling factor. It is consistent with the mass estimated with the abundance pattern. One may argue that core-collapse SN of a massive progenitor 30–35 $M_{\odot}$ may leave a black hole rather than a neutron star. However,

other observations show that a neutron star can be still formed from even these massive progenitor stars (Muno et al. 2006).

4.4.4 Spatial Distribution of the Ejecta

Although Park et al. (2004) and Gonzalez & Safi-Harb (2003) reported significant spatial variations in the sub-arcmin scale, we find no significant and systematic variations in the spatial scale over arcmin. In fact, the best-fit abundances of most of the heavy elements show no variations within their typical errors of 50%. Nevertheless, we find marginal evidence of spatial variation of Fe in the ejecta; the north region is enhanced compared to that of the center region. Since the position of the neutron star (PWN) is off-set to southeast from the geometrical SNR center (Park et al. 2007), it would be conceivable that Fe from the core region would be ejected to the opposite northwest direction. Our observational result of the Fe variation is marginal to support this off-set effect due to large errors. To establish this kick-off scenario, we need higher quality observations.

4.4.5 PWN

The best-fit spectral parameters of the PWN, the photon index and unabsorbed flux (4–8 keV) are 1.91±0.03 and (3.80±0.18)×10^{-4} photons s^{-1} cm^{-2}, respectively. The photon index is steeper than that of the pulsar (1.6–1.7, Hughes et al. 2001, 2003). Probably the index increases as the distance from the central pulsar increases (e.g. Slane et al. 2000). The PWN flux is 52% of the total flux (4–8 keV) from the whole SNR ((7.30±0.06)×10^{-4} photons s^{-1} cm^{-2}). This ratio is slightly smaller than 66%, determined with the high spatial resolution observation of *Chandra* (Hughes et al. 2001). This difference, however, would be within uncertainty range due possibly to the NXB and CXB subtraction[3], and/or other systematic cross errors including different data reduction processes between *Suzaku* and *Chandra*. Thus our simultaneous fitting analysis properly estimates the flux and spectra of both the SNR and the PWN, although the spatial resolution of *Suzaku* is limited to completely separate the emissions from these two sources.

[3]The 4-8 keV band fluxes of the BG region are about 8% and 70% of the whole SNR regions for the data of *Suzaku* and *Chandra*, respectively

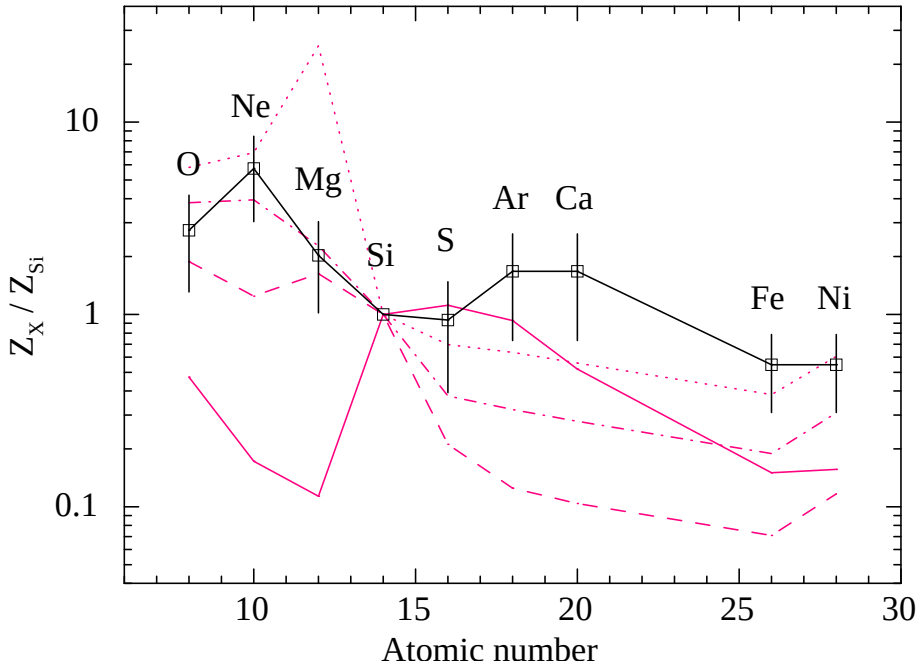

Figure 4.6: Abundance pattern of high-kT_e plasma in G292.0+1.8. The solid black line shows abundance ratios of O, Ne, Mg, Si, S, Ar, and Fe relative to Si in the high-kT_e plasma (ejecta). The red, green, blue, light blue, and magenta dashed lines represent core-collapse models with progenitor masses of 20, 25, 30, 35, and 40 $M_\odot$, respectively (Woosley & Weaver 1995).

4.5 Summary

We have analyzed the *Suzaku*/XIS data obtained from G292.0+1.8. The results are summarized as follows:

1. We confirm that the thermal X-ray emission from G292.0+1.8 consists of two type plasmas in CIE and NEI conditions.

2. The NEI plasma includes K-shell line from B-like Fe, with super solar abundances for O, Ne, Mg, Si, S, Ar, and Fe. Therefore this plasma is likely the ejecta origin of the CC SNR.

3. Using the abundance pattern of the ejecta, we confirm the progenitor mass to be 30–35 $M_{\odot}$.

4. The CIE plasma has nearly solar abundances for all the relevant elements, and hence is likely the CSM and ISM origin.

Chapter 5

G290.1−0.8

5.1 Previous Results

G290.1−0.8, also known as MSH 11-61A, is a member of MM SNRs in our galaxy. This SNR is discovered in the radio band by Kesteven (1968). The radio image obtained with the Molonglo Observation Synthesis Telescope (MOST) revealed its asymmetric geometry elongated in the southeast and the northwest direction with the size of $15' \times 10'$ (Kesteven & Caswell 1987; Milne et al. 1989). Filipovic et al. (2005) reported that the NANTEN CO data suggest a dense molecular cloud in the southeast of the SNR. Reynoso et al. (2006) studied the gas distribution and kinematics in detail, and suggested that the SNR probably lies in the Carina arm, at a distance of 7 ± 1 kpc.

In X-ray, G290.1−0.8 was found by the Galactic SNRs survey with the Einstein Observatory (Seward 1990). *ASCA* found that the X-ray is a thermal plasma emission, and then classified this SNR as a member of the MM SNRs (Rho & Petre 1998). García et al. (2012) analyzed the *XMM-Newton* and the *Chandra* data focusing on the asymmetric geometry of the SNR. The *Chandra* image of G290.1−0.8 is shown in figure 5.1. They concluded that the plasmas in the southeast and the northwest regions are IPs, while those in the other regions are CIEs. Employing these X-ray results and the H_I map, they proposed that the SNR is due to a core collapse of a high mass progenitor with a bipolar wind.

Pavan et al. (2011) discovered a hard X-ray source, IGR J11014-6103, about 10′at the southwest of G290.1−0.8. Halpern et al. (2014) detected the pulsation of 62.8 msec. This pulsar has a prominent jet extending toward the northwest and a possible counter jet to the southeast (Pavan et al. 2014). It also has a bow shock tail pointing to the center of G290.1−0.8. Moreover, the absorption (N_H) of the pulsar is similar to that of G290.1−0.8. Thus IGR J11014-6103 would be an associated pulsar of G290.1−0.8, a compact remnant

of a CC SN. Halpern et al. (2014) estimated the spin-down age to be 116 kyr, significantly larger than the previous estimation of the SNR age of 10–20 kyr (Slane et al. 2002).

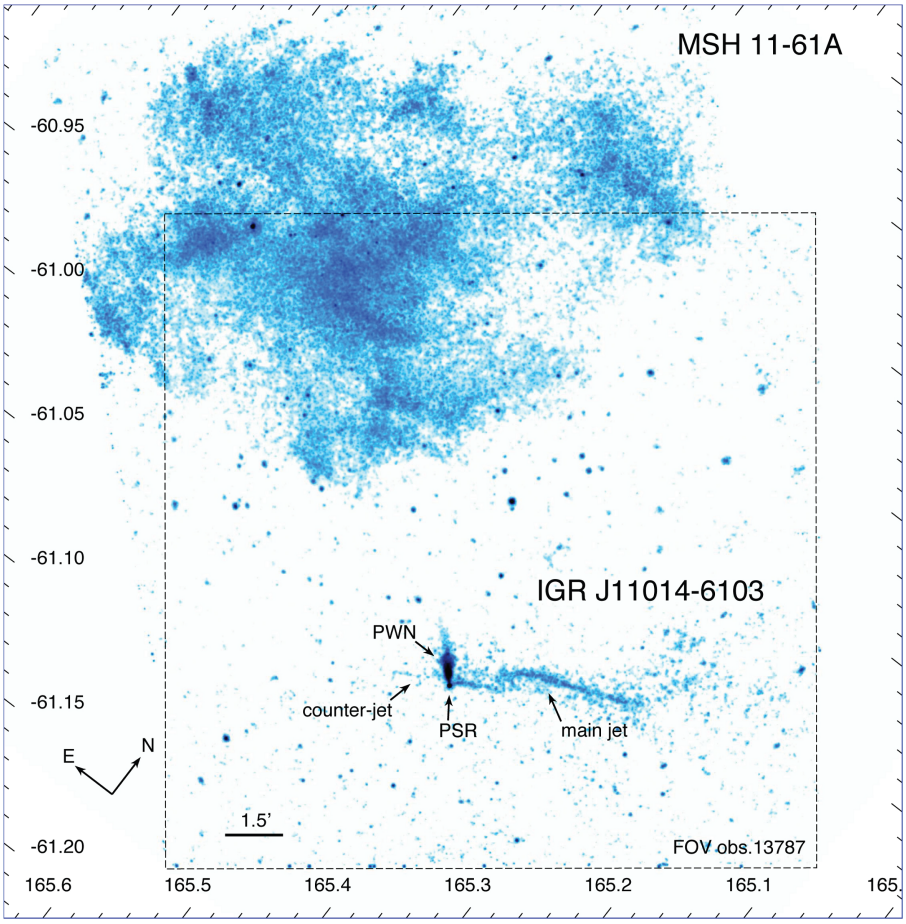

Figure 5.1: *Chandra*/ACIS image of G290.1−0.8 and IGR J11014-6103. This figure is taken from Pavan et al. (2014).

5.2 Observation and Data Reduction

The Suzaku satellite observed G290.1−0.8 on 2011 June 25 with the XIS. The observation log is given in table 5.1. Three of the XISs (XIS 0, 1 ,3) were operated in the normal full-clocking mode with a SCI technique. The amount of the injection charge was 2 keV for the FI CCDs (XIS 0, 3), while it was 6 keV for the BI CCD (XIS 3). The XIS data were reprocessed with the calibration data base (CALDB) released in 2014 February. We used the HEASOFT version 6.15 for the data reduction and XSPEC version 12.8.2a for the spectral analysis. The total exposure time, after the standard screening, is about 110 ks.

Table 5.1: Observation logs of G290.1−0.8 and 1E1048.1−5937.

Target	Obs. ID	Obs. Date	R.A.	Dec.	Exposure
			(J2000.0)		(ks)
G290.1−0.8	506061010	2011-June-25	$11^{h}02^{m}58.7^{s}$	$-60\,°53\,'18.2\,''$	110.6
1E1048.1−5937	403005010	2008-Nov-30	$10^{h}50^{m}10.9^{s}$	$-59\,°50\,'21.8\,''$	100.4

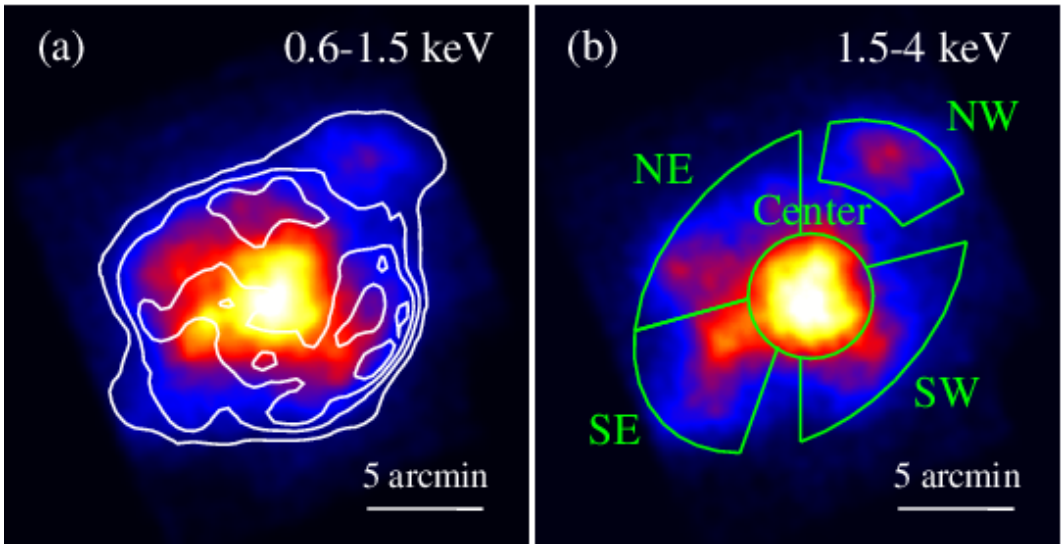

Figure 5.2: XIS images of G290.1−0.8 in the energy bands of (a) 0.6–1.5 keV and (b) 1.5–4 keV, respectively. The 843 MHz radio profile is overlaid on (a) with white contours. The spectral extraction regions are shown with the green lines in (b).

5.3 Analyses and Results

5.3.1 Imaging Analysis

Figure 5.2 (a)-(b) show XIS images in the 0.6–1.5 keV and 1.5–4 keV energy bands. We combine the all XIS data to maximize photon statistics. The images are binned with $2.''1 \times 2.''1$ and smoothed with a Gaussian kernel of $\sigma = 0.'5$. We overlay the 843 MHz radio profile obtained by the MOST with white contours.

We can see a center-filled X-ray emission in the radio shell, which is the typical feature of the mixed-morphology SNRs. The diffuse emission from G290.1−0.8 is mainly found in the 0.6–4 keV band; no significant emission except the X-ray background is found above this energy band. We see ear-like structures at the southeast and the northwest that are prominent in the 1.5–4 keV band.

5.3.2 Spectral Analysis

Background Estimation

Since G290.1−0.8 extends widely over the field of view (FoV) of the XIS, the X-ray background region is not available from the same FoV. Therefore, we use the data from a nearby sky field: a blank region in the field of the X-ray pulsar 1E1048.1−5937. We extract the background data from the whole FoV of the XIS, excluding the pulsar region of $4'$ radius. We generate the NXB using *xisnxbgen* and subtract it from the extracted spectrum. This background spectrum consists of the cosmic X-ray background (CXB), the Galactic ridge X-ray emission (GRXE), and the Galactic halo (GH) (e.g., Kushino et al. 2002; Kaneda et al. 1997; Henley & Shelton 2013). Then, we fit the spectrum with a model of [Abs1 × power-law (CXB) + Abs2 × (APEC (HP) + APEC (LP)) + Abs3 × APEC (GH)], where the apec is a CIE plasma model in the XSPEC. The second term is the GRXE component, which is represented with a 2-CIE model, a high-temperature plasma (HP; $kT_{\rm e} \sim 7$ keV) + a low-temperature plasma (LP; $kT_{\rm e} \sim 1$ keV) (Kaneda et al. 1997; Uchiyama et al. 2013). The CXB component parameters are fixed at those in Kushino et al. (2002). The model is nicely fitted with χ^2_ν (d.o.f.) = 1.08 (1111), where χ^2_ν and d.o.f. represent the reduced chi square and the degree of freedom. The best-fit spectrum and parameters are summarize in figure 5.3 and table 5.2.

Since the Galactic coordinate of G290.1−0.8 ($(l, b) = (290.^\circ1, -0.^\circ75)$) is slightly different from that of the 1E1048.1−5937 ($(l, b) = (288.^\circ3, -0.^\circ52)$) field, we fine-tune the GRXE flux using the spatial structure of the GRXE. Kaneda et al. (1997) estimated its Galactic latitude distribution by an exponential function with the e-folding values of

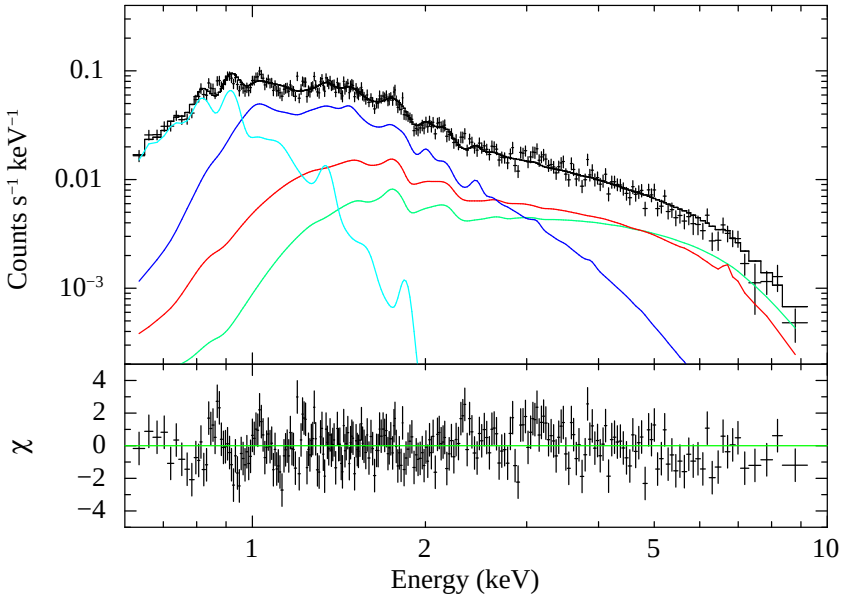

Figure 5.3: Background spectrum (FI) for G290.1−0.8. The spectrum is extracted from the nearby blank region in the field of 1E1048.1−5937. The color lines represent the models of the CXB (green), HP (red), LP (blue), and GH (cyan).

Table 5.2: Best-fit parameters for the background spectrum of 1E1048.1−5937.

Component	Parameter	Value
Abs1	$N_{\rm H}$ (10^{21}cm^{-2})	13.2 (fixed)
CXB	photon index	1.4 (fixed)
	flux†	1.94 (fixed)
Abs2	$N_{\rm H}$ (10^{21}cm^{-2})	7.0 ± 0.8
HP	$kT_{\rm e}$ (keV)	7 (fixed)
	all elements	< 0.2
LP	$kT_{\rm e}$ (keV)	1 (fixed)
	all elements	0.10 ± 0.02
Abs3	$N_{\rm H}$ (10^{21}cm^{-2})	4.1 ± 0.7
GH	$kT_{\rm e}$ (keV)	0.16 ± 0.01
	O	$0.06^{+0.03}_{-0.02}$
	Ne	0.17 ± 0.02
	Mg	$0.28^{+0.15}_{-0.14}$
	Others	1 (fixed)
χ^2_ν (d.o.f.)		1.08 (1111)

† Flux (10^{-11} erg cm^{-2} s^{-1} deg^{-2}) in the 2–10 keV band.

$\sim 0.^\circ 5$ and 1° for the HP and the LP, respectively. Uchiyama et al. (2013) estimated the Galactic longitude distribution by an exponential function with the e-folding values of $\sim 50^\circ$ both for the HP and the LP. Then, we can estimate the fluxes of the HP and the LP at G290.1−0.8 to be $\sim 60\,\%$ and $\sim 80\,\%$ of those at 1E1048.1−5937 field.

Analysis of Spatially Resolved Spectra

Since the spatial structure of G290.1−0.8 is asymmetric (Kesteven & Caswell 1987), we divide the SNR into the Center, NW, SE, NE, and SW regions as shown in figure 5.2 (b). The NXB-subtracted spectra are shown in figure 5.4. We first apply a 1-component IP adding the background model spectrum given in the previous subsection. We use the plasma code (VVRNEI) in the XSPEC package. The VVRNEI calculates the spectrum of a non-equilibrium ionization plasma after a rapid transition of the electron temperature from $kT_{\rm init}$ to $kT_{\rm e}$. The initial plasma temperature $kT_{\rm init}$ is fixed at 0.01 keV. The present electron temperature $kT_{\rm e}$, ionization timescale $n_{\rm e}t$, emission measure, and column density $N_{\rm H}$ are free parameters, where $n_{\rm e}$ and t are an electron density and an elapsed time after the initial state. The abundances of Ne, Mg, Si, S, Ar, and Fe are also allowed to vary freely, while the abundances of Ca and Ni are linked to those of Ar and Fe, respectively. The CXB flux is free within the fluctuation expected for the area of each region (Kushino et al. 2002), while the other background parameters are fixed to the values in the table 5.2.

This fit, however, leaves a large residual around 1.2 keV. This residual is due to the error of Fe-L lines in the current XSPEC code (e.g., Borkowski et al. 2006; Yamaguchi et al. 2011). We therefore add a Gaussian line at 1.2 keV. The χ^2_ν values are improved to 1.19 (Center), 1.24 (NW), 1.08 (SE), 1.06 (NE), and 1.10 (SW). Contrary to the nice fits for the SE, NE and SW regions, the IP models for the Center and particularly the NW spectra are rejected with the large χ^2_ν values. For example, the fits of the NW spectra leave hump-like residuals around 2.7 keV and line-like residuals at 2.0 keV (see the middle panels of the NW spectra in figure 5.4). The former residuals correspond to the RRC of Si, while the latters are Si Lyα (2.01 keV). These residuals indicate that the ionization state of Si is higher than that expected from the IP model. In particular, the RRC structure of Si strongly suggests that the plasma is in a recombining phase.

We therefore apply RP models for the spectra of the Center and the NW (1-component RP plus a Gaussian line). Unlike the fixed initial temperature $kT_{\rm init}$ of 0.01 keV in the IP fit, the RP fit assumes a high temperature in the initial phase of the plasma. The RP fit assumes a rapid electron cooling of $kT_{\rm init} \rightarrow kT_{\rm e}$ at an early phase of the plasma evolution. Thus the free parameters are $kT_{\rm init}$, $kT_{\rm e}$, and $n_{\rm e}t$, where t is an elapsed time after the

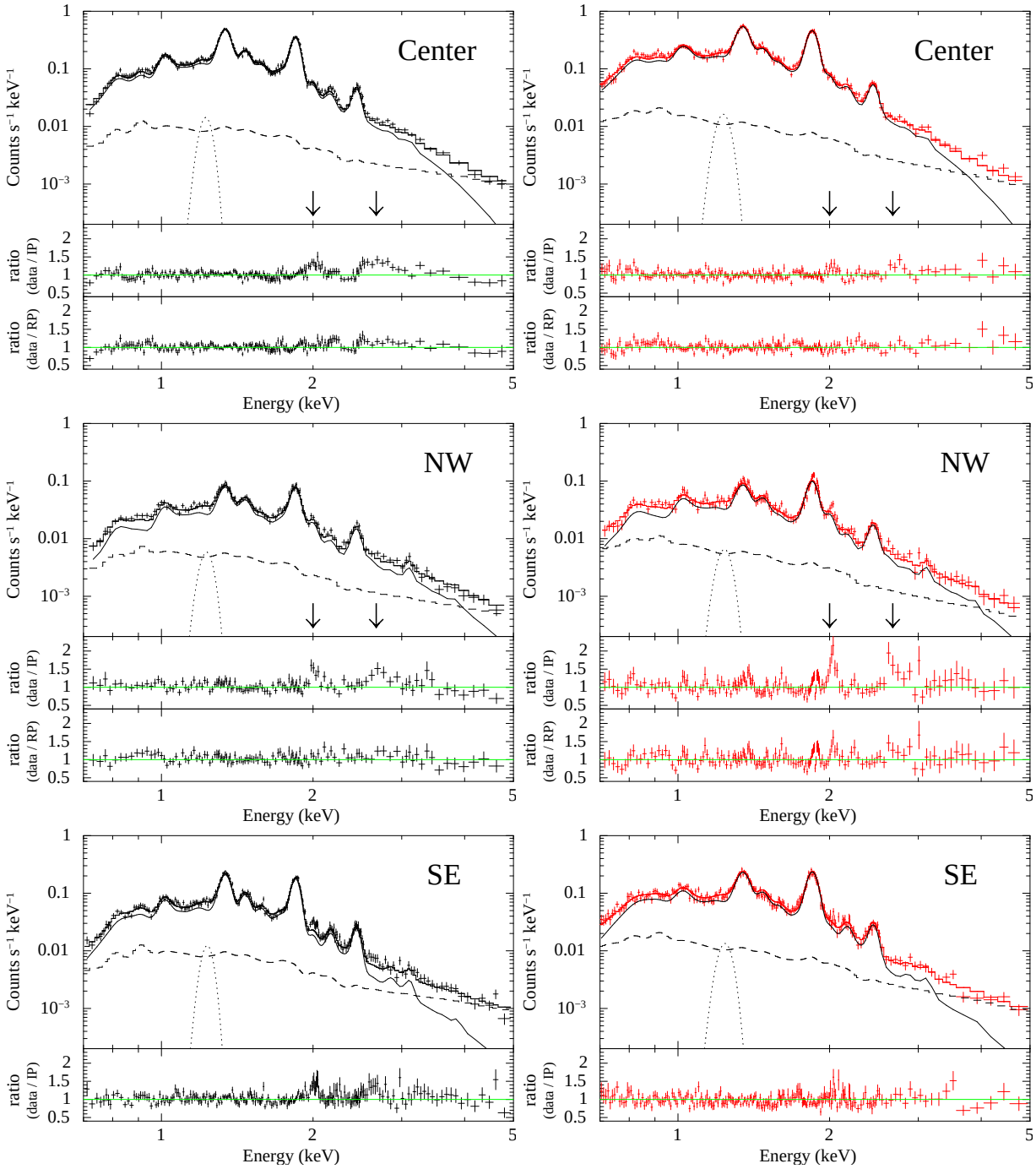

Figure 5.4: Spectra obtained from the Center, NW, SE, NE, and SW regions of G290.1−0.8 (black: FI, red: BI). Each spectrum is fitted with the plasma model (solid line) + the background model (dashed line) + one Gaussian (dotted line). For the plasma model, the RP is employed in the Center and the NW, while the IP is employed in the SE, NE, and SW. The bottom panels are the ratios of the data to the models we applied. For the Center and the NW, we show the ratios of the data to the IP models in the middle panels for comparison.

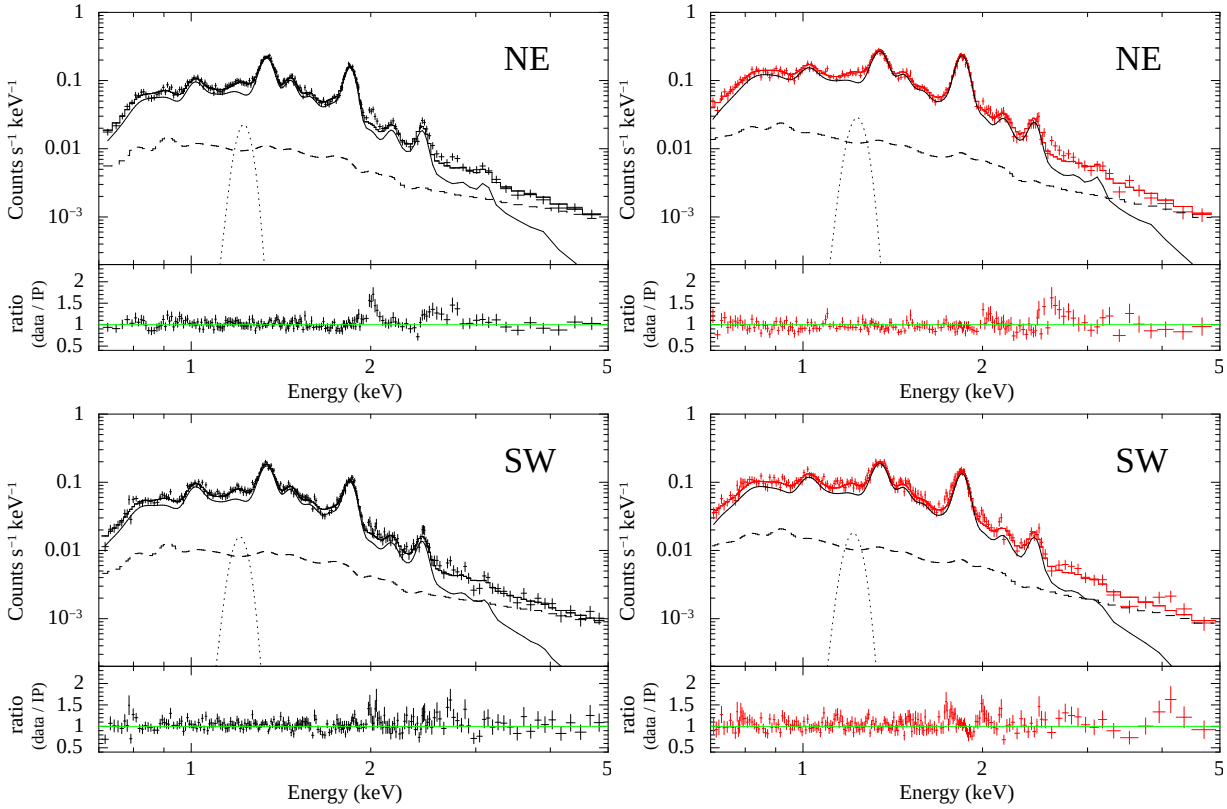

Figure 5.5: Continued.

Table 5.3: Best-fit parameters for G290.1−0.8 spectra.

Parameter	Center	NW	SE	NE	SW
	RP	RP	IP	IP	IP
$N_{\rm H}$ ($10^{21}{\rm cm}^{-2}$)	$7.8^{+0.3}_{-0.5}$	$9.6^{+0.8}_{-1.4}$	$6.8^{+0.7}_{-0.8}$	$6.7^{+0.5}_{-0.6}$	$6.2^{+0.7}_{-0.8}$
$kT_{\rm init}$ (keV)	$1.7^{+1.2}_{-0.3}$	> 1.9	–	–	–
$kT_{\rm e}$ (keV)	$0.45^{+0.02}_{-0.01}$	$0.52^{+0.02}_{-0.04}$	$0.66^{+0.03}_{-0.02}$	$0.64^{+0.02}_{-0.01}$	$0.59^{+0.03}_{-0.02}$
$n_{\rm e}t$ ($10^{12}{\rm s\,cm}^{-3}$)	$1.22^{+0.13}_{-0.09}$	$1.06^{+0.06}_{-0.20}$	$0.34^{+0.07}_{-0.06}$	$0.42^{+0.09}_{-0.07}$	$0.64^{+0.25}_{-0.18}$
VEM ($10^{11}{\rm cm}^{-5}$)	23^{+2}_{-1}	$4.0^{+0.7}_{-0.5}$	$4.9^{+0.4}_{-0.5}$	5.9 ± 0.4	$4.9^{+0.3}_{-0.5}$
Ne	$0.43^{+0.04}_{-0.06}$	0.7 ± 0.2	$0.36^{+0.08}_{-0.07}$	$0.43^{+0.09}_{-0.08}$	0.5 ± 0.1
Mg	1.5 ± 0.1	1.5 ± 0.3	1.3 ± 0.1	1.2 ± 0.1	1.2 ± 0.2
Si	$2.5^{+0.1}_{-0.2}$	$2.6^{+0.4}_{-0.3}$	$2.0^{+0.2}_{-0.1}$	1.6 ± 0.1	$1.4^{+0.2}_{-0.1}$
S	2.1 ± 0.2	$2.4^{+0.4}_{-0.3}$	$1.5^{+0.1}_{-0.2}$	1.1 ± 0.1	$1.1^{+0.1}_{-0.2}$
Ar (= Ca)	2 ± 1	3 ± 1	$1.1^{+0.7}_{-0.6}$	1.3 ± 0.6	< 1.6
Fe (=Ni)	$0.10^{+0.02}_{-0.03}$	$0.3^{+0.1}_{-0.2}$	$0.16^{+0.06}_{-0.05}$	0.22 ± 0.05	$0.18^{+0.07}_{-0.06}$
χ^2_ν (d.o.f.)	1.12 (1436)	1.10 (749)	1.08 (1126)	1.06 (1198)	1.10 (1080)

rapid cooling of the electron temperature. This RP model fit significantly improves the χ^2_ν value to 1.12 and 1.10 for the Center and the NW spectra, respectively. The hump-like residuals in the IP fits disappear in the RP fits (see the bottom panels of the Center and NW spectra in figure 5.4). On the other hand, the RP fits for the SE, NE and SW spectra do not significantly improve the χ^2_ν value from those of the IP fits. Although the hump-like residuals also seen in the NE, the current photon statistics does not allow us to discriminate the IP and RP models.

The best-fit spectra and parameters for the RP fits (Center and NW) and IP fits (SE, NE, and SW) are shown in the figure 5.4 and table 5.3. The null hypothesis probabilities of the IP fits are 8×10^{-7} (Center), 9×10^{-6} (NW), 0.03 (SE), 0.08 (NE), and 0.01 (SW), while those of the RP fits are 0.001 (Center), 0.03 (NW). Although all the spectra are statistically rejected under the canonical criterion of the null probability of 0.1, the IP fits for the SE, NE and SW and the RP fits for the Center and NW are marginally acceptable by taking account of possible systematic errors.

We select the similar regions to those employed in García et al. (2012). They reported that CIE models adequately describe some of the regions. We therefore try CIE models for the direct comparison between the Suzaku and the XMM-Newton results. The CIE results, however, show no significant difference from the IP fits within the systematical uncertainty; the χ^2_ν values of the CIE fits are 1.22 (Center), 1.24 (NW), 1.12 (SE), 1.09 (NE), and 1.11 (SW). We thus use the IP fit results for the SE, NE, and SW regions, while the RP results for the Center and NW regions in the following discussion as the good approximation.

5.4 Discussion

5.4.1 Discovery of RP

We find that the spectrum of G290.1−0.8 is well described by RPs in the Center and NW regions, while those in the SE, NE and SW regions are IPs. The electron temperatures are $0.45^{+0.02}_{-0.01}$ keV (Center), $0.52^{+0.02}_{-0.04}$ keV (NW), $0.66^{+0.03}_{-0.02}$ keV (SE), $0.64^{+0.02}_{-0.01}$ keV (NE), and $0.59^{+0.03}_{-0.02}$ keV (SW). Thus the temperatures of the RP regions (Center and NW) are lower than those of the IP regions (SE, NE, and SW) about 25 %. The ionization parameter ($n_{\rm e}t$) in the NW region is smaller than that in the Center region, which is consistent with the fact that the apparent RRC feature in the NW spectrum is clearer than that in the Center. In contrast, the XMM-Newton observations reported the plasma of IP or CIE in all the regions (García et al. 2012). We believe that the discrepancy is due to the better energy resolution and photon statistics in the hard energy band of *Suzaku* than those of *XMM-Newton*-Newton (as in the case of IC 443; Yamaguchi et al. 2009).

As we noted in the section 5.3.2.2, we allowed the possible fluctuation of the CXB in the source regions. We here examine the effect of the CXB fluctuation changing the flux by ±50 %, which is the largest deviation expected for each region, of the nominal value (Kushino et al. 2002). The results, however, show no significant change of the χ^2_ν and the best-fit parameters; for example the electron temperatures change only by 0.01 keV, which is within the range of the statistical errors.

5.4.2 Abundances and Masses

The abundances of the RP are over-solar, while those of the IP except in the SE region are roughly 1 solar. The abundances in the SE region seem intermediate between those in the RP and IP regions. Probably, the plasma in the SE region is a mixture of the RP and the IP. In fact, although the significance level is low, the RP fit for the SE (χ^2/d.o.f. = 1210/1125) is slightly better than the pure IP fit (χ^2/d.o.f. = 1215/1126).

The abundance pattern of the RP in NW is shown in figure 5.6 together with the prediction from the massive progenitor (Woosley & Weaver 1995). The pattern is roughly similar to that of ejecta from the progenitor star of M = 20–25 $M_\odot$. On the other hand, the solar abundances of the IP in the NE and SW regions suggest that the plasma is ISM origin.

In detail, the Ne and Fe abundances in every region are systematically lower than the other elements. The Fe abundances are mainly determined by the line fluxes of Fe-L lines, which have rather large uncertainty in the present plasma code. The main transitions are

3s→2p (~ 0.7 keV) and 3d→2p (~ 0.8 keV) of Fe XVII. These low energy line fluxes are significantly affected by the low energy absorptions and contamination from the Lyβ of O VIII (0.77 keV). As the results, the Fe abundance may have a large error, and hence apparent depletion of Fe may occur. The Ne abundances are due to Kα lines of Ne IX and Ne X. The L-line energies from more highly ionized Fe XIX come near the Kα of Ne IX (e.g., see Brinkman et al. (2000)). Therefore, coupled to the large error of Fe abundance, the Ne abundance would have a large error too. However, the reason of apparent Ne depletion is somehow puzzling. We simply note that the same depletions of Ne and Fe are observed in García et al. (2012), and also reported from other SNRs (e.g., W28, Sawada & Koyama 2012).

Assuming the depth of the SNR as 11 pc, which is same as the diameter of the Center region, the plasma mass is calculated to be $22\,f^{0.5}\,M_\odot$ (Center), $8\,f^{0.5}\,M_\odot$ (NW), $22\,f^{0.5}\,M_\odot$ (SE), $13\,f^{0.5}\,M_\odot$ (NE), and $11\,f^{0.5}\,M_\odot$ (SW), respectively. Therefore, the masses of the ejecta and the ISM are roughly estimated to be $30\,f^{0.5}\,M_\odot$ (Center + NW) and $24\,f^{0.5}\,M_\odot$ (NE + SW), respectively, if we ignore the SE where the ejecta and ISM are coexisting. Taking account of the uncertainty of the filling factor, the ejecta mass is not in contradiction with the progenitor mass ($M = 20$–$25\,M_\odot$) estimated by the abundances.

5.4.3 Origin of the RP

To form the RP in the Center and the NW regions, either a rapid electron cooling or an enhancement of ionization should occur. In the former case, the electron temperature is expected to be lower in the RP region, while visa versa for the latter case. Since our results show a lower temperature of the RP than that of the IP, the former scenario is preferable; the electron cooling occurred to the center-northwest direction.

For the electron cooling, two formation processes are proposed: thermal conduction (Kawasaki et al. 2002) and adiabatic rarefaction (Itoh & Masai 1989; Yamaguchi et al. 2009). The RP should become prominent toward the contact region with cold dense clouds in the former case, while vice-versa in the latter case. Filipovic et al. (2005) reported that a dense molecular cloud may be interacting with the SNR shock at the southwest. Recently, Auchettl et al. (2015) also discovered the GeV emission at the west by *F*ermi. These results may suggest that plausible origin of the RP is the thermal conduction, although the interacting region with molecular clouds are a little off-set from the RP region (Center-NW).

5.4.4 Association with IGR J11-14-6103

Assuming the distance of 7 kpc and using the best-fit $n_{\rm e}t$ and VEM in the NW region, the recombining time ($t_{\rm rec}$) is estimated to be $50\,(f/0.25)^{0.5}$ kyr. While this value is larger than the estimated SNR age of 10–20 kyr (Slane et al. (2002)), This disagreement is probably due to the simplified age estimation of the complex SNR. In fact, Halpern et al. (2014) reported the spin-down age of the pulsar to be 116 kyr, which favors our recombining time. If the SNR age is equal to the recombining time of $50\,(f/0.25)^{0.5}$ kyr, the kick velocity of the pulsar is $400\,(f/0.25)^{-0.5}\,{\rm km\,s^{-1}}$. This is consistent with the mean value of pulsars of $450 \pm 90\,{\rm kms^{-1}}$ (Lyne & Lorimer 1994), and contradicts the high kick velocity of 1000–2000 $\rm kms^{-1}$, estimated by Pavan et al. (2014).

Since the long-jet of IGR J11014-6103 is pointing to the northwest, the same direction of the RP region, it may be conceivable that the RP was made by the jet when the pulsar was still in the main body of the SNR. However, this scenario would be a remote possibility because the jet energy is far less to make a significant over-ionization at the NW plasma, unless it was extraordinary bright, like a gamma-ray burst and its afterglow.

5.5 Summary

We have analyzed Suzaku/XIS data obtained from G290.1−0.8. The results are summarized as follows:

1. The plasma states in G290.1−0.8 are different from region to region. We find Si Lyα and RRCs from the NW and the Center sepctra, while not from other regions. Thus the plasmas are in the recombining phase at the Center and the NW, while in the ionizing phase at other regions.

2. The electron temperature of the RP is lower than that of the IP.

3. The abundance pattern indicates that the RP is dominated by ejecta of a core-collapse SN, while the IP is likely ISM origin.

4. A plausible origin of the RP is the thermal conduction by molecular clouds.

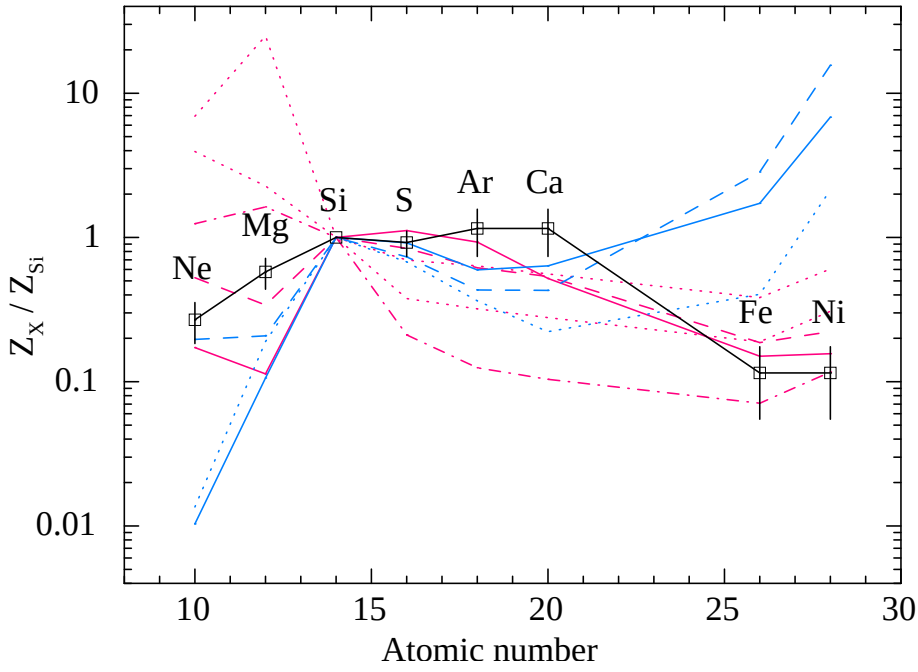

Figure 5.6: Abundance pattern of the NW plasm in G290.1−0.8 (black solid line). Each elemental abundance is normalized by the value of Si. The red, green, blue, light blue, and magenta dashed lines represent core-collapse models with main sequence masses of 20, 25, 30, 35, and 40 $M_\odot$, respectively (Woosley & Weaver 1995)

Chapter 6

G272.2−3.2

6.1 Previous Results

G272.2−3.2 is one of thermal dominated SNRs in X-rays. It was firstly discovered with the ROSAT all sky survey (Greiner & Egger 1993; Greiner et al. 1994). The ROSAT observations revealed the spherical structure of 7.′6 radius, showing center-filled thermal X-rays. Greiner et al. (1994) argued that the origin of the center X-ray emission is reverse-shocked ejecta from the SN explosion or cloud evaporation in the interior of the remnant.

More recently, Harrus et al. (2001) found a non-equilibrium ionization (NEI) plasma of $kT_{\rm e} \sim 0.7\,{\rm keV}$ with the ASCA and the ROSAT data. The statistical analysis of the Galactic SNRs distribution led to a probable distance of 2 kpc. However, a large upper limit of 10 kpc was also reported using the interstellar absorption. Lopez et al. (2011) suggested a Type Ia origin for G272.2−3.2 with a morphological analysis of the Chandra data. In the Suzaku data, Sezer & Gök (2012) found an NEI plasma of super-solar abundances and a stratified structure. They claimed that the plasma originated from the ejecta of a Type Ia SN based on the abundance pattern. McEntaffer et al. (2013), using the Chandra data, confirmed the NEI plasma of $kT_{\rm e} = 0.7$–$1.5\,{\rm keV}$. They also found a cool collisional ionization equilibrium (CIE) plasma of $kT_{\rm e} \sim 0.2\,{\rm keV}$ in the outer regions. Since the abundances of the NEI plasma were depleted in the outer region, they claimed that the plasma in the center region was ejecta origin, while the outer region was the shock-heated ISM. Sánchez-Ayaso et al. (2013), using the XMM-Newton and the Chandra data, reported the two NEI plasmas similar to those by McEntaffer et al. (2013), but the temperature distribution was different; the temperatures in the center and outer plasmas were $0.76 \pm 0.03\,{\rm keV}$ and $1.05 \pm 0.79\,{\rm keV}$, respectively.

Based on the super solar abundances and abundance pattern of Si, S, and Fe, the

authors in the previous studies proposed a Type Ia origin for G272.2−3.2 (table 1 of Sezer & Gök (2012), table 5 of McEntaffer et al. (2013), and table 2 of Sánchez-Ayaso et al. (2013)). It is consistent with the fact that a pulsar or a pulsar wind nebula associated with the remnant was not found neither in the X-ray (McEntaffer et al. (2013)) nor the radio band (Duncan et al. (1997)). However, most of the spectral analyses in the previous studies were limited below 3 keV, and hence reliable K-shell line fluxes (or abundances) were available only for Ne, Mg, Si and S. Especially, the previous report by Sezer & Gök (2012) was poor in the data-reduction and analysis. They subtracted the background data from a very small region near the edge of the detector/mirror field, and hence degraded the S/N of the Suzaku spectra, especially above 3 keV.

6.2 Observation and Data Reduction

The Suzaku satellite observed G272.-2−3.2 with the XIS on 2011 May 28 and 2011 Nov 12. The observation log is given in table 6.1. Three of the XISs (XIS 0, 1 ,3) were operated in the normal full-clocking mode with a SCI technique. The amount of the injection charge was 2 keV for the FI CCDs (XIS 0, 3) on both observations, while for the BI CCD (XIS 3) it was 2 keV on the first observation and 6 keV on the second observation. The XIS data were reprocessed with the calibration data base (CALDB) released in 2014 February. We used the HEASOFT version 6.16 for the data reduction and XSPEC version 12.8.2 for the spectral analysis. The total exposure times of the first and the second observations, after the standard screening, are about 130 ks and 26 ks, respectively.

Table 6.1: Observation logs of G272.2−3.2.

Target	Obs. ID	Obs. Date	R.A.	Dec.	Exposure
			(J2000.0)		(ks)
G272.2−3.2	506060010	2011-May-28	$9^h6^m50.7^s$	$-52\,°7\,'23.2\,''$	130.1
G272.2−3.2	506060020	2011-Nov-12	$9^h6^m49.6^s$	$-52\,°7\,'20.3\,''$	25.5

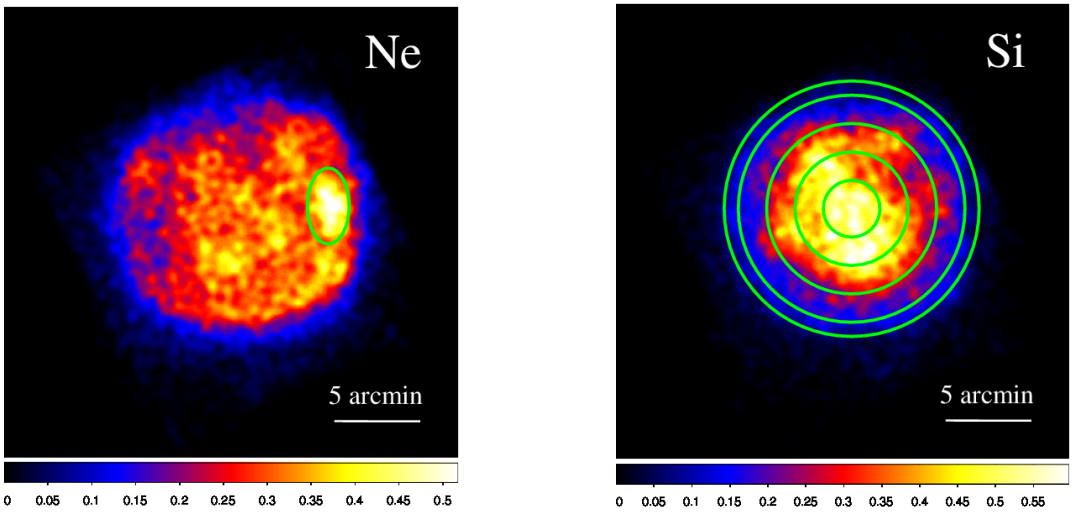

Figure 6.1: XIS images of G272.2−3.2 in the 0.86–0.96 keV band (Ne-band: left) and 1.79–1.93 keV band (Si-band: right). The spectral extraction regions are shown with the green lines.

6.3 Analyses and Results

6.3.1 Imaging Analysis

Figure 6.1 shows the narrow band images of the G272.2−3.2 in the energy bands of 0.86–0.96 keV and 1.79–1.93 keV, which include the K-shell lines of Ne and Si, respectively. We combine all the XIS data of the two observations to maximize the photon statistics. The images are binned with $2.''1 \times 2.''1$ and smoothed with a Gaussian kernel of $\sigma = 0.'45$.

The emission of the Ne K-shell band extends over the whole region of the SNR, while that of Si is concentrated at the center. In the Ne-band image, a hot spot shown in a green ellipse is also found in the west, which is reported in the previous study (Harrus et al. 2001; McEntaffer et al. 2013; Sánchez-Ayaso et al. 2013). The narrow band image of Mg K-shell (1.28–1.42 keV) has a similar profile to that of the Ne K-shell band, and those of S K-shell (2.41–2.51 keV) and Fe L-shell (1.18–1.28 keV) are similar to that of the Si K-shell band.

6.3.2 Spectral Analysis

Background Estimation

Since G272.2−3.2 extends widely over the XIS field of view ($17.'8 \times 17.'8$), the available background region is limited in the region of $r > 510''$ from the SNR center (here, BG region). Moreover, the BG region is contaminated by a leakage of the SNR emission due to the point spread function of the XRT with a relatively large half power diameter of $\sim 2'$. To estimate the leaked SNR emission, we make spectra from the outer SNR region (r =300-450″) and the BG region. The NXBs are subtracted from the spectra of the two regions. The NXB-subtracted spectra consist of the SNR emission and the X-ray background (XBG). The SNR emission is modeled by a bremsstrahlung continuum plus several Gaussian lines. The XBG consists of the cosmic X-ray background (CXB) and the Galactic halo (GH) (e.g., Kushino et al. 2002; Henley & Shelton 2013), which are represented by a power-law and a CIE (APEC in the XSPEC), respectively. With these settings, we fit the two spectra simultaneously using the simulated ARFs for the two regions. The flux of the CXB is a free parameter within the range of the possible fluctuation ($\sim 40\,\%$) (Kushino et al. 2002). The fit is reasonable with χ^2_ν (d.o.f.) = 1.19 (360). The best-fit spectrum and parameters for the BG are summarized in figure 6.2 and table 6.2, respectively. We employ the XBG spectrum in the following SNR analysis.

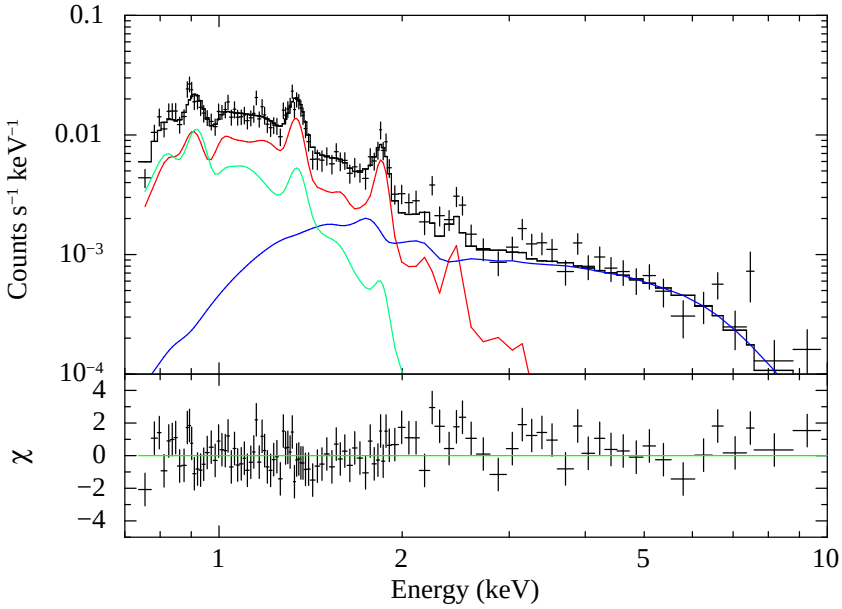

Figure 6.2: Background region spectrum (FI) of G272.2−3.2. The spectrum is fitted with the model of the CXB (blue), GH (green), and stray light from the source (red).

Table 6.2: Best-fit parameters for the background spectrum of G272.2−3.2.

Component	Parameter	Value
Abs1	$N_{\rm H}$ (10^{21}cm^{-2})	8.6 (fixed)
CXB	Photon index	1.4 (fixed)
	Flux†	2.44 ± 0.09
Abs2	$N_{\rm H}$ (10^{21}cm^{-2})	8.0 ± 0.5
GH‡	$kT_{\rm e}$ (keV)	0.20 ± 0.02
χ^2_ν (d.o.f.)		1.19 (360)

† Flux (10^{-11} erg cm^{-2} s^{-1} deg^{-2}) in the $2-10$ keV band.
‡ Abundances are fixed to the solar values.

Analysis of Whole Region Spectrum

We first produce a spectrum from the whole region of the SNR (the circle of r =450″), and subtract the NXB. The NXB-subtracted spectrum is shown in figure 6.3. Many K-shell lines from highly ionized Ne, Mg, Si, S, Ar, and Ca are found. The Ar and Ca lines are the first discovery from this SNR. In addition, we find a line near at 6.4 keV. With a Gaussian line fit, the center energy and flux are determined to be $6.42^{+0.07}_{-0.05}$ keV and $(1.83 \pm 0.50) \times 10^{-6}$ photons s^{-1} cm^{-2}, respectively. The center energy constrains the charge state of Fe to be $\leq 18+$ (Beiersdorfer et al. 1993). This line is not a contamination of the Fe K-shell line in the Galactic ridge X-ray emission (GRXE), because the GRXE has the emission line at about 6.7 keV, and the flux of the GRXE near G272.2−3.2 should be very faint due to the large distance from the Galactic ridge (e.g., Uchiyama et al. 2013).

We fit the whole region spectrum with an NEI plasma model (VNEI) adding the XBG model given in table 1. In the VNEI fit, the electron temperature $kT_{\rm e}$, column density $N_{\rm H}$ and ionization timescale $n_{\rm e}t$ are free parameters, where $n_{\rm e}$ and t represent the electron density and the time after the shock heating, respectively. The abundances of Ne, Mg, Si, S, Ar, and Fe are also free parameters, while those of Ca and Ni are tied to those of Ar and Fe, respectively. This fit, however, leaves a line-like residual around 1.2 keV that comes from the uncertainty of the Fe L-shell data in the VNEI code (e.g., Borkowski et al. 2006; Yamaguchi et al. 2011). Thus we add a Gaussian line at 1.2 keV. The χ^2_ν (d.o.f.) is largely improved from 1.89 (2006) to 1.38 (2004), but residuals below 1 keV are still large (panel:(a) in figure 6.3). Therefore, we add a CIE model (APEC), where we leave the abundances free. Although this fit largely improved the χ^2_ν (d.o.f.) from 1.38 (2004) to 1.21 (2001), this model fit is statistically rejected.

Significant residuals are found at 6.4 keV and around 2–3 keV (panel:(b)). The former is due to the K-shell line of nearly neutral Fe, and the latter is due to K-shell complexes of Si and S. Thus, for further improved fit, we divide the VNEI spectrum into four components, they stand for H–Mg (VNEI 1), Si–S (VNEI 2), Ar–Ca (VNEI 3), and Fe–Ni (VNEI 4). We let the temperatures for those four components be independent free parameters. We link the ionization parameters ($n_{\rm e}t$) for the first three components, but fix to 10^{10}cm^{-3} s for the Fe–Ni plasma because of the low ionization. As a result, χ^2_ν (d.o.f.) is improved to be 1.16 (1998) (panel:(c)). The improvement is significant with the F-test null probability much less than 0.01 %. In the χ^2 test, this model is still unacceptable, possibly due to systematic errors. In fact, we obtain no significant improvement by adding further components or by changing the trial model. We thus adopt this model as the best approximation. The best-fit parameters are given in table 6.3.

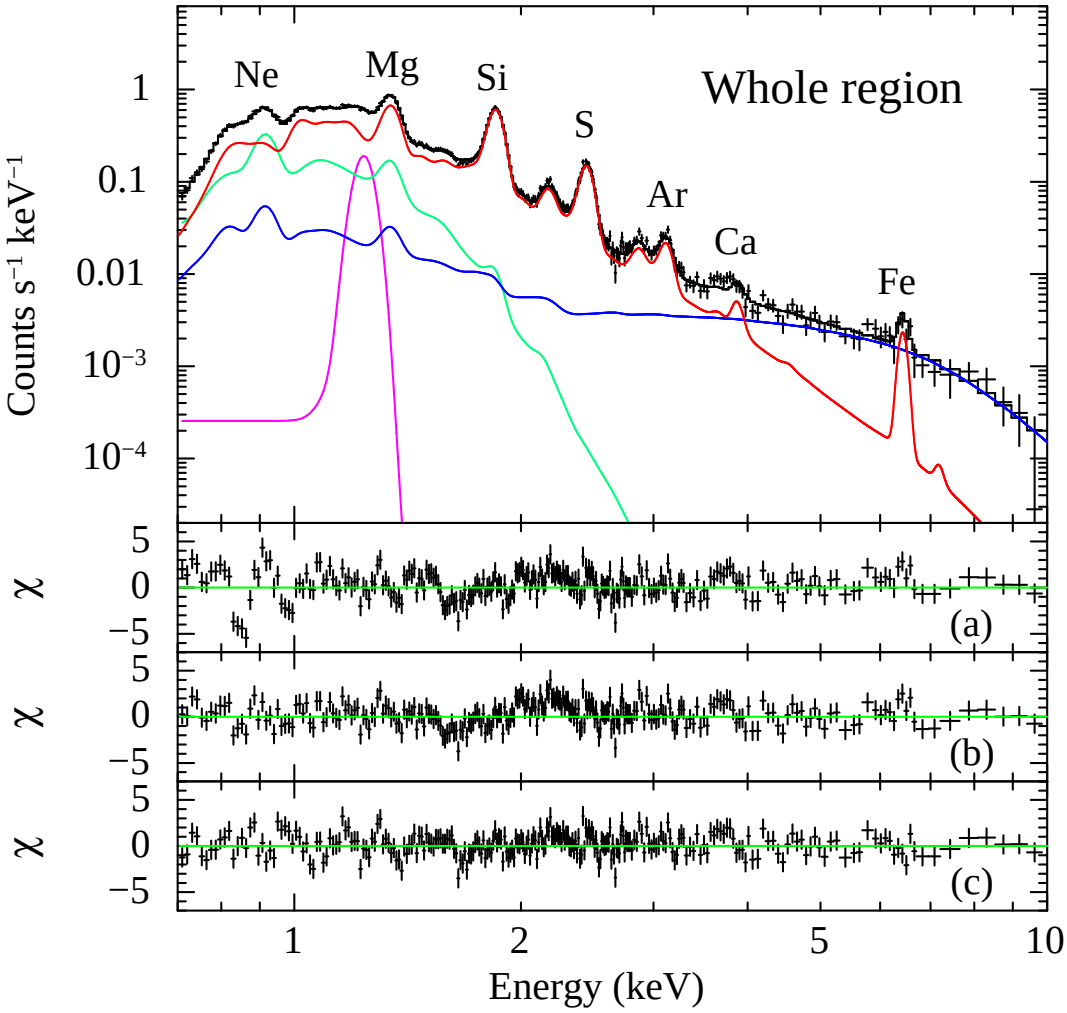

Figure 6.3: Whole region spectrum (FI) of G272.2−3.2. The spectrum is fitted with the model of 4-VNEI (red) + 1-APEC (green), adding the XBG (blue) and a Gaussian line (magenta). The lower panels represent the residuals from the source models of (a) 1-VNEI, (b) 1-VNEI + 1-APEC, and (c) 4-VNEI + 1-APEC, respectively.

Analysis fo Spatially Resolved Spectra

We next make spatially-resolved spectra dividing the SNR into a circle and four rings with the boundary radii of $r = 0-100''$, $100-200''$, $200-300''$, $300-400''$ and $400-450''$ (figure 6.1 right). We also define the region for the hot spot at the western edge of the remnant (figure 6.1 left). The spectra extracted after the NXB subtraction are shown in figure 6.4. We fit these spectra with the same model and method as those for the whole region, but fixing the column density, temperatures, and ionization parameters to the best-fit values of the whole region. We also fix the abundance of the APEC to 1 solar because of the large statistical error. The best-fit parameters are given in table 6.3.

We show the radial profile of the surface brightness of the APEC and the VNEI 1–4 (H–Mg, Si–Ca, Fe–Ni) in figure 6.5. The data from the hot spot are also added in diamonds, while the data from the $400-450''$ ring are not plotted, because this region is just at the boundary of the SNR. The components show different spatial structures with each other; the surface brightness of the APEC and light elements (H–Mg) in the VNEI increase to the outer region, while those of the intermediate (Si–Ca) and Fe-peaked elements (Fe–Ni) in the VNEI concentrate at the inner region. The hot spot shows clear enhancement in the APEC and light elements in the VNEI, while it shows no clear enhancement in the intermediate and Fe-peaked elements in the VNEI.

Figure 6.6 shows the radial distribution of the abundances of Ne, Mg, Si–S and Fe in the VNEI. The abundance of Ne is constant across the radius, while those of Si–S and Fe show central concentrations. The abundance of Mg is in between that of Ne and those of Si–S. The abundances at the hot spot show no deviation from the radial profile.

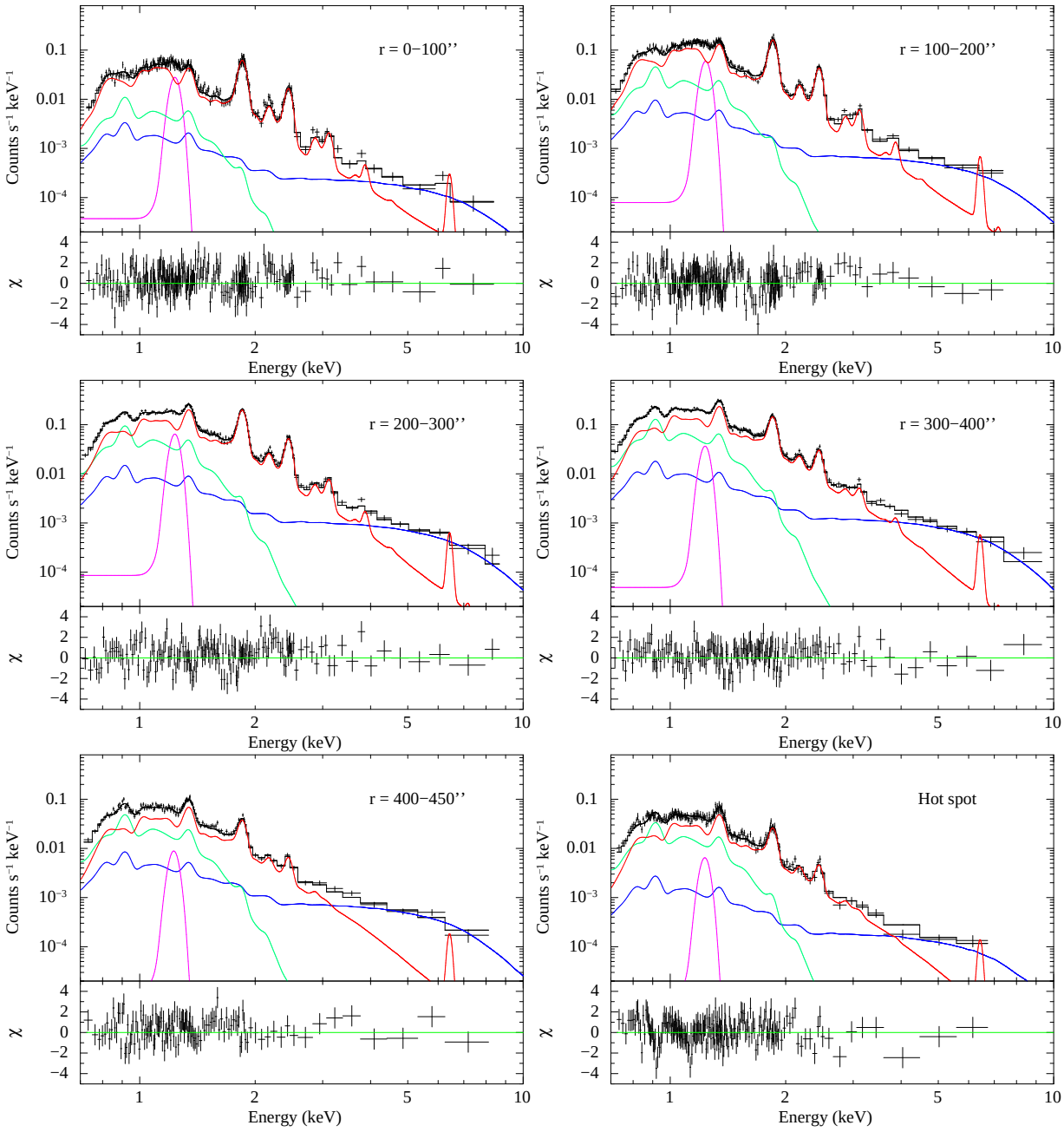

Figure 6.4: Spectra (FI) obtained from six regions of G272.2−3.2: $r = 0-100''$, $100-200''$, $200-300''$, $300-400''$, $400-450''$, and hot spot. The same model as in the figure 6.3 is applied. Each lower panel shows the residual of the data from the model.

Table 6.3: Best-fit parameters for the SNR spectra of G272.2−3.2.

Component	Parameter	Whole	0–100″	100–200″	200–300″	300–400″	400–450″	Hot-spot
Absorption	$N_{\rm H}$ $(10^{22}{\rm cm}^{-2})_{\rm FI}$	0.99 ± 0.01				0.99 (fixed)		
	$N_{\rm H}$ $(10^{22}{\rm cm}^{-2})_{\rm BI}$	0.98 ± 0.01				0.98 (fixed)		
VNEI 1	$kT_{\rm e}$ (keV)	0.62 ± 0.02				0.62 (fixed)		
	H	1 (fixed)				1 (fixed)		
	He	1 (fixed)				1 (fixed)		
	C	1 (fixed)				1 (fixed)		
	O	1 (fixed)				1 (fixed)		
	Ne	0.54 ± 0.03	0.63 ± 0.11	0.61 ± 0.06	0.60 ± 0.04	0.59 ± 0.03	0.47 ± 0.05	0.62 ± 0.08
	Mg	0.74 ± 0.03	1.09 ± 0.12	1.06 ± 0.06	0.86 ± 0.04	0.75 ± 0.03	0.67 ± 0.05	0.83 ± 0.07
	$n_{\rm e}t$ $(10^{10}{\rm cm}^{-3}\,{\rm s})$	12.3 ± 1.0				12.3 (fixed)		
	$EM^{\dagger}$ $(10^{11}{\rm cm}^{-5})$	30.1 ± 2.5	1.28 ± 0.10	4.12 ± 0.18	8.23 ± 0.24	11.1 ± 0.3	2.75 ± 0.11	2.12 ± 0.11
VNEI 2	$kT_{\rm e}$ (keV)	0.80 ± 0.03				0.80 (fixed)		
	Si	0.97 ± 0.06	2.44 ± 0.22	1.94 ± 0.10	1.23 ± 0.04	0.63 ± 0.02	0.50 ± 0.03	0.60 ± 0.05
	S	1.25 ± 0.08	3.34 ± 0.33	2.69 ± 0.15	1.70 ± 0.07	0.66 ± 0.03	0.40 ± 0.05	0.50 ± 0.07
	$n_{\rm e}t$ $(10^{10}{\rm cm}^{-3}\,{\rm s})$					(Linked to VNEI 1)		
	$EM^{\dagger}$ $(10^{11}{\rm cm}^{-5})$					(Linked to VNEI 1)		
VNEI 3	$kT_{\rm e}$ (keV)	1.00 ± 0.22				1.00 (fixed)		
	Ar = Ca	0.68 ± 0.22	1.73 ± 0.34	1.58 ± 0.17	1.02 ± 0.10	0.38 ± 0.07	< 0.13	< 0.18
	$n_{\rm e}t$ $(10^{10}{\rm cm}^{-3}\,{\rm s})$					(Linked to VNEI 1)		
	$EM^{\dagger}$ $(10^{11}{\rm cm}^{-5})$					(Linked to VNEI 1)		
VNEI 4	$kT_{\rm e}$ (keV)	2.76 ± 0.15				2.76 (fixed)		
	Fe = Ni	0.30 ± 0.02	0.86 ± 0.08	0.60 ± 0.03	0.30 ± 0.01	0.21 ± 0.01	0.22 ± 0.02	0.28 ± 0.03
	$n_{\rm e}t$ $(10^{10}{\rm cm}^{-3}\,{\rm s})$	1 (fixed)				1 (fixed)		
	$EM^{\dagger}$ $(10^{11}{\rm cm}^{-5})$					(Linked to VNEI 1)		
APEC	$kT_{\rm e}$ (keV)	0.172 ± 0.005				0.172 (fixed)		
	All elements	< 2.4				1 (fixed)		
	$EM^{\dagger}$ $(10^{11}{\rm cm}^{-5})$	342 ± 33	11.4 ± 1.7	46.9 ± 2.8	101.3 ± 3.6	137.0 ± 4.0	39.1 ± 1.8	36.1 ± 2.0
χ^2_ν (d.o.f.)		1.16 (1998)	1.09 (712)	1.15 (1186)	1.14 (1392)	1.04 (1366)	1.03 (870)	1.13 (620)

† Emission measure defined as $\int n_e n_{\rm H} dV/(4\pi d^2)$, where V and d are the emitting volume ($\rm cm^3$) and the distance to the source (cm), respectively.

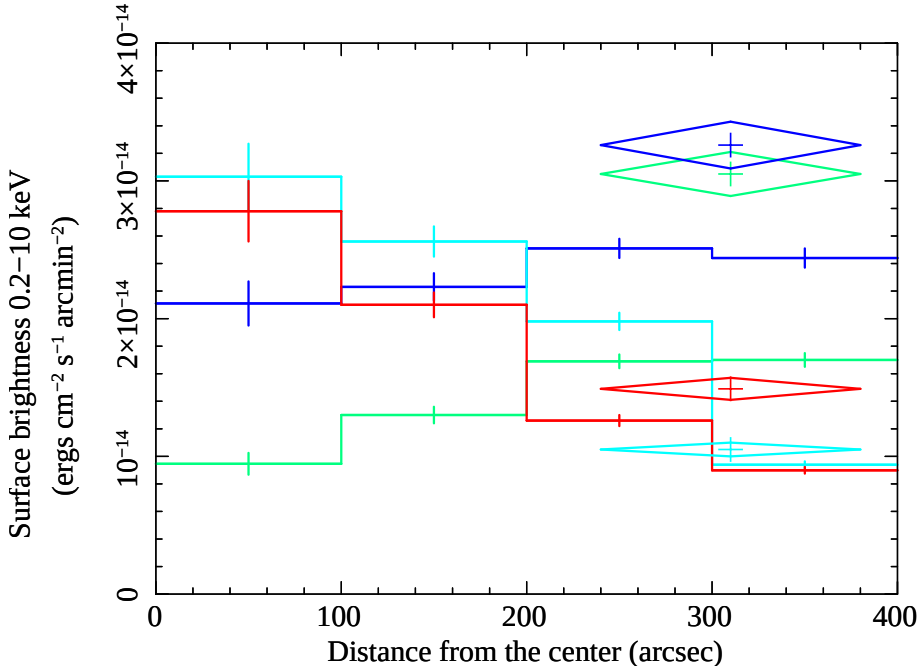

Figure 6.5: Radial profiles of the surface brightness of the plasma components in G272.2−3.2: ISM (green), H–Mg ejecta (blue), Si–Ca ejecta (light blue), and Fe–Ni ejecta (red). The results of the hot spot are added in diamonds.

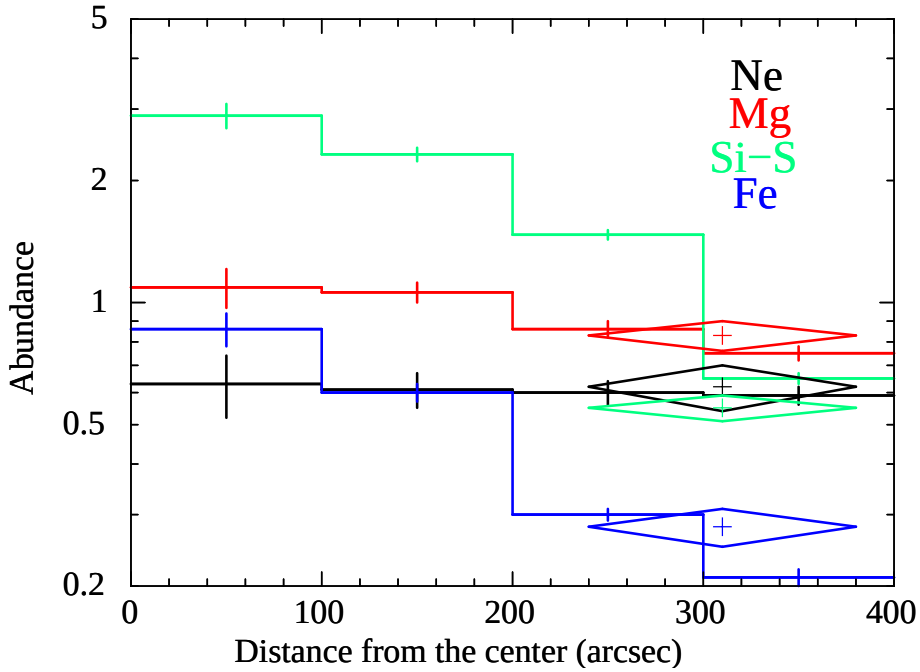

Figure 6.6: Radial distribution of the ejecta abundances of G272.2−3.2. The abundances are taken from VNEI 1-4 plasma. The results of the hot spot are shown in diamonds.

6.4 Discussion

We find two important facts on the Galactic SNR G272.2−3.2 by the revised data reduction and background subtraction for the Suzaku data. (1) A clear emission above 3 keV is detected, and the K-shell lines of Ar, Ca, and Fe are discovered for the first time. (2) The G272.2−3.2 plasma consists of two components: a low-temperature CIE plasma ($kT_{\rm e} \sim 0.2$ keV) and a high-temperature NEI plasma ($kT_{\rm e} = 0.6$–3 keV). Since the CIE plasma (APEC) has roughly solar abundances over the entire area (table 6.3), this likely originates from the ISM. The abundances of the NEI plasma (VNEI) increase toward the center and becomes higher than solar values. Therefore it must be ejecta origin. The newly detected K-shell lines of Ar, Ca, and Fe mainly come from the ejecta. In the following subsections, we separately discuss the ISM and the ejecta based on the revised results of the distance, mass and morphology.

6.4.1 Distance Estimation

The distance to G272.2−3.2 from the Sun has been estimated as 2-10 kpc using the statistical analysis (lower limit) and the interstellar absorption (upper limit) (Harrus et al. 2001). The best-fit $N_{\rm H}$ of 1.0×10^{22} cm^{-2} is consistent with Harrus et al. (2001), and hence the same method and estimation of the distance (10 kpc) may be applied. However, the observed $N_{\rm H}$ of G272.2−3.2 is larger than those of the sources on the plane in $l = 260$–290° that are summarized in table 6.4, in spite of its large Galactic latitude. In fact, Pup A (G260.4−3.4), at similar Galactic latitude to G272.2−3.2, has a small value of $N_{\rm H}$ ($< 10^{22}$ cm^{-2}). The large value of $N_{\rm H}$ of G272.2−3.2 would be due to a local absorption in the line of sight at the "Vela region" (Lallement et al. 2014). On the other hand, more than 90 % of the Galactic SNRs are statistically distributed within 100 pc from the Galactic plane (Ilovaisky & Lequeux 1972). The large Galactic latitude limits the distance of G272.2−3.2 to be < 2 kpc same as that in the statistical analysis by Harrus et al. (2001). Additionally, all the sources in table 6.4 may locate on the Carina nebula arm, like pulsars (in figure 1 of Taylor & Cordes 1993). G272.2−3.2 may also locate on the edge of this arm, at the tangential point of the arm with the distance of ∼2–3 kpc. Thus we assume that the most likely distance, d, is 2–3 kpc. Hereafter we adopt the distance of 2.5 kpc, or parameterized as $d_{2.5} = d/2.5$ kpc.

Table 6.4: Column densities of the sources on the plane of $l = 260 - 290°$.

Name	(l, b)	d (kpc)	$N_{\rm H}$ (10^{21} cm^{-2})	Refs.*
Puppis A	(260.°4, −3.°4)	2.2	2 – 4	1, 2, 3, 4
Vela SNR	(263.°9, −3.°3)	0.25 – 0.3	0.2 – 0.4	5, 6
Vela Jr	(266.°2, −1.°2)	0.5 – 1	3 – 6	7, 8, 9, 10
G272.2−3.2	(272.°2, −3.°2)	2 – 10	9 – 11	11, 12, 13, 14
PSR J1016-5857	(284.°0, −1.°8)	3	12	15, 16
MSH 10-53	(284.°3, −1.°8)	2.9	8	17, 18
XMMUJ101855.4 -58564	(284.°3, −1.°8)	5.4	6.6	18
B1046−58	(287.°4, +0.°6)	3	4 – 9	16, 19, 20
MSH 11-61A	(290.°1, −0.°8)	7	5 – 9	21, 22, 23
MSH 11-62	(291.°0, −0.°1)	1 – 11	6 – 6.7	24, 25
MSH 11-54	(292.°0, +1.°8)	6	4 – 6	26, 27, 28, 29

* References: (1) Reynoso et al. (2003); (2) Hwang et al. (2008);
(3) Katsuda et al. (2008a); (4) Katsuda et al. (2010); (5) Lu & Aschenbach (2000);
(6) Dodson et al. (2003); (7) Katsuda et al. (2008b) (8) Pannuti et al. (2010);
(9) Kishishita et al. (2013); (10) Allen et al. (2015); (11) Greiner et al. (1994);
(12) Harrus et al. (2001); (13) Sánchez-Ayaso et al. (2013);
(14) McEntaffer et al. (2013); (15) Camilo et al. (2004);
(16) Kargaltsev & Pavlov (2008); (17) Ruiz & May (1986);
(18) H. E. S. S. Collaboration et al. (2012); (19) Cordes & Lazio (2002);
(20) Gonzalez et al. (2006); (21) Filipovic et al. (2005); (22) García et al. (2012);
(23) Kamitsukasa et al. (2015b); (24) Harrus et al. (1998); (25) Slane et al. (2012);
(26) Gaensler & Wallace (2003); (27) Park et al. (2004); (28) Lee et al. (2010)
(29) Kamitsukasa et al. (2014);

6.4.2 ISM Structure and Density

The surface brightness of the ISM shows an increase toward the outer rings. From the angular size, the radius of G272.2−3.2 is 1.7×10^{19} cm and volume of the plasma is 2×10^{58} cm^3. The best-fit ISM temperature of $kT_{\rm e} = 0.17$ keV gives the expansion speed of $V_s = 3.8 \times 10^2$ km s^{-1} from the strong shock relation assuming electron-ion temperature equilibration, $kT_{\rm e} = 3/16 \mu m_{\rm H} V_s^2$, where μ and $m_{\rm H}$ are the mean atomic mass and the mass of a hydrogen atom, respectively. Consequently, the dynamical age is $\sim 6 \times 10^3$ years from the Sedov self-similar solution (Sedov 1959). We calculate the density of the pre-heated ISM to be 1.0 cm^{-3} from the emission measure. This high ambient density and the large latitude of $-3.2°$ imply that G272.2−3.2 is located in the Carina nebula arm, consistent with the small distance of 2.5 kpc estimated in section 6.4.1.

6.4.3 Fe K-shell Line

The most important result of this work is the discovery of the Fe K-shell line. The Fe K-shell line energy is $6.42^{+0.07}_{-0.05}$ keV, and hence Fe is in a low-ionization state. The best-fit temperature ($kT_{\rm e}$) is 2.76 ± 0.15 keV with a small ionization parameter ($n_{\rm e}t$) of $10^{10}\,{\rm cm^{-3}\,s}$. Therefore the Fe ejecta should be recently heated by the reverse shock. Recently, Yamaguchi et al. (2014) suggested the new observational diagnostic to discriminate the progenitor types of SNRs using the Fe K-shell lines. They argued that the Fe K-shell lines of CC SNRs have higher center energies (6.6–6.7 keV) than those of Type Ia SNRs (6.4–6.5 keV). According to their criterion, G272.2−3.2 is a member of Type Ia SNRs.

6.4.4 Radial Profile of the Ejecta

The radial distribution of the surface brightness of Si–Ca and Fe in the ejecta increases toward the center. The abundances of the ejecta also have a layer-like structure (figure 6.6); the radial pattern of Ne is rather flat compared to the central concentration of Si–S and Fe. The best-fit temperatures in the NEI plasma of the element group (H–Mg, Si–S, Ar–Ca, Fe–Ni), on the other hand, show smooth increase in the order of the atomic mass (table 2): $kT_{\rm e} = 0.62 \pm 0.02$ keV (H–Mg), 0.80 ± 0.03 keV (Si–S), 1.00 ± 0.22 keV (Ar–Ca), and 2.76 ± 0.15 keV (Fe–Ni). These results suggest that the element groups are stratified. The stratified structure of the elements and the temperature distribution of the relevant plasma are consistent with numerical simulations of Type Ia SNe (e.g., Dwarkadas & Chevalier 1998). We note that Lopez et al. (2011) argued a Type Ia origin of G272.2−3.2 by the spherically symmetric structure, in contrast to the fact that CC SNRs generally have deformed shapes due to the interaction with the complex and dense environments, where the massive progenitors are born.

6.4.5 Ejecta Mass

If the ejecta are really a Type Ia origin, the plasma has no H nor He. With this assumption, we re-fit the whole region spectrum. The χ^2_ν (d.o.f.) becomes to be 1.16 (1999), that is equal to that of H-dominant plasma (1.16 (1998)). The best-fit parameters of the ejecta (VNEI) are almost the same as those of table 6.3 (Whole), but the normalization becomes to be $\int n_e n_{\rm C} dV/(4\pi d^2) = 2.8 \times 10^9\,{\rm cm^{-5}}$, where $n_{\rm C}$ represents the density of carbon. Using the SPEX software (Kaastra et al. 1996), we calculate $n_{\rm e}$ and $n_{\rm C}$ as $5 \times 10^{-2}\,(d_2.5)^{-0.5}\,f^{-0.5}\,{\rm cm^{-3}}$ and $2\times10^{-3}\,(d_{2.5})^{-0.5}\,f^{-0.5}\,{\rm cm^{-3}}$, respectively, where f is a filling factor. Therefore, the mass of the non-Fe ejecta is estimated to be $\sim 1.8\,(d_{2.5})^{2.5}\,f^{0.5}\,M_\odot$, while that of the Fe ejecta is only $\sim 6 \times\ 10^{-2}\,(d_{2.5})^{2.5}\,f^{0.5}\,M_\odot$. The mass of the non-

Fe ejecta is two or three times larger than that expected in a Type Ia SN (0.5–0.9 $M_{\odot}$; e.g., Maeda et al. 2010). However, adopting the lower limit of the distance of 2 kpc (see section 4.1) and the filling factor of 1/4, the non-Fe mass becomes to be $\sim 0.5\,M_{\odot}$ that is consistent with the Type Ia model. The mass of Fe is, on the other hand, too small, compared with that of the Type Ia. It may be due to the fact that only a small fraction of Fe in the center regions is heated by the reverse shock, which is often seen for young Type Ia SNRs (e.g., N103B: Lewis et al. 2003; SN 1006: Yamaguchi et al. 2008).

6.4.6 Hot Spot

G272.2−3.2 shows a spherical symmetric shape, the typical morphology of Type Ia SNRs (Lopez et al. 2011). We, however, find one singularity, which is the bright hot spot at the western edge of this SNR. From table 6.3, the surface brightness of the hot spot shows significant enhancement in the ISM plasma and Ne–Mg in the ejecta plasma. On the other hand, the abundances show no large deviation from the mean radial profile (figure 6.6). Thus the origin of the hot spot would be a dense ISM. It must be heated up by the light elements of ejecta located in the outer layer.

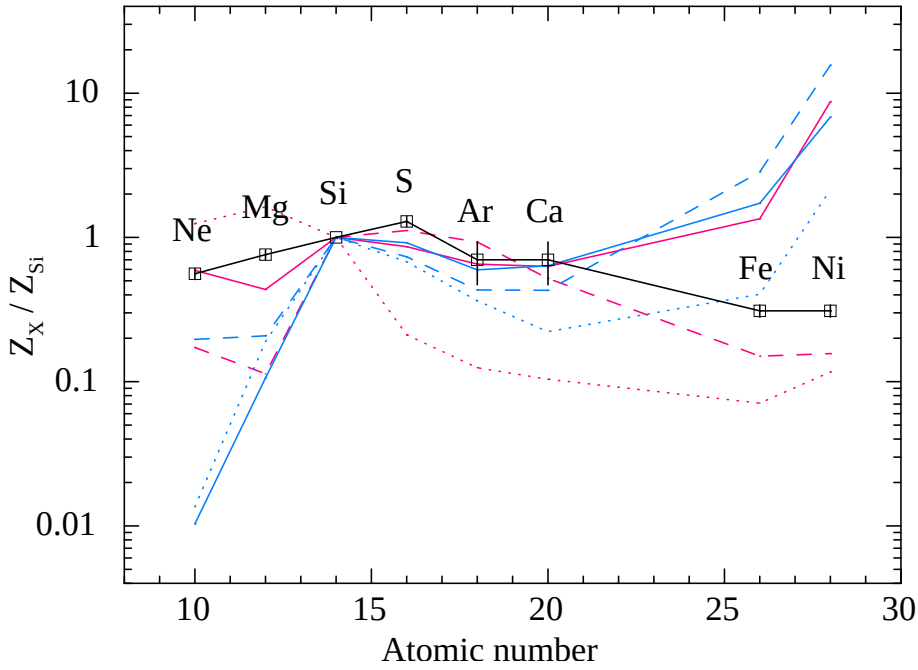

Figure 6.7: Metal abundances as a function of atomic number derived from the spectral fitting. The color lines represent several nucleosynthesis models for core-collapse SNe with different progenitor masses of 11 $M_\odot$ (red solid line), 20 $M_\odot$ (red dashed line), and 30 $M_\odot$ (red dotted line) from Woosley & Weaver (1995), and for Type Ia SNe, W7 (blue solid line), C-DEF (blue dashed line), and C-DDT (blue dotted line) from Maeda et al. (2010).

6.5 Summary

We have analyzed the Suzaku/XIS data of the Galactic SNR, G272.2−3.2. The results are summarized as follows:

1. The X-ray emission from G272.2−3.2 consists of two types of components, one is a CIE plasma and the other is a NEI plasma.

2. The CIE plasma has roughly solar abundances, and hence is likely the ISM origin, while the NEI plasma has super-solar in the central region, indicating the ejecta origin.

3. In the NEI plasma, we discover the K-shell lines of Ar, Ca and Fe. The Fe is in a low ionization state, which would be recently heated by a reverse shock.

4. The abundances of the ejecta have different radial distributions; Ne is almost constant across the radius, while Si–Ca and Fe concentrate at the center. The lighter elements have lower temperatures than those of the heavier elements.

5. Based on the morphologies of the ejecta and ISM, the presence of nearly neutral Fe and the ejecta mass, we conclude that the origin of G272.2−3.2 is a Type Ia SN rather than a CC SN.

Chapter 7

3C 397

7.1 Previous Results

3C397 (G41.1−0.3) is an SNR located near the Galactic plane. It has a peculiar rectangular morphology with a size of $2\farcm5 \times 4\farcm5$, elongated along the southeast to the northwest direction, perpendicular to the Galactic plane (figure 7.1). The SNR is located in the dense circumstellar environment. The ^{12}CO observation (Jiang et al. 2010) revealed that the western boundary of the remnant was interacting with molecular clouds based on its line broadening. The morphological agreement between the SNR and the molecular features also suggested the distance of ~ 10 kpc. It is consistent with the estimation from the interstellar absorption (6.4–12.8 kpc; Caswell et al. 1975). The density of the molecular clouds becomes large toward the west part of the remnant.

In this SNR, the compact object, such as a neutron star or a black hole, is not found. In the radio band, Dyer & Reynolds (1999) found that the remnant is unpolarized at 20 cm wavelength and has a mean fractional polarization of 1.5 % at 6 cm. The polarization peaks, however, did not coincide with the location of the hot spot observed in X-rays. Safi-Harb et al. (2005) ruled out the possibility of a pulsar or a PWN for the hot spot by the high resolution X-ray image by *Chandra*. Although they found two point sources in the observed field, they concluded that neither of them was not associated with the remnant.

The origin of 3C397 (core-collapse or Type Ia) has been still debated. It is because any previous studies could not succeed to separate the ejecta from the ISM. Chen et al. (1999) analyzed the *ASCA* and *ROSAT* data and found a two component NEI plasma. The low-temperature ($kT_\mathrm{e} \sim 0.2$ keV) component, containing Mg, Si K-shell and Fe L-shell lines, was approaching ionization equilibrium ($n_\mathrm{e}t > 3\times10^{11}$ cm^{-3}s), while the high-temperature ($kT_\mathrm{e} \sim 2.5$ keV) component, emitting S and Fe K-shell lines, was in a lower ionization state

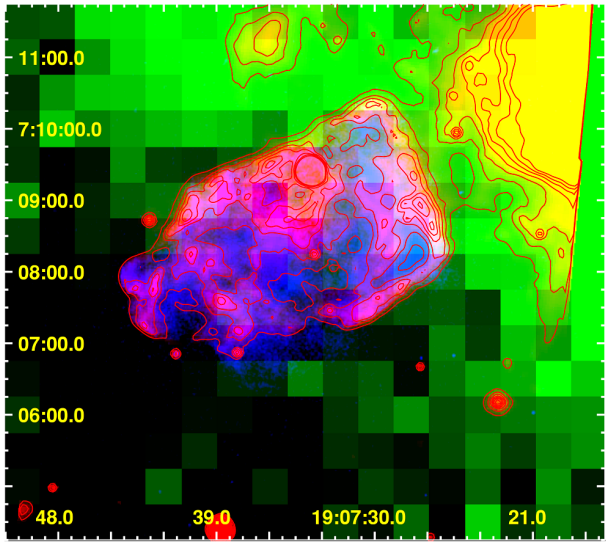

Figure 7.1: Multi-wavelength image of 3C397: (Green) ^{12}CO (J =1–0) intensity map in the velocity interval 27–35 kms^{-1}, (blue) The *Chandra* X-ray profile, (red) *Spitzer* 24 μm mid-IR image, and (yellow) the foreground H$_{\rm II}$ region at $V_{\rm LSR} \sim 59$ kms^{-1}. This image is taken from figure 3 of Jiang et al. (2010).

($n_{\rm e}t \sim 6 \times 10^{10}$ cm^{-3}s). They argued that the low-temperature component arose from the shocked dense cloud matter, while the high-temperature component was the shocked low-density intercloud matter, including some amount of the ejecta. Safi-Harb et al. (2000, 2005), analyzing the *ASCA* and *Chandra* spectra respectively, also obtained a similar two component NEI plasma, but could not extract the pure ejecta component from the spectra. Yang et al. (2013), on the other hand, analyzed the hard band spectrum with *Suzaku* and discovered the K-shell lines of Cr and Mn. They suggested that 3C397 was Type Ia origin based on equivalent width ratio of Cr to Fe K-shell line (EW(Cr)/EW(Fe)$>$ 2 %). Yamaguchi et al. (2014) also supported the Type Ia origin from the center energy of Fe K-shell line ($6.556^{+0.004}_{-0.003}$ keV). Yamaguchi et al. (2015) argued that the high Ni/Fe and Mn/Fe mass ratios indicated a single-degenerate origin for 3C397. However, these results are not a robust evidence for the typing, and the spectral separation of the ejecta from the ISM is an open question.

7.2 Observation and Data Reduction

The Suzaku satellite observed 3C 397 with XIS on 2010 Oct 24 and 2013 Oct 30. The observation log is given in table 7.1. Three of XISs (XIS 0, 1 ,3) were operated in the normal full-clocking mode with a SCI technique. The amount of the injection charge was 2 keV for the FI CCDs (XIS 0, 3) on both observations, while for the BI CCD (XIS 3) it was 2 keV on the first observation and 6 keV on the second observation. The XIS data were reprocessed with the calibration data base (CALDB) released in 2014 February. We used the HEASOFT version 6.16 for the data reduction and XSPEC version 12.8.2 for the spectral analysis. The total exposure times of the first and the second observations, after the standard screening, are about 69 ks and 104 ks, respectively.

Table 7.1: Observation logs of 3C 397.

Target	Obs. ID	Obs. Date	R.A.	Dec.	Exposure
			(J2000.0)		(ks)
3C 397	505008010	2010-Oct-24	$19^{h}7^{m}36.9^{s}$	$-7\,°7\,'20.3\,''$	69.3
3C 397	508001010	2013-Oct-30	$19^{h}7^{m}38.2^{s}$	$-7\,°7\,'21.4\,''$	103.5

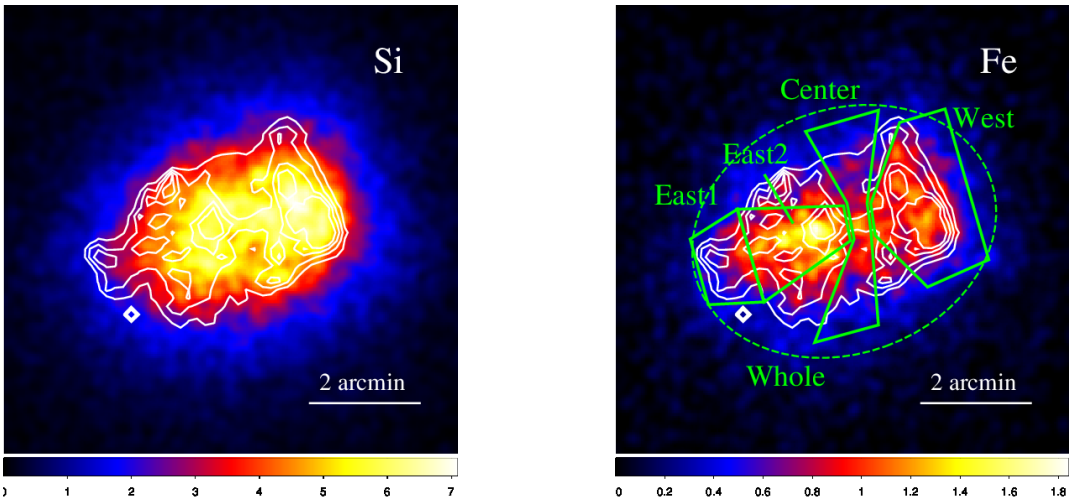

Figure 7.2: XIS images of 3C 397 in the 1.80–1.92 keV band (Si-band: left) and 6.40–6.70 keV band (Fe-band: right). The X-ray profile of 0.6–10 keV band obtained by the *Chandra* is overlaid in white contours. The spectral extraction regions are shown with green lines.

7.3 Analyses and Results

7.3.1 Imaging Analysis

Figure 7.2 shows the narrow band images of the 3C 397 in the energy bands of 1.80–1.92 keV (Si K-shell) and 6.40–6.70 keV (Fe K-shell). We combine all the XIS data of the two observations to maximize the photon statistics. Since we find the inconsistency in the source positions of the two observations, maybe due to the position accuracy of *Suzaku* (Uchiyama et al. 2008), we shift the second observation image 0.′5 toward the southeast before combining the data.

We see distinctly different structures among these two images: the intensity of Si-K becomes large toward the west, while the Fe-K is concentrated at the east. The narrow band image of S K-shell (2.41–2.51 keV) also has a similar profile to that of Si K-shell band, and those of Mg K-shell (1.28–1.42 keV) and Fe L-shell (1.18–1.28 keV) are similar to that of Fe K-shell band. These results clearly suggest that the plasma state varies from the west to the east in this SNR.

7.3.2 Spectral Analysis

Analysis of Whole region Spectrum

Since the size of 3C397 ($2.'5 \times 4.'5$) is enough small compared to the XIS field ($17.'8 \times 17.'8$), we generate the BG spectrum from the same field. We define the SNR region (Whole) as a ellipse of $4.'4 \times 5.'6$ as shown by a green dashed line in figure 7.2, while the BG region is the FoV of XIS, excluded the SNR and the calibration source regions. We make an XB spectrum from the BG region subtracting the relevant NXB. The spectrum from the Whole region is also made and subtracted the NXB. We then subtract the XB spectrum from the Whole region spectrum after the vignetting and area corrections, assuming the uniform distribution of the XB in the field. The resultant spectrum is shown in figure 7.3. As reported in the previous studies (Yang et al. 2013; Yamaguchi et al. 2015), the K-shell lines of Cr, Mn, Fe, and Ni are clearly detected in the *Suzaku* spectrum, including the K-shell lines of Mg, Si, S, Ar, and Ca.

We firstly apply an NEI plasma model (VNEI) with interstellar absorption. A Gaussian line at 1.2 keV is also added in order to compensate for the insufficiency of Fe L-shell emissivities (e.g., Yamaguchi et al. 2011). In this fit, the column density $N_{\rm H}$, the electron temperature $kT_{\rm e}$ and ionization timescale $n_{\rm e}t$ are free parameters. The abundances of Mg, Al, Si, S, Ar, Ca, Cr, Mn, Fe, and Ni are also free parameters. However, this model is not statistically acceptable with χ^2_ν (d.o.f.) = 2.4 (3532) (figure 7.3 panel (a)).

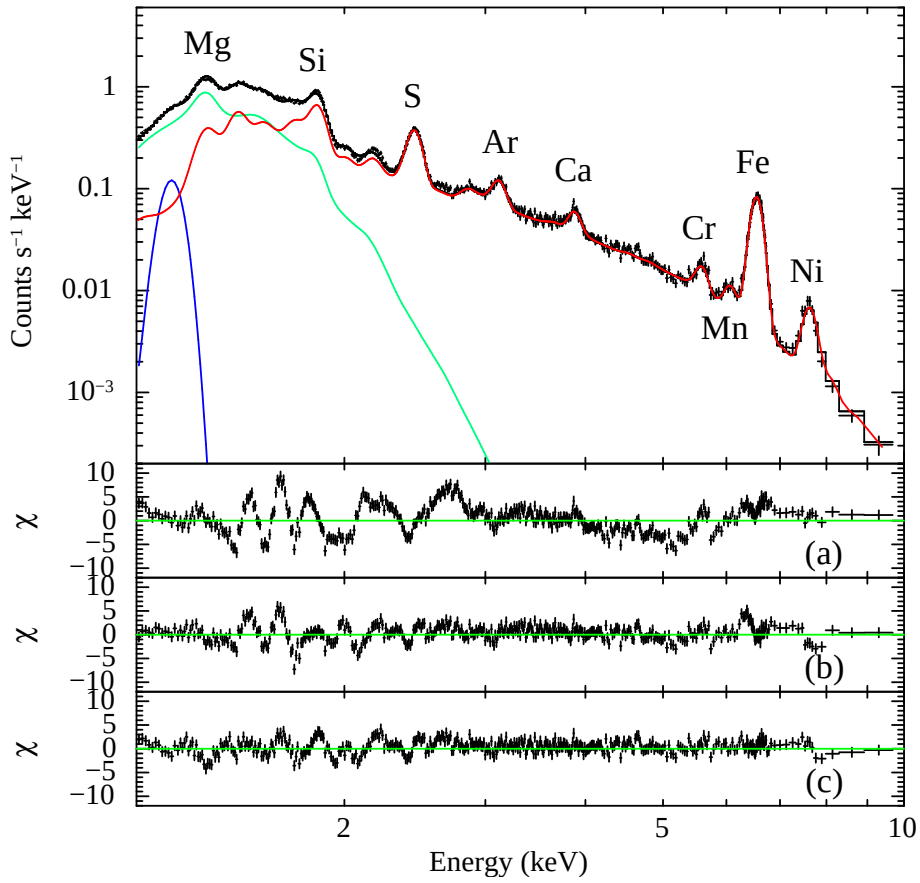

Figure 7.3: Whole region spectrum of 3C397. Only the FI spectrum is displayed for the visibility. The spectrum is fitted with Model A, multi-NEI (red) + CIE (green), adding a Gaussian line (blue). The lower panels represent the residuals from the source models of (a) NEI, (b) NEI + CIE, and (c) multi-NEI + CIE, respectively.

Table 7.2: Best-fit parameters for the SNR spectra of 3C397.

Component	Parameter	Whole	East1	East2	Center	West
Absorption	$N_{\rm H}$ ($10^{22}{\rm cm}^{-2}$)	3.26 ± 0.06		3.26 (fixed)		
VNEI-1	$kT_{\rm e}$ (keV)	0.72 ± 0.03		0.72 (fixed)		
	Mg	2.23 ± 0.20	1.15 ± 0.57	2.64 ± 0.27	2.24 ± 0.18	2.55 ± 0.13
	Al	4.02 ± 0.51	< 1.7	3.53 ± 0.67	4.20 ± 0.49	5.54 ± 0.39
	Si	0.97 ± 0.08	1.43 ± 0.21	1.26 ± 0.08	0.96 ± 0.05	1.14 ± 0.04
	S	1.60 ± 0.11	2.23 ± 0.28	2.00 ± 0.11	1.50 ± 0.07	1.60 ± 0.05
	$n_{\rm e}t$ ($10^{11}{\rm cm}^{-3}\,{\rm s}$)	6.0 ± 1.6		6.0 (fixed)		
	$EM^{\dagger}$ ($10^{12}{\rm cm}^{-5}$)	10.3 ± 0.7	0.249 ± 0.024	1.12 ± 0.05	1.18 ± 0.04	3.49 ± 0.08
VNEI-2	$kT_{\rm e}$ (keV)	1.00 ± 0.38		1.00 (fixed)		
	Ar	0.86 ± 0.35	0.84 ± 0.23	1.23 ± 0.12	0.78 ± 0.08	0.89 ± 0.06
	Ca	0.80 ± 0.41	< 0.49	1.04 ± 0.14	0.84 ± 0.10	0.96 ± 0.08
	$n_{\rm e}t$ ($10^{10}{\rm cm}^{-3}\,{\rm s}$)			(Linked to NEI 1-a)		
	$EM^{\dagger}$ ($10^{11}{\rm cm}^{-5}$)			(Linked to NEI 1-a)		
VNEI-3	$kT_{\rm e}$ (keV)	2.36 ± 0.10		2.36 (fixed)		
	Cr	2.23 ± 0.17	3.1 ± 1.4	2.98 ± 0.53	2.49 ± 0.37	2.40 ± 0.27
	Mn	4.92 ± 0.46	8.1 ± 4.1	8.2 ± 1.5	4.9 ± 1.0	5.10 ± 0.73
	Fe	0.64 ± 0.03	1.28 ± 0.15	1.03 ± 0.05	0.55 ± 0.02	0.60 ± 0.02
	Ni	1.66 ± 0.16	< 1.9	2.13 ± 0.45	1.45 ± 0.31	2.24 ± 0.22
	$n_{\rm e}t$ ($10^{11}{\rm cm}^{-3}\,{\rm s}$)	1.18 ± 0.09		1.18 (fixed)		
	$EM^{\dagger}$ ($10^{11}{\rm cm}^{-5}$)			(Linked to NEI 1-a)		
APEC	$kT_{\rm e}$ (keV)	0.155 ± 0.005		0.155 (fixed)		
	All metals	0.10 (fixed)		0.10 (fixed)		
	$EM^{\dagger}$ ($10^{15}{\rm cm}^{-5}$)	30.2 ± 8.3	1.78 ± 0.06	4.72 ± 0.10	2.99 ± 0.07	8.73 ± 0.15
χ^2_ν (d.o.f.)		1.19 (3490)	1.17 (825)	1.10 (1663)	1.06 (1657)	1.13 (2289)

The main residual comes from the low energy band of 1–3 keV. Therefore, we add a CIE plasma (APEC). This model (NEI + CIE) improves χ^2_ν (d.o.f.) to 1.54 (3529), although the residuals at 1.4–1.8 keV and Fe-K band still stand out (figure 7.3 panel (b)). The former is due to the inconsistency of the continuum spectrum, and the latter is due to the line broadening of the Fe-K line. Thus, for further improved fit, we divide a VNEI into three components, they stand for H–S, Ar–Ca, and Cr–Ni, respectively. We convolve the Fe-group component (Cr–Ni) with a gsmooth, which is a line broadening model in XSPEC. We let the temperatures of these three components vary freely, but link the ionization timescales except for the Fe-group. Since the abundances of APEC approach zero in this fit, we fix the abundances at 0.1 solar. This model (multi-NEI + CIE) largely improves χ^2_ν (d.o.f.) to 1.19 (3490) (figure 7.3 panel (c)), almost acceptable taking account of the systematic errors. The best-fit spectrum and parameters are summarized in figure 7.3 and table 7.2, respectively.

Analysis of Spatially Resolved Spectra

We next perform the spatially resolved analysis of 3C397. As seen in section 7.3.1, the plasma states of 3C397 varies from the east to the west. The *Chandra* image (white contour in figure 7.2) also has a dark lane running north-south direction and a protrusion in the most east part. Hence, we divide the SNR into four regions: East1, East2, Center, and West (figure 7.2 right).

We analyze the spectra with the same model as Whole region. We fix the column density, temperatures, and ionization timescales to those of Whole region. We also fix the S abundance due to its large statistical error. The fit results are statistically acceptable for all the regions (χ^2_ν =1.06–1.17). The best-fit spectra and parameters are summarized in figure 7.4 and table 7.2.

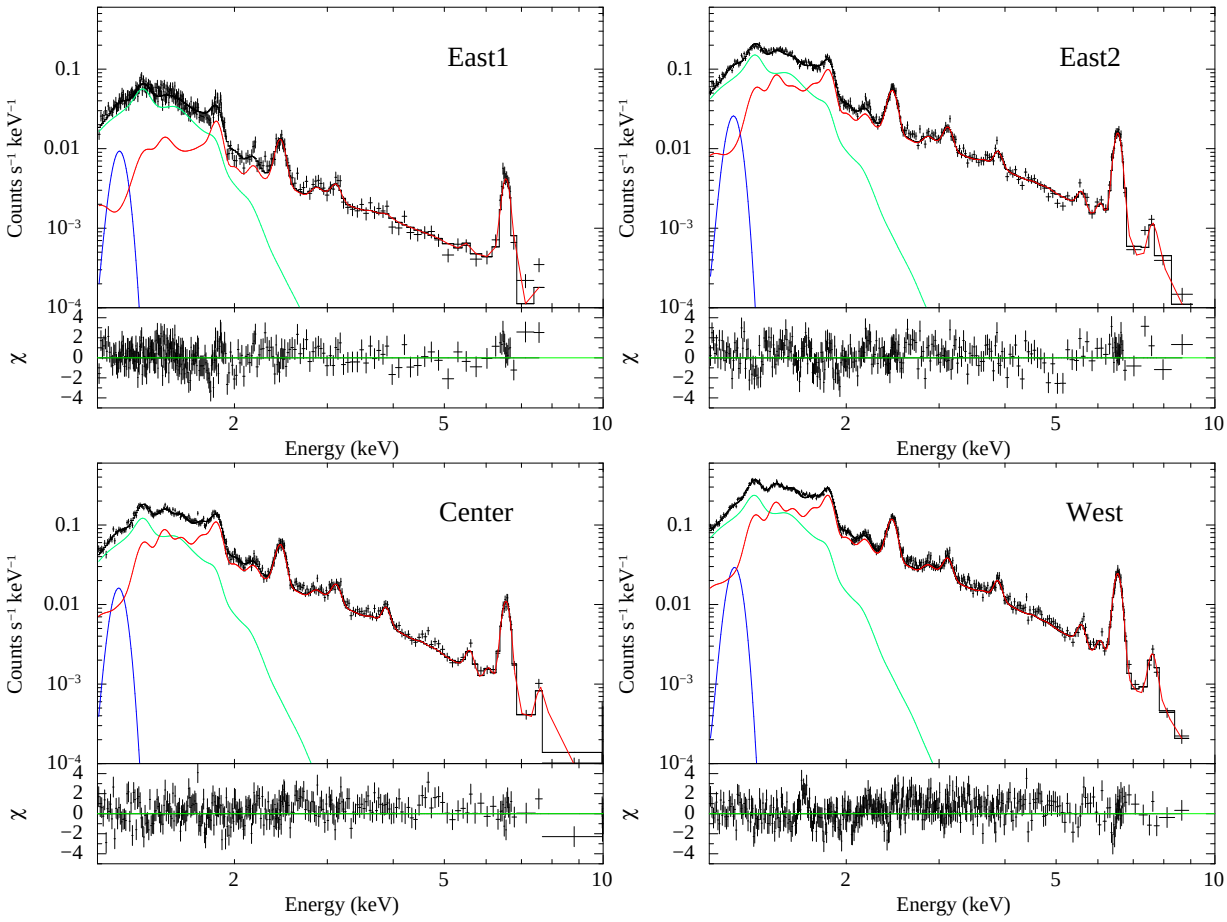

Figure 7.4: Spectra obtained from four regions: East1, East2, Center, and West. The same model as in figure 7.3 is applied.

7.4 Discussion

7.4.1 Plasma Components

We find that the X-ray spectrum of 3C397 is well described with two types of components, a low-temperature CIE plasma ($kT_{\rm e} = 0.155 \pm 0.005$ keV) and a high-temperature multi-NEI plasma ($kT_{\rm e} = 0.72 \pm 0.03$ keV, 1.00 ± 0.38 keV, and 2.36 ± 0.10 keV). This result is roughly similar to those of the previous studies (Chen et al. 1999; Safi-Harb et al. 2005), in which they employed two-temperature components of ~ 0.2 keV and ~ 2 keV. Since the low-temperature plasma has the abundances of 0.1 solar, it is likely the swept-up ISM. The high-temperature plasma has an enhanced metal abundances, hence it would be ejecta origin. Based on this best-fit model, we discuss the progenitor type of 3C397 in the following subsections.

7.4.2 Relative Abundance and Mass of the Ejecta

We compare our best-fit relative abundances of the high-temperature plasma with the predicted nucleosynthesis yield of core-collapse (Woosley & Weaver 1995) and Type Ia (Maeda et al. 2010) SNe. Although the relative abundances of light elements (Mg and Al) are close to the core-collapse model with progenitor mass of $M = 30\,M_{\odot}$, those of intermediate mass and Fe-group elements favor the Type Ia models. Most remarkable feature is the abundance pattern of Fe-group elements. The abundance ratios of Cr, Mn and Ni to Fe are $Z_{\rm Cr}/Z_{Fe} = 3.48 \pm 0.31$, $Z_{\rm Mn}/Z_{Fe} = 7.69 \pm 0.80$ and $Z_{\rm Ni}/Z_{Fe} = 2.59 \pm 0.28$, which cannot be reproduced by any core-collapse models. These abundance ratios are roughly consistent with those estimated by Yamaguchi et al. (2015), $Z_{\rm Ni}/Z_{Fe} = 2.8 \pm 0.7$, $Z_{\rm Mn}/Z_{Fe} = 4.9 \pm 1.6$ and $Z_{\rm Ni}/Z_{Fe} = 4.3 \pm 1.5$, who argued the single degenerate progenitor for 3C397.

On the other hand, assuming the distance of 10 kpc, the volume of 3C397 is estimated to be $1.6 \times 10^{58}\,{\rm cm}^3$. Then, the ejecta mass is estimated to be $M = 48\ (d_{10})^{2.5}\ f^{-0.5}\,M_{\odot}$ from the emission measure. Even if we assume the Type Ia abundance for lighter elements than Mg, the ejecta mass does not decrease larger than a factor of 3. Therefore, based on the ejecta mass, 3C397 is likely a core-collapse origin.

7.4.3 Spatial Distribution

The peculiar rectangular morphology of 3C397 elongated along southeast to northwest is not still understood. Jiang et al. (2010) showed that the ambient cloud has a column density gradient increasing from southeast to northwest. They also found the direct

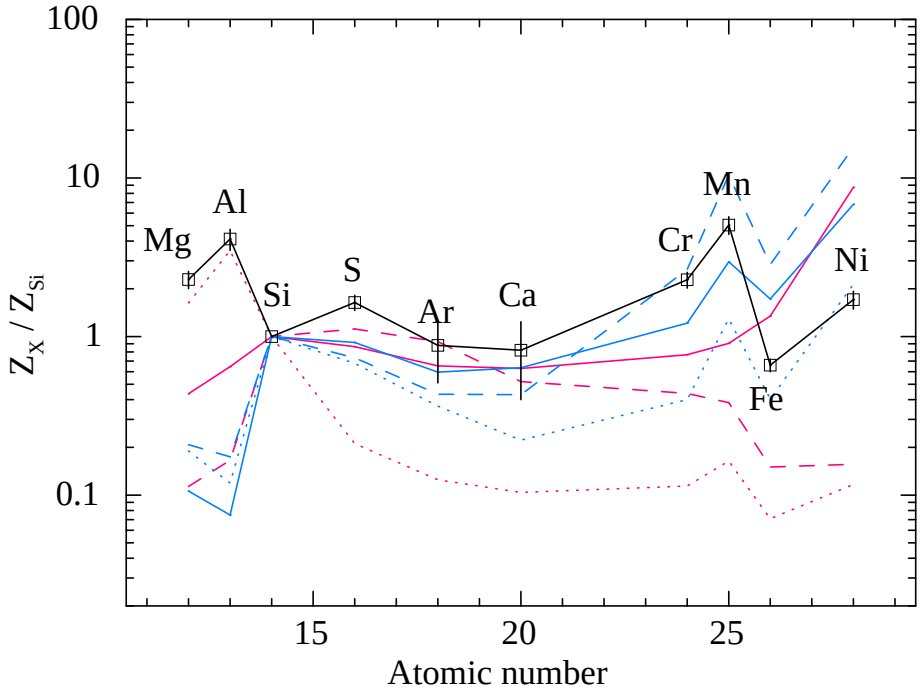

Figure 7.5: Metal abundances as a function of atomic number derived from the spectral fitting. The color lines represent several nucleosynthesis models for core-collapse SNe with different progenitor masses of 11 $M_\odot$ (red solid line), 20 $M_\odot$ (red dashed line), and 30 $M_\odot$ (red dotted line) from Woosley & Weaver (1995), and for Type Ia SNe, W7 (blue solid line), C-DEF (blue dashed line), and C-DDT (blue dotted line) from Maeda et al. (2010).

evidence of the interaction between the SNR and the molecular cloud with a ^{12}CO line broadening. However, these direction is perpendicular to that of the narrow side of 3C397.

In our analysis, the ejecta abundances show a significant distribution varying from east to west: the abundances of Fe-group elements become large toward the east of the remnant (table 7.2). It might suggest that the SN which formed 3C397 caused an unipolar explosion to the east. Such an asymmetric explosion favors a core-collapse origin for this SNR.

7.4.4 Another Solution for the Plasma Components

The ejecta abundances of heavy elements favor a Type Ia origin for 3C397, while those of light elements, the mass, and distribution indicate a core-collapse origin. We suspect that these anomaly are caused by the failure on the separation of the ejecta from the ISM. If the ISM contaminates the soft-band spectra of the ejecta, the real abundances of light elements become lower, approaching the Type Ia abundances. In this case, the mass and distribution should also differ from the current model.

In fact, the emission measure of the ISM in the current model is inordinately large. Assuming the volume of $1.6 \times 10^{58}\,\mathrm{cm}^3$, this emission measure leads to the average ISM density of $n_0 = 140\,\mathrm{cm}^{-3}$ and the mass of $\sim 2600\ f^{0.5}\,M_\odot$. In such a dense environment, the SNR cannot expand due to the higher pressure of the ISM than ejecta. The above mass also corresponds to the thermal energy of $4 \times 10^{51}\ f^{0.5}\,\mathrm{erg}$, which is one or two order of magnitude greater than those of typical SNRs ($\sim 10^{49-50}$ erg).

Although we express the excess in 1–2 keV spectrum by the bremsstrahlung continuum of the ISM component, its features might be strong Fe or Ni L-shell lines, characteristic for Type Ia SNRs. We examine this assumption, but cannot obtain any acceptable models. The main reason might be the uncertainty of Ni L-shell emissivities. In the current atomic code, the theoretical emissivities are employed for these lines. Figure 7.6 shows one example of our fitting trials. In this figure, we fixed the abundance ratio of Ni/Fe as 3 in order to fit the Ni-K line (panel (a)). If we let the Ni abundance free and ignore the Ni-K band, the 1.6 keV residual is improved (panel (b)), but the abundance ratio of Ni/Fe becomes $\sim$ 10. In this model, the emission measure of the ISM ($\sim 1.7 \times 10^{13}\ \mathrm{cm}^{-5}$) is smaller than that of the best-fit model due to the higher electron temperature ($kT_\mathrm{e} \sim 0.55\,\mathrm{keV}$). In order to identify the spectral components of 3C397, we need a higher resolution spectrum such by ASTRO-H/SXS. Since SXS has superior spectral resolution around 5 eV, it can resolve the triplet (resonance, forbidden, and inter-combinations) of Mg Heα, from which we can directly estimate the electron temperature of the ISM.

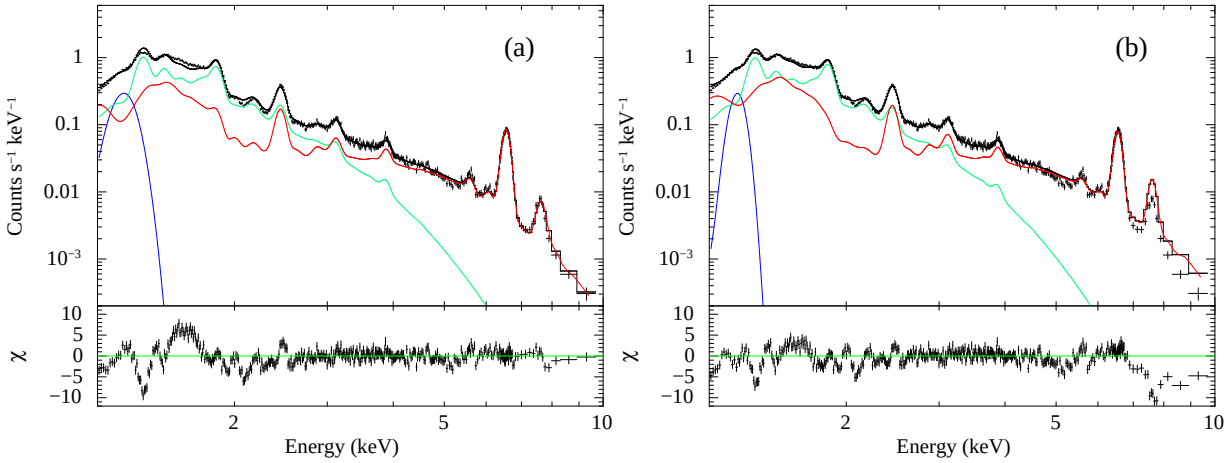

Figure 7.6: Contributions of Ni L-shell lines in the low energy band of 3C397. In panel (a), the spectrum is fitted with the fixed abundance ratio of Ni/Fe= 3 for the K-shell line intensities, while the fitting in panel (b) ignore the Ni K-shell band, and lead to the abundance ratio of Ni/Fe$\sim$ 10.

7.5 Summary

We have analyzed the high-quality spectra of 3C397 obtained with *Suzaku*. The results and interpretations are summarized as follows:

1. The spectra consists of a low-temperature CIE plasma ($kT_{\rm e} \sim 0.16\,{\rm keV}$) and a high-temperature multi-NEI plasma ($kT_{\rm e} = 0.7$–$2.4\,{\rm keV}$).

2. The low-temperature component has abundances of 0.1 solar, hence is likely the ISM origin, while the high-temperature component has super-solar, indicating the ejecta origin.

3. The ejecta abundances of intermediate mass and Fe-group elements are consistent with Type Ia ejecta, while those of light elements, mass, and asymmetric distribution favors a core-collapse origin.

4. The anomaly of the typing might be caused by a failure on the separation of the ejecta from the ISM, but it cannot be identified with a current spectral quality.

Chapter 8

Discussion

8.1 Summary of Analysis results

In the previous chapter, we analyzed the data of four Galactic SNRs (G292.0+1.8, G290.1−0.8, G272.2−3.2, and 3C397) obtained with the *Suzaku* satellite. The superior performance of *Suzaku* has enabled us to lead a lot of new results. The results are summarized as follows,

- We discovered new spectral features which were not detected by other satellites: Fe-K for G292.0+1.8, Si RRC for G290.1−0.8, Ar, Ca, Fe-K for G272.2−3.2.
- We successfully separated the ejecta from the ISM on G292.0+1.8 and G272.2−3.2 in the broadband X-ray spectra, but failed for 3C397, which maybe due to the Ni L-shell uncertainty in the current atomic code. On the other hand, we identified the ejecta dominant region in G290.1−0.8.
- Based on the ejecta abundances and masses, we concluded that G292.0+1.8 and G290.1−0.8 are a core-collapse origin, while G272.2−3.2 is a Type Ia origin. The ejecta abundances distribute uniformly in the core-collapse SNRs, but in G272.2−3.2 we found the abundance stratification.
- We also discovered the recombining plasma in the ejecta dominant region of G290.1−0.8.

We further discuss the ejecta natures in the following section. In order to examine the difference between core-collapse and Type Ia SNRs more systematically, we summarize the physical parameters of the Galactic SNRs, in which the ejecta are clearly separated from the ISM, in table 8.1. Since Yamaguchi et al. (2014) reported that the ionization states of Fe K-shell lines can be one of the most distinct criteria discriminating the types of SNRs, we focus on the Fe-K detected SNRs so far.

Table 8.1: Physical parameters of Fe-K detected Galactic SNRs, obtained with *Suzaku*.[a]

Name[b]	$N_{\rm H}$ ($10^{22}{\rm cm}^{-2}$)	$kT_{\rm e,ISM}$ (keV)	$kT_{\rm e,ej}$ (keV)	$n_{\rm e}t$[Si] ($10^{11}{\rm cm}^{-3}{\rm s}$)	$n_{\rm e}t$[Fe] ($10^{11}{\rm cm}^{-3}{\rm s}$)	n_0 (${\rm cm}^{-3}$)	n_e (${\rm cm}^{-3}$)	$M_{\rm ISM}$ ($M_\odot$)	$M_{\rm ej}$ ($M_\odot$)	($f_{\rm ISM}$: $f_{\rm ej}$)	Volume (10^{58} ${\rm cm}^3$)	Age (yr)	Refs[c]
Core-collapse SNRs													
Cas A	1.3	2	2	2	8	3.9	0.7	9	3	—	0.23	310–350	1, 2
G292.0+1.8	0.444 ± 0.019	0.72 ± 0.01	1.07 ± 0.19	3.0 ± 2.6	0.86 ± 0.19	2.4	0.6	70	25	(0.25 : 0.75)	6.0	~ 2900	3
G349.7+0.2	6.4 ± 0.1	0.60 ± 0.02	1.24 ± 0.02	20 ± 2	$= n_{\rm e}t$[Si]	5.5	5.3	25	35	(0.25 : 0.75)	0.9	~ 3500	4
G350.1−0.3	3.3 ± 0.1	0.48 ± 0.02	1.51 ± 0.05	3.5 ± 0.2	$= n_{\rm e}t$[Si]	3.7	1.7	21	14	(0.25 : 0.75)	1.1	~ 900	4
Type Ia SNRs													
Kepler	0.64	1.06 ± 0.02	2.08 ± 0.01	0.209 ± 0.003	0.0162^{+0}_{-0}	2.0	0.25	0.75	3.9	(0.09 : 0.57)	0.13	411	5
Tycho	1	0.41 ± 0.01	0.96 ± 0.01	$0.794^{+0.012}_{-0.011}$	0.0631 ± 0.0009	2.3	0.25	3.1	0.9	(0.2 : 0.53)	0.30	443	5
SN1006	0.0680 ± 0.0004	0.4 ± 0.1	0.48 ± 0.01	0.439 ± 0.003	0.0140 ± 0.0001	0.18	0.1	0.6	1.6	(0.25 : 0.75)	0.60	1009	6, 7
G272.2−3.2	0.99 ± 0.01	0.172 ± 0.003	0.80 ± 0.03	1.23 ± 0.10	0.1	1.2	0.06	13	1.6	(0.25 : 0.75)	2.0	3000–8000	8
G337.2−0.7	3.19 ± 0.01	0.75 ± 0.03	$1.54^{+0.08}_{-0.01}$	$3.6^{+0.1}_{-0.3}$	$0.21^{+0.02}_{-0.01}$	0.9	?	13	2.1	(0.25 : 0.16)	3.0	5000–7000	9
Unknown													
3C397	3.26 ± 0.06	0.155 ± 0.005	0.72 ± 0.03	6.0 ± 1.6	1.18 ± 0.09	170	3.5	1300	42	(0.25 : 0.75)	1.6	1500–5500	10

[a] Only the SNRs, in which the ejecta are separated from the ISM component, are listed.

[b] The physical parameters of Cas A are derived from the *Chandra* observations.

[c] References: (1) Hwang & Laming (2012); (2) Lee et al. (2014) (3) Kamitsukasa et al. (2014) (This work); (4) Yasumi et al. (2014); (5) Katsuda et al. (2015); (6) Yamaguchi et al. (2011); (7) Uchida et al. (2013); (8) Kamitsukasa et al. (2015a) (This work); (9) Takata et al. (2015); (10) Kamitsukasa et al. in prep. (This work)

8.2 Ejecta Abundances and Masses

We have discriminated the SNR types based on the ejecta abundances and masses in the previous analyses. In this section, we investigate the systematical trends between core-collapse and Type Ia SNRs on these observational values.

Figure 8.1 shows the metal abundance ratios relative to Si for the SNRs in table 8.1. The red and blue marks represent the abundances of core-collapse SNRs and those of Type Ia SNRs, respectively. We also overlay seven model prediction values by lines: the red lines are model values of core-collapse SNRs on several progenitor masses (dotted: 11 $M_\odot$, dot-dashed: 20 $M_\odot$, dashed: 30 $M_\odot$, solid: 40 $M_\odot$) by Woosley & Weaver (1995), while the blue lines are Type Ia models (solid: W7, dashed: C-DEF, dotted: C-DDT) by

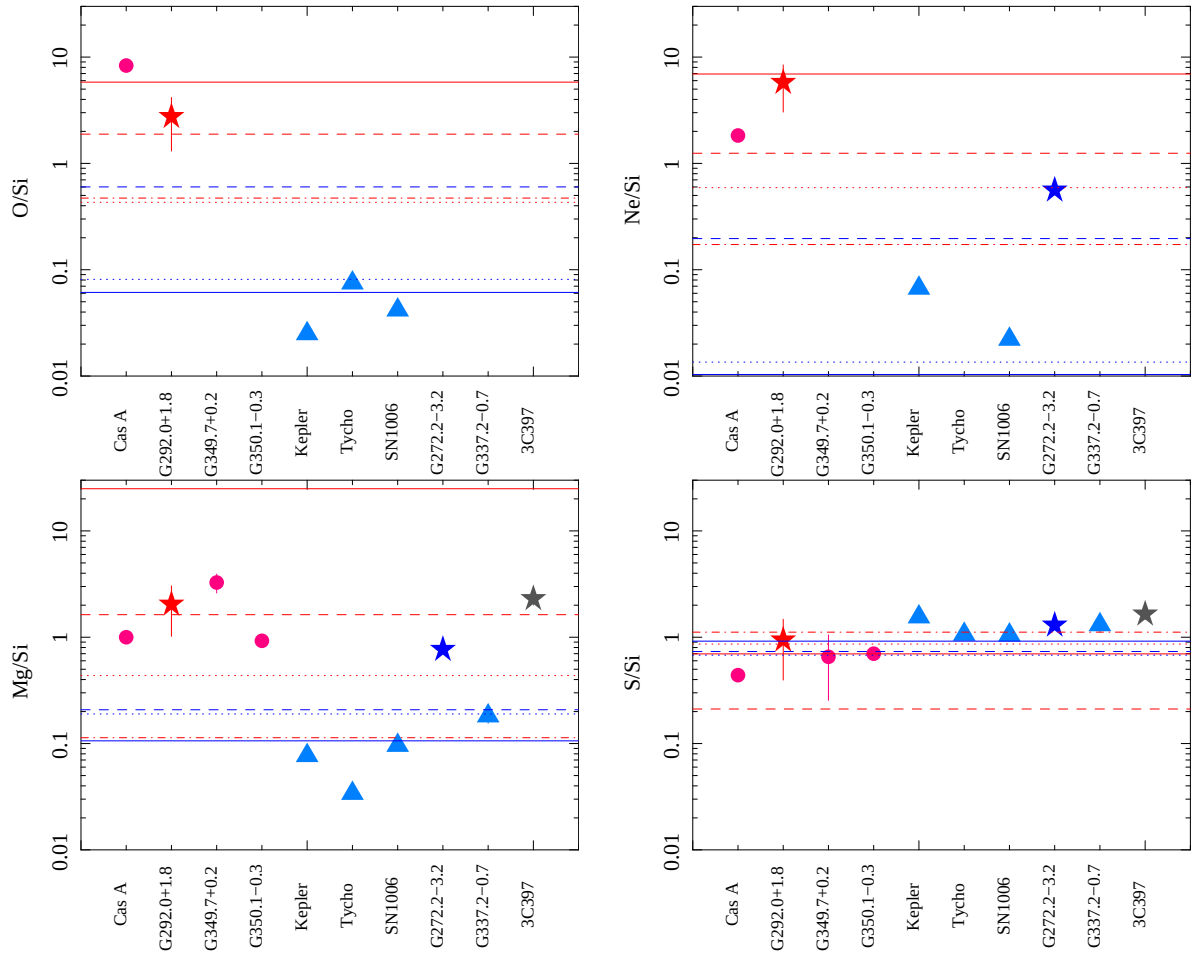

Figure 8.1: Metal abundance ratios relative to Si in the ejecta. The red lines are model prediction values of the core-collapse on several progenitor masses (dotted: 11 $M_\odot$, dot-dashed: 20 $M_\odot$, dashed: 30 $M_\odot$, solid: 40 $M_\odot$) by Woosley & Weaver (1995), while the blue lines are Type Ia models (solid: W7, dashed: C-DEF, dotted: C-DDT) by Maeda et al. (2010).

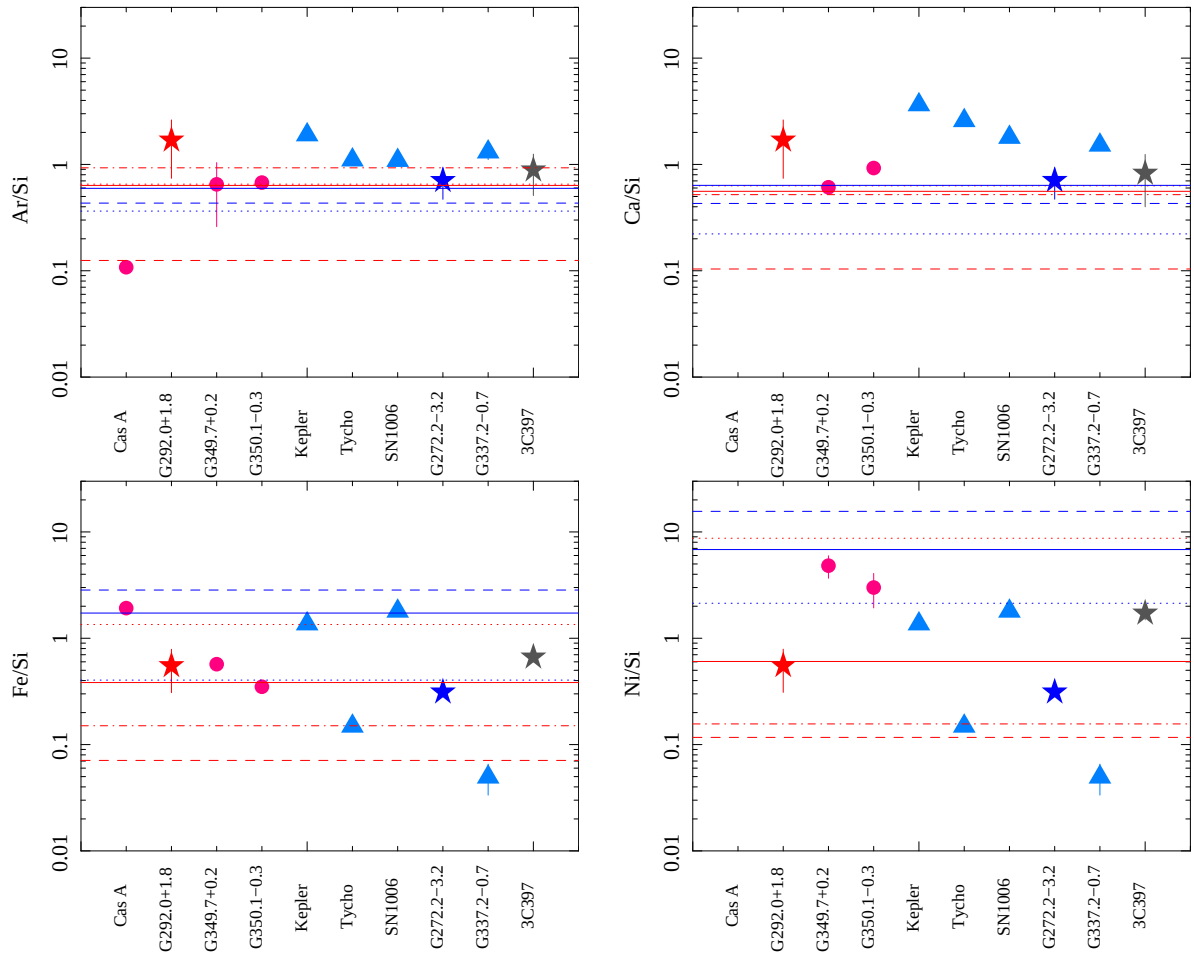

Figure 8.1: Continued.

Maeda et al. (2010). We see some trends in these plots: (1) the light elements of O, Ne, Mg of core-collapse SNRs are 10 times larger than those of Type Ia. (2) the intermediate mass elements, such as S, Ar, Ca, are roughly equal to Si. (3) the Fe-group elements, especially of Type Ia SNRs, have a large variety in their abundances.

The differences between the core-collapse and Type Ia SNRs on the light elements are consistent with the model prediction. The massive stars which lead to the core-collapse produce a large amount of light elements by the stellar nucleosynthesis, while the Type Ia transforms most part of a white dwarf to the intermediate and Fe-group elements by the explosive burning.

The intermediate mass elements are also generally consistent with the model values. However, the Ar and Ca abundances of some Type Ia SNRs (Kepler, Tycho, SN1006, and G337.2-0.7) are 2–3 times larger. We check the abundances of other Type Ia models including the recent 3D simulations, but all of these models predict that the Ar and Ca abundances are half (or equal at best) of the Si abundance. We suspect that the abundance anomaly comes from the temperature gradient between Si and Ar/Ca. In

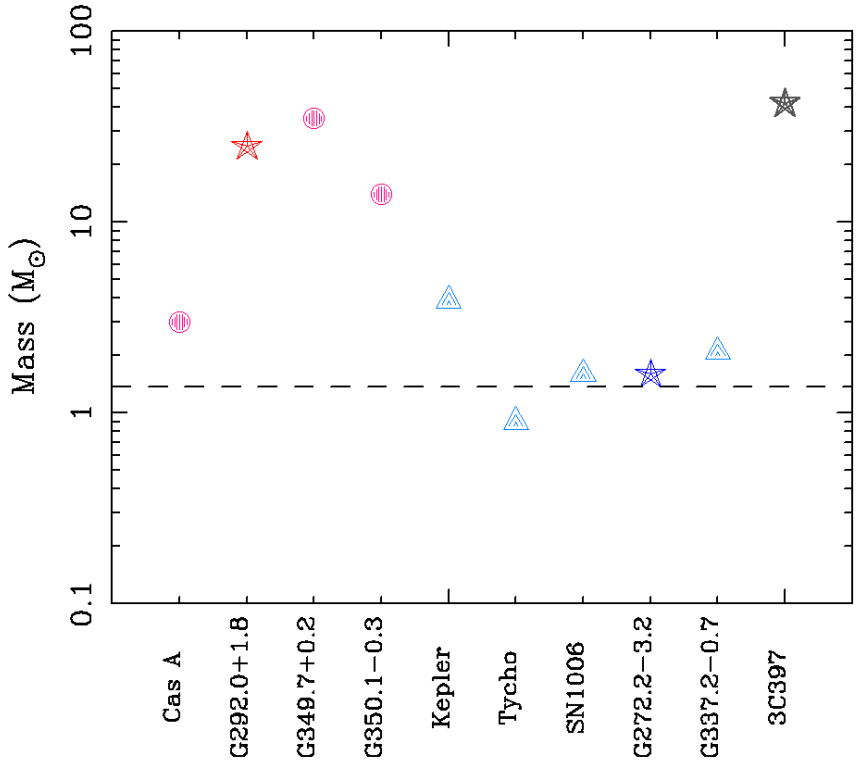

Figure 8.2: Estimated ejecta masses of Fe-K detected Galactic SNRs. The dashed line corresponds to the Chandrasekhar mass of a white dwarf ($M = 1.38\,M_\odot$).

the spectral analyses for these SNRs, the electron temperature of the intermediate mass elements are all linked. In fact, our analyses of G272.2−3.2 and 3C397, in which we let the electron temperatures free independently for each element, led the consistent values with the Type Ia models.

On the Fe-group abundances, it is guessed that the core-collapse SNRs have a large uncertainty because the amount of these elements depend on the location of the mass cut, which is not well-known. The Type Ia SNRs, on the other hand, have a uniformity. The observed values, however, show that the Type Ia SNRs have a larger variety on the Fe-group abundances. It suggests that the Fe-group elements in the Type Ia SNRs are recently heated by the reverse shock. Actually, the ionization states of Fe in the Type Ia SNRs are significantly lower than those of the core-collapse SNRs as suggested by Yamaguchi et al. (2014). Therefore, only a small fraction of Fe-group elements is detected except 3C397, which is located in a more dense circumstellar environment than others. The ionization states of Fe are discussed again in section 8.3.

Figure 8.2, on the other hand, shows the ejecta masses. We can see that the masses are differently distributed between the core-collapse ($M \sim 10\,M_\odot$) and Type Ia SNRs

($M \sim 1\,M_{\odot}$). Although we must note that these masses depend on the filling factor ($M \propto f^{0.5}$), the masses are roughly consistent with the expected values of the core-collapse and Type Ia SNRs. Thus, it is enough useful to employ the ejecta mass in addition to the abundances for discriminating the type of SNRs.

8.3 Ejecta Distribution

We obtained the results that the ejecta abundances distribute uniformly in the core-collapse SNRs (G292.0+1.8 and G290.1−0.8), while in the Type Ia SNR, G272.2−3.2, the abundances of heavy elements are more enhanced in the center regions than those of light elements. Although we could not find the abundance distribution in the Type Ia SNR, 3C397, it might be because the morphology of the SNR is highly disturbed by the nonuniform dense ISM.

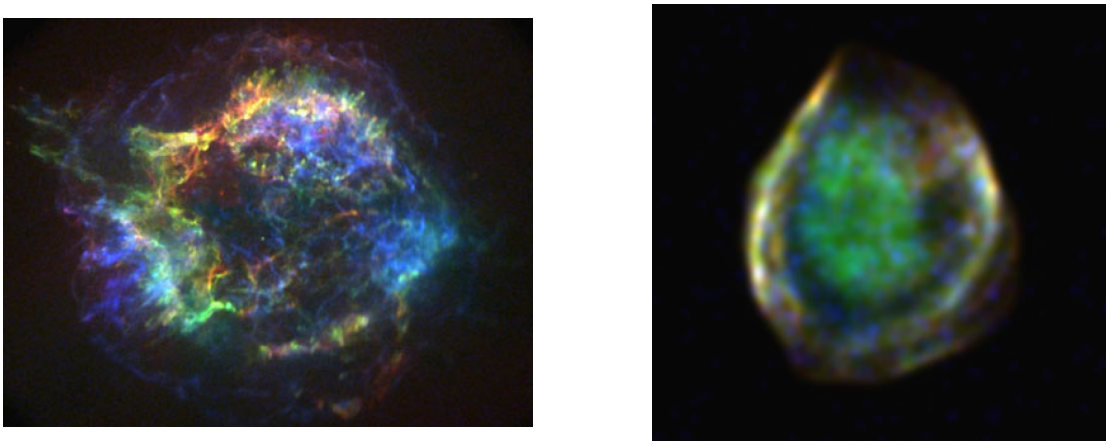

Figure 8.3: Typical ejecta distributions for core-collapse (left: Cas A) and Type Ia SNRs (right: DEM L71). The images are taken from Vink (2012).

Generally, it is believed that in the core-collapse SNRs the ejecta distribute more asymmetric and well mixed by the fluid instability, whereas in the Type Ia it distributes symmetric and stratified as seen in figure 8.3. However, these trends have been not examined quantitatively by the systematic study of the SNRs, in which the ejecta are separated from the ISM in spectra. Then, we try to study the ejecta distributions quantitatively and systematically in this section.

We firstly summarize the ionization parameters of Si and Fe ejecta of the Fe-K detected Galactic SNRs in figure 8.4. We find that in the core-collapse SNRs the ionization parameters of Si is about equal to those of Fe ($n_{\rm e}t[{\rm Si}] \simeq n_{\rm e}t[{\rm Fe}]$). On the other hand, in the Type Ia SNRs, the ionization parameters of Si is about 15 times larger than those of Fe ($n_{\rm e}t[{\rm Si}] \simeq 15 \times n_{\rm e}t[{\rm Fe}]$). Assuming the pressure equilibrium between Si and Fe ejecta,

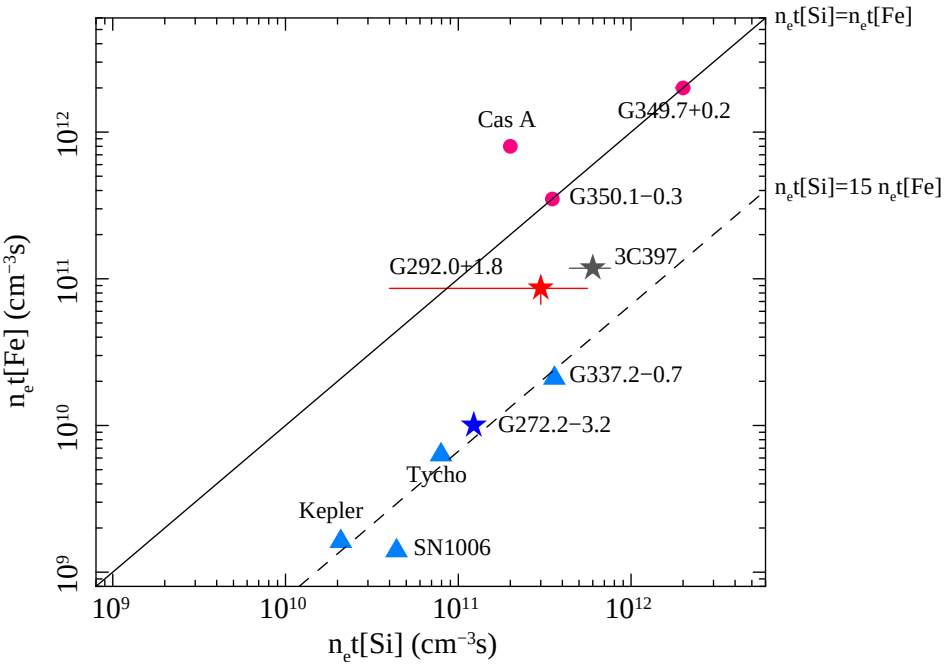

Figure 8.4: Ionization parameters of Si and Fe ejecta for Fe-K detected Galactic SNRs. The red and blue marks represent the data of core-collapse and Type Ia SNRs, respectively.

the electron densities ($n_{\rm e}$) are roughly common (but it may need a correction by the square root of the electron temperature ratio, typically ~ 1.4 from table 8.1). Thus the ionization parameters correspond the elapsed time after the arrival of the reverse shock at each ejecta. The relations between $n_{\rm e}t$[Si] and $n_{\rm e}t$[Fe] suggest that the Fe ejecta are more concentrated at the center than Si in the Type Ia SNRs, while in the core-collapse SNRs both of the ejecta are co-existing at same regions. This is the direct evidence the ejecta stratification of Type Ia SNRs. Interestingly, in Cas A, the ionization of Fe is more proceeded than Si. It may be because that we referred the $n_{\rm e}t$[Fe] of the Fe-rich knot in the southeast. In this region, the Fe is apparently more extent toward the outer region than Si. This irregularity against the onion-like structure expected in a progenitor star causes the high ionization values of Fe.

8.4 Discovery of the Recombining Plasma

In the core-collapse SNR, G290.1−0.8, we discovered the recombining plasma (RP). So far, ten RP SNRs were reported by the *Suzaku* observations as show in table 8.2. In this section, we discuss the origin of the RP by the systematical study on these SNRs.

Physical parameters of RPs

Most of the SNRs in which the RPs were discovered are the mixed-morphology SNRs. They have a abnormal morphology with center concentrated X-rays againt radio shells. These SNRs tend to be old ($> 10000\,\mathrm{yr}$) and locate in dense ISM environments. As seen in table 8.2, most of the RP SNRs show OH maser emission (1720 MHz) which is the direct evidence of the interaction between the SNR shock and molecular clouds. GeV/TeV γ-ray emissions are also detected in these SNRs. Therefore, it is guessed that such a dense and complex environment contributes to the birth of a RP.

Most of RP SNRs show enhanced metal abundances as seen in table 8.2. It might suggest that RPs are characteristic for the ejecta. In W49B, IC443, 3C391, and N49, the ejecta are spectrally separated from the ISM component (Sato et al. 2014; Uchida et al. 2015; and also see Appendix A and B). In all of these SNRs, the ejecta are RPs, whereas the ISMs are CIE plasmas. However, we note that it is difficult to accurately measure the ionization state of the ISM because the ISM component is largely suppressed by the interstellar absorption due to its low electron temperature. In fact, the ISM temperatures in these SNRs are $\sim$2 times smaller than those of the ejecta.

The same temperature difference between the ISM and the ejecta is expected in the other SNRs in which the ejecta is not separated from the ISM. In these SNRs, the temperatures of main components, maybe the ejecta, are relatively small ($kT_\mathrm{e} \sim 0.5\,\mathrm{keV}$), then the ISM components ($kT_\mathrm{e} \sim 0.2\,\mathrm{keV}$) are almost obscured. It may be the reason why the mixed-morphology SNRs have no shell structure in X-rays.

Table 8.2: List of the RP SNRs with their physical parameters.

Name	$N_{\rm H}$	$kT_{\rm init}$	$kT_{\rm e}$	$n_{\rm e}t$	Abundance	$n_{\rm e}$	$M_{\rm RP}$[a]	Volume[a]	Age	OH maser	γ-ray emission	Refs[b]
	(10^{22}cm^{-2})	(keV)	(keV)	(10^{11}cm^{-3}s)	(solar)	(cm^{-3})	($M_\odot$)	(10^{58} cm^3)	(kyr)			
W49B	5.05 ± 0.02	5	1.30 ± 0.01	5.18 ± 0.07	10–50	1.0	28	3.45	1–3	—	Yes	1, 2
IC443	0.542 ± 0.004	5	0.65 ± 0.01	5.53 ± 0.05	1–3	0.8	2.5*	0.35*	4-30	Yes	Yes	3, 4, 5
W28	0.470 ± 0.008	3	$0.40^{+0.01}_{-0.02}$	6.31	~ 0.2	1.1	3.8*	0.3*	$\sim$40	Yes	Yes	6
W44	1.3 ± 0.1	$1.07^{+0.05}_{-0.04}$	0.48 ± 0.01	6.76 ± 0.30	1–2	7.3	54*	0.66*	$\sim$20	Yes	Yes	7
3C391	3.13 ± 0.08	$1.8^{+1.0}_{-0.4}$	0.495 ± 0.009	$14.0^{+0.9}_{-1.3}$	~ 1	2.5	10–25	2.4	?	Yes	Yes	8
G290.1−0.8	0.78 ± 0.02	> 1.9	$0.52^{+0.01}_{-0.02}$	$10.6^{+0.4}_{-1.2}$	1–3	0.5	30	17	20–50	—	Yes	9
G346.6−0.2	2.3 ± 0.1	5	$0.30^{+0.02}_{-0.01}$	$4.8^{+0.1}_{-0.2}$	0.5–1	?	?	8.1	?	Yes	—	10
G348.5+0.1	3.5 ± 0.1	5	$0.49^{+0.05}_{-0.04}$	13^{+2}_{-1}	1–3	0.82	100	11	$\sim$10	Yes	Yes	11
G359.1−0.5	2.0 ± 0.2	$0.87^{+0.09}_{-0.07}$	0.29 ± 0.01	< 4.42	3–15	0.1	58	53	> 10	Yes	Yes	12
N49	0.351 ± 0.002	11 ± 1	0.62 ± 0.01	$7.00^{+0.27}_{-0.01}$	1–1.5	0.4	38	8.3	4–5	—	—	13

a The asterisks (*) indicate the SNRs whose masses and volumes are limited by the FoV of XIS and not the whole values.

b References: (1) Ozawa et al. (2009), (2) Appendix A, (3) Yamaguchi et al. (2009), (4) Ohnishi et al. (2014), (5) Appendix B, (6) Sawada & Koyama (2012), (7) Uchida et al. (2012), (8) Sato et al. (2014), (9) Kamitsukasa et al. (2015b) (This work), (10) Yamauchi et al. (2013), (11) Yamauchi et al. (2014), (12), Ohnishi et al. (2011), (13) Uchida et al. (2015)

Formation Process of RPs

In the recombining SNRs, the electron temperature kT_e is lower than the ionization temperature kT_Z ($kT_e < kT_Z$), against the expected relation ($kT_e > kT_Z$) in the standard SNRs. There are two ideas for the formation process of RP: the selective ionization and the electron cooling. In the former process, the ionization is advanced independently to the electron temperature, while in the latter process, only the electron temperature is dropped down.

In order to resolve which process is correct, we compare the distributions of electron temperature kT_e and ionization parameter $n_e t$ of four RP SNRs, W49B, IC443, W44, and G290.1−0.8, in figure 8.6. The data of W44 are obtained from Uchida et al. (2012), while those of W49B and IC443 are derived from the analyses in Appendix A and B. Since the ionization parameter $n_e t$ of RPs represents the timescale from the sudden creation of RPs, the lower $n_e t$ corresponds to the stronger RP. We can see the trend that the strength of the RPs becomes higher at lower electron temperatures. It clearly suggests that the RP is formed with the electron cooling process. We therefore focus on the models for the electron cooling in the followings.

Two major scenarios are considered for the electron cooling process (figure 8.5).

1. Thermal conduction: Cold molecular clouds interacting with the SNR shock wave cool down the plasma through the thermal conduction (Kawasaki et al. 2002).

2. Adiabatic rarefaction: The shock wave propagates from the dense CSM to the rarefied ISM. Then the rapid adiabatic cooling occurs (Itoh & Masai 1989; Yamaguchi et al. 2009).

(a) Thermal conduction (b) Adiabatic rarefaction

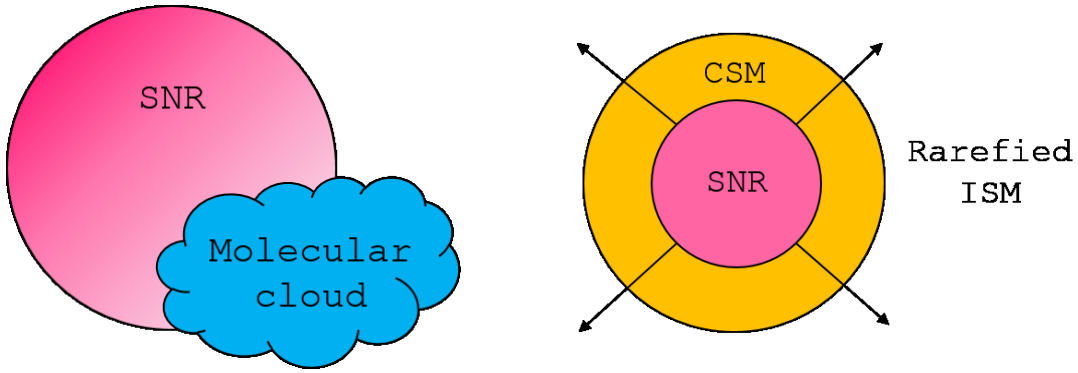

Figure 8.5: Schematic views of possible formation processes of a recombining plasma.

Due to their formation mechanisms, the key to the identification is the correlation between the circumstellar environments and the distributions of RPs. In the case of the thermal conduction, the RP is expected to become strong toward the molecular clouds, while vice-versa in the adiabatic rarefaction.

We therefore compare the distribution of the ISM and the RPs in figure 8.6, and discover the strong correlation between them. The strengths of RPs ($kT_{\rm Z}/kT_{\rm e}$) become higher toward the locations of OH masers or γ-ray emissions, which are the evidence of shocked molecular clouds. Accordingly, we conclude that the thermal conduction scenario is the origin of RPs.

Kawasaki et al. (2002) estimated the conduction timescale between two components as follows,

$$t_{\rm cond} \simeq 5000 \left(\frac{n_{\rm e}}{1\,{\rm cm}^{-3}}\right) \left(\frac{l_T}{10^{19}\,{\rm cm}}\right)^2 \left(\frac{kT_{\rm init}}{1\,{\rm keV}}\right)^{-5/2} \left(\frac{\ln\Lambda}{32.2}\right) {\rm yr} \tag{8.1}$$

where l_T is the distance from the approximate radius of the high-temperature plasma to the edge of the remnant, while $\ln\lambda$ is the Coulomb logarithm appropriate for $T > 4.2 \times 10^5\,{\rm K}$. We assume typical values for $n_{\rm e}$, $kT_{\rm init}$, and l_T from table 8.2. The conduction timescale is smaller than the ages of the RP SNRs except W49B, in which the initial temperature $kT_{\rm init}$ is expected higher than the current temperature ($kT_{\rm e} = 1.5\,{\rm keV}$). The recombining timescale, on the other hand, is given as

$$t_{\rm recomb} \simeq 24000 \left(\frac{n_{\rm e}}{1{\rm cm}^{-3}}\right)^{-1} {\rm yr} \tag{8.2}$$

which is enough larger than the conduction timescale. Thus the thermal conduction is possible to produce RPs.

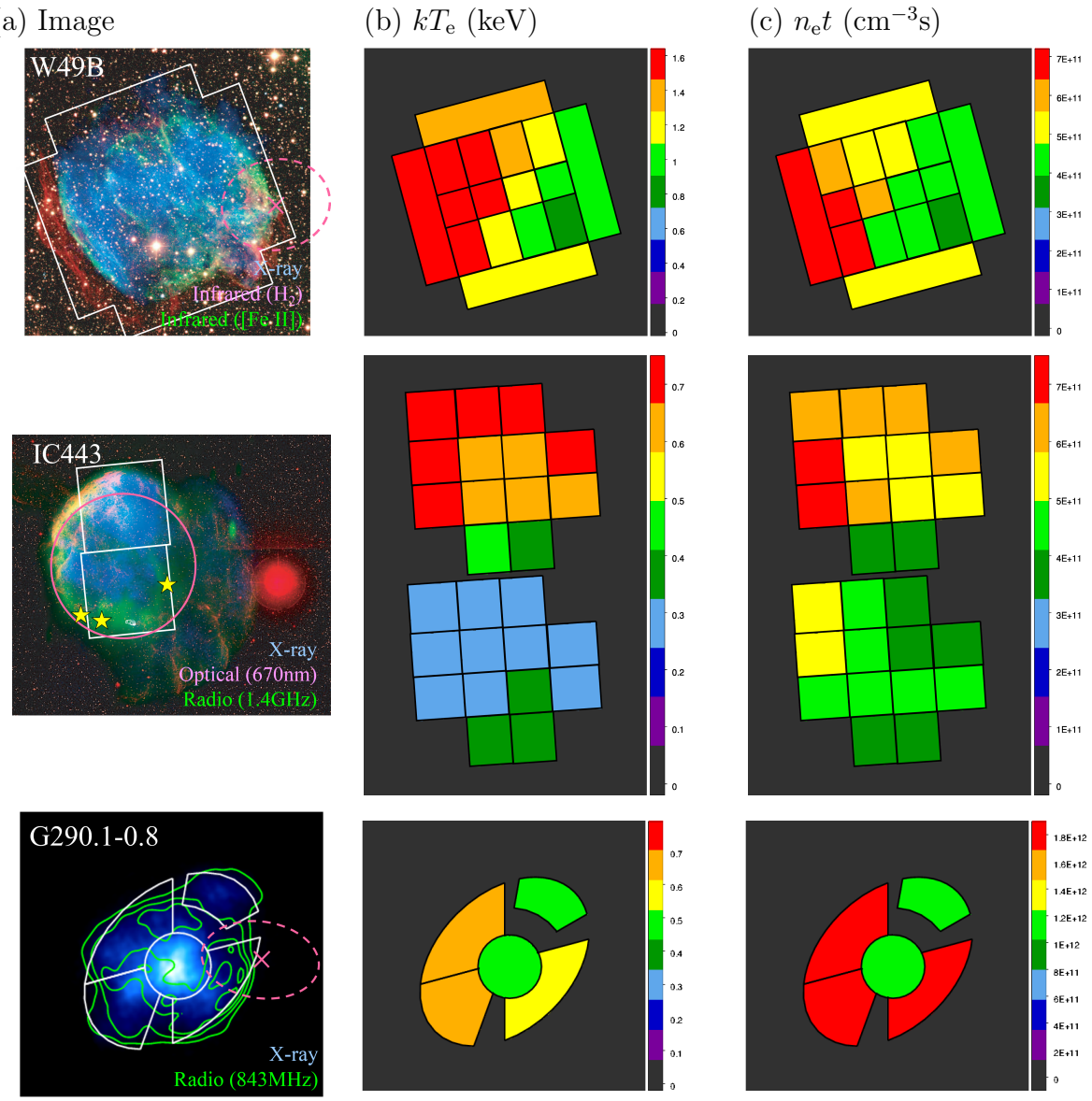

Figure 8.6: Spatial correlation between the molecular clouds and the RPs. Column (a): multi-wavelength images of RP SNRs (W49B: Keohane et al. 2007, IC443: Gaensler et al. 2006). The yellow marks and magenta lines represent the OH masers and GeV emission (dashed lines: 95% error circle, solid lines: extended emission), respectively. Column (b): the distributions of the electron temperatures kT_e. Column (c): the distribution of the ionization parameter n_et. For G290.1−0.8, we assume the large ionization parameters ($> 10^{13}cm^{-3}s$) in the IP regions.

Chapter 9

Conclusion

We have performed the X-ray study on the ejecta of the Galactic SNRs, G292.0+1.8, G290.1−0.8, G272.2−3.2, and 3C397, utilizing the high spectral resolution and sensitivity of the *Suzaku*/XIS. The important results obtained from our analyses are summarized as follows:

1. We have successfully separated the ejecta from the ISM in the broadband spectra of G292.0+1.8 and G272.2−3.2. The abundances and masses of these ejecta indicate the core-collapse and Type Ia origins, respectively. We have also shown that the spectrum of 3C397 is well represented with a two-component model. However, we can not specify the progenitor type because the abundances of light elements favor a core-collapse origin, while those of heavy elements favor a Type Ia origin.

2. Combining our results with previous studies on other Galactic SNRs, we confirmed that the abundances of light elements relative to intermediate mass elements in core-collapse SNRs are 10 times larger than those in Type Ia SNRs. The ejecta masses of core-collapse SNRs are about $10\,M_{\odot}$, while those of Type Ia SNRs are about $1\,M_{\odot}$.

3. The ionization ages of the Fe ejecta in the Type Ia SNRs are 15 times smaller than those of the Si ejecta, while those in the core-collapse SNRs are roughly equal to each other. It indicates that the ejecta of Type Ia SNRs keeps the stratified structures, while those of core-collapse SNRs are well mixed by the convection that maybe due to a hydrodynamical instability.

4. We discover a recombining plasma (RP) in the ejecta dominant region of the core-collapse SNR, G290.1−0.8. Including other RP SNRs discovered so far, we investigate a correlation between the distributions of RPs and ISMs. We then find that the

RPs become prominent toward the contact regions with cold molecular clouds. The plasma temperatures also decrease toward the contact regions. These facts suggest that the RPs are formed by a thermal conduction cooling with molecular clouds.

Appendix A

Analysis of W49B

A.1 Observation and Data Reduction

We analyze the *Suzaku* data of W49B summarized in table A.1. We merged these two data sets because the pointing positions are almost the same. Three of XISs were operated in the normal full-frame clocking mode with a SCI technique. The XIS data were reprocessed with the CALDB released in 2014 February. We used the HEASOFT version 6.16 for the data reduction and XSPEC for the spectral analysis. The total exposure time after the standard screening is 114 ks.

Table A.1: Observation log of W49B.

Target	Obs. ID	Obs. Date	R.A. (J2000.0)	Dec. (J2000.0)	Exposure (ks)
W49B	503084010	2009-March-29	$19^{h}11^{m}8.3^{s}$	$9\,^{\circ}6\,'56.5\,''$	52.2
W49B	504035010	2009-March-31	$19^{h}11^{m}8.3^{s}$	$9\,^{\circ}6\,'55.1\,''$	61.8

A.2 Analyses and Results

Figure A.1 shows the XIS image of W49B in the energy band of 1–10 keV. We generate the source spectrum from the circular region (Whole) with a radius of $3'$, subtracting the relevant NXB. We also extract the background spectrum from the FoV of XIS, excluding the source region and the calibration source regions, and subtract the NXB from it. We then subtract the background spectrum from the source spectrum. The resultant spectrum is shown in figure A.2. The spectrum has K-shell lines of Si, S, Ar, Ca, Cr, Mn, Fe, and Ni. It also shows a strong RRC structure of Fe around 9 keV, which strongly suggests that the plasma is in a recombining phase.

Table A.2: Best-fit parameters for the Whole region spectrum of W49B.

Component	Parameter	Value
Absorption	$N_{\rm H}$ ($10^{22}{\rm cm}^{-2}$)	5.05 ± 0.02
RNEI	$kT_{\rm init}$ (keV)	5 (fixed)
	$kT_{\rm e}$ (keV)	1.30 ± 0.01
	Si	12.0 ± 1.1
	S	18.7 ± 1.7
	Ar	21.4 ± 2.0
	Ca	24.4 ± 2.3
	Cr	44.0 ± 5.0
	Mn	53.0 ± 9.9
	Fe	21.7 ± 2.1
	Ni	18.4 ± 3.4
	$n_{\rm e}t$ ($10^{11}{\rm s\,cm}^{-3}$)	5.18 ± 0.07
	EM ($10^{12}{\rm cm}^{-5}$)	3.29 ± 0.28
APEC	$kT_{\rm e}$ (keV)	0.58 ± 0.01
	All elements	1 (fixed)
	EM ($10^{12}{\rm cm}^{-5}$)	23.0 ± 1.0
χ^2_ν (d.o.f.)		1.8 (5052)

We firstly apply a RP model (RNEI) with interstellar absorption. In this model, the column density $N_{\rm H}$, the electron temperature $kT_{\rm e}$ and ionization timescale $n_{\rm e}t$ are free parameters, whereas the initial electron temperature $kT_{\rm init}$ is fixed at 5 keV. The abundances of Si, S, Ar, Ca, Cr, Mn, Fe, and Ni are also free parameters. However, this model is not statistically acceptable with χ^2_ν (d.o.f.) = 2.5 (5122) (figure A.2 panel (a)). The main residuals are found in the energy band below 2 keV. Therefore, we add a CIE model (APEC) with solar abundances. This model largely improves the fit with χ^2_ν (d.o.f.) = 1.8 (5052) (figure A.2 panel (b)). Although this model also shows residuals at the K-shell lines of S (2.47 keV) and Fe (6.65 keV), the structure of the residuals indicate that the line width of the model is larger than that of the observed spectrum. We suspect that the residuals are due to the calibration error of the energy resolution of XIS. In fact, we obtain no significant improvement by adding further components or by changing the trial model. We thus adopt this model as the best approximation. The best-fit parameters are given in table A.2.

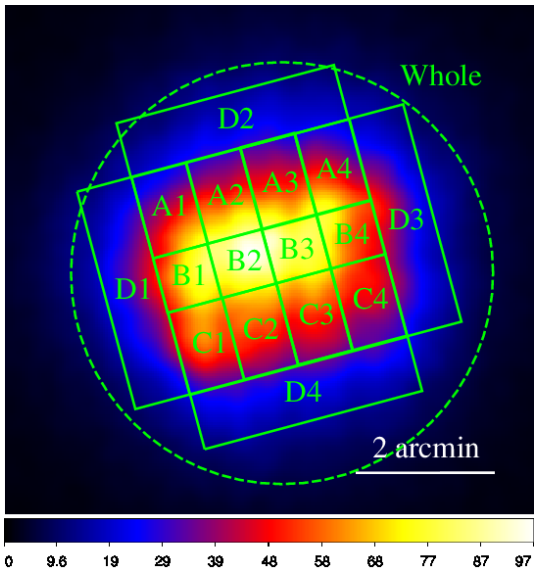

Figure A.1: XIS image of W49B in the energy band of 1–10 keV. The spectral extraction regions are shown with the green lines.

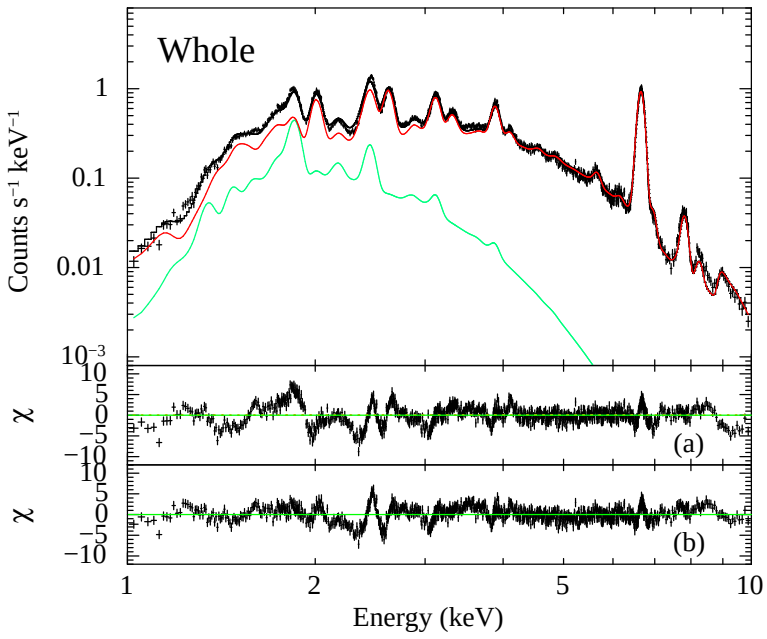

Figure A.2: Whole region spectrum (FI) of W49B. The spectrum is fitted with the model of RNEI (red) + APEC (green). The lower panels represent the residuals from the source models of (a) RNEI and (b) RNEI + APEC, respectively.

We next perform the spatially resolved analysis of W49B in order to examine the distribution of RP. We divide the SNR into 16 segmented regions as shown in figure A.1. The extracted spectra are shown in figure A.3. We analyze the spectra with the same model as Whole region. The fit results are statistically acceptable for all the regions (χ^2_ν =1.0–1.2). The best-fit electron temperatures and ionization parameters are summarized in figure A.4.

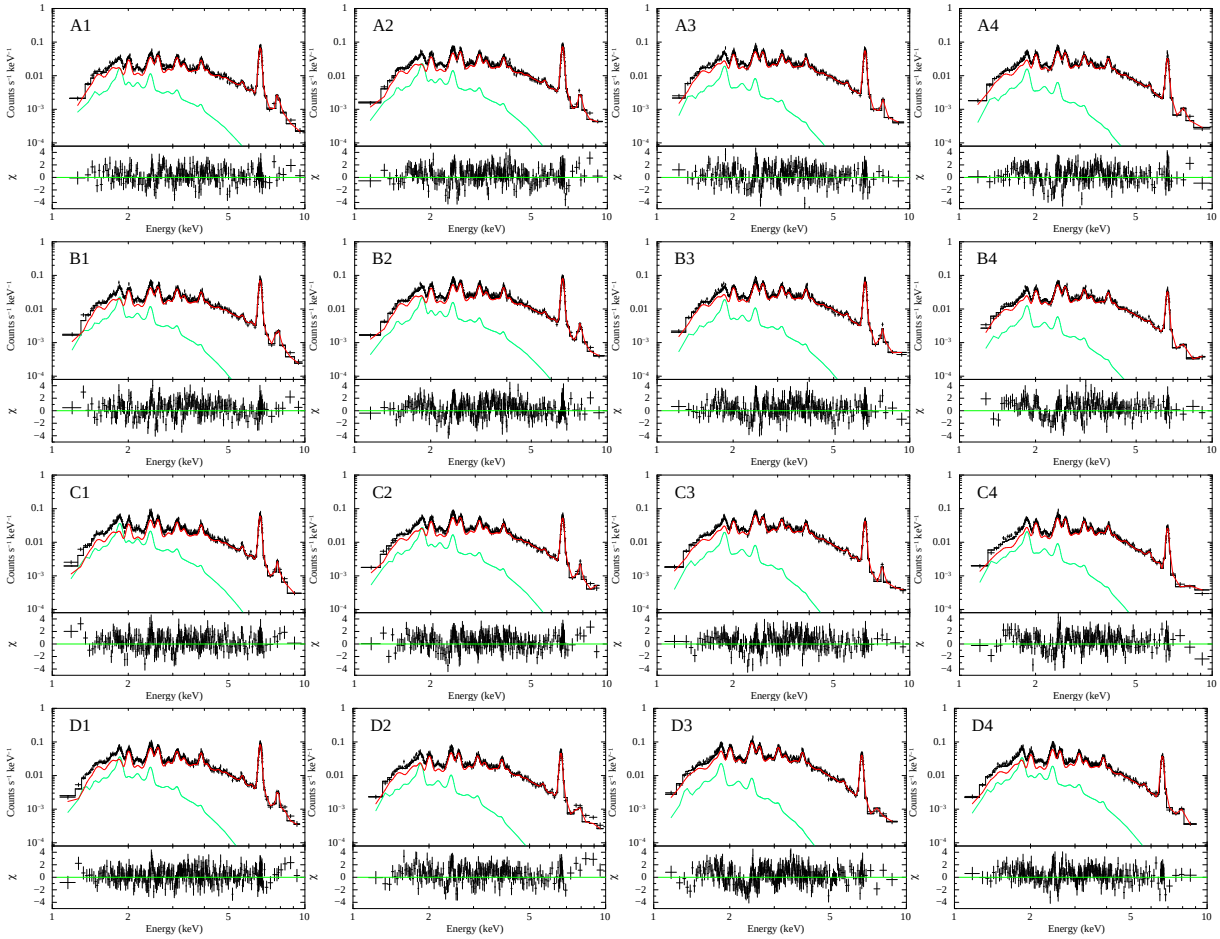

Figure A.3: Spatially resolved spectra (FI) of W49B. The spectrum is fitted with the same model in figure A.2.

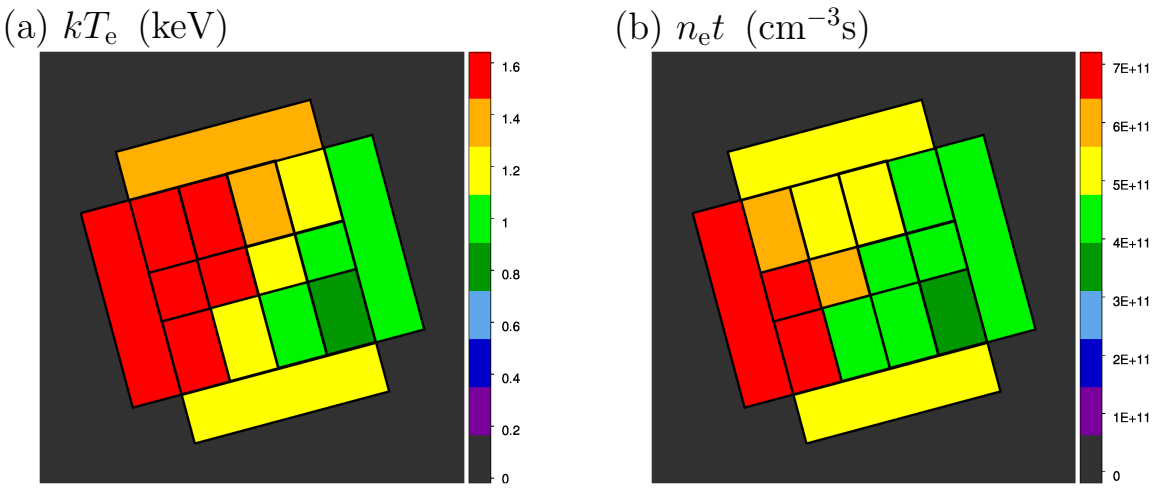

Figure A.4: Color maps representing the best-fit values of (a) electron temperature and (b) ionization parameter.

Appendix B

Analysis of IC443

B.1 Observation and Data Reduction

We analyze the *Suzaku* data of IC443 summarized in table B.1. Three of XISs were operated in the normal full-frame clocking mode with a SCI technique. The XIS data were reprocessed with the CALDB released in 2014 February. We used the HEASOFT version 6.16 for the data reduction and XSPEC for the spectral analysis. The total exposure time of the first and second observations, after the standard screening, are 42 ks and 44 ks, respectively.

Table B.1: Observation log of IC443.

Target	Obs. ID	Obs. Date	R.A.	Dec.	Exposure
			(J2000.0)		(ks)
IC443	501006010	2007-March-6	$6^{h}17^{m}11.4^{s}$	$22\,^{\circ}46\,'32.5\,''$	42.0
IC443	501006020	2007-March-7	$6^{h}17^{m}11.3^{s}$	$22\,^{\circ}28\,'46.9\,''$	44.0

B.2 Analyses and Results

Figure B.1 shows the XIS images of W49B in the energy bands of 0.8–3 keV and 3–7 keV. Contrary to the extended emission of 0.8–3 keV band, the 3–7 keV band image shows the point source like emission. It corresponds to the pulsar wind nebula (PWN) G189.2+2.9 (Gaensler et al. 2006).

We generate the source spectrum from the circular region (Circle) show in figure B.1 left, subtracting the relevant NXB. The resultant spectrum is shown in figure B.2. The spectrum has K-shell lines of O, Ne, Mg, Si, S, Ar, Ca, and Fe. All of these structures

come from the remnant because the X-ray background except the CXB is enough smaller than the SNR emission in this field.

We firstly apply a RP model (RNEI) with interstellar absorption. In this model, the column density $N_{\rm H}$, the electron temperature $kT_{\rm e}$ and ionization timescale $n_{\rm e}t$ are free parameters, but the initial electron temperature $kT_{\rm init}$ is fixed at 5 keV. The abundances of O, Ne, Mg, Si, S, Ar, Ca, and Fe are also free parameters, whereas that of Ni is tied to that of Fe. However, this model is not statistically acceptable with χ^2_ν (d.o.f.) = 3.3 (2817) (figure B.2 panel (a)). The main residuals are found in the energy band below 1 keV. Therefore, we add a CIE model (APEC) with solar abundances. This model largely improves the fit with χ^2_ν (d.o.f.) = 1.7 (2700) (figure B.2 panel (b)). Although this model is still statistically unacceptable, we obtain no significant improvement by adding further components or by changing the trial model. We thus adopt this model as the best approximation. The best-fit parameters are given in table B.2.

We also examine the spectrum of the PWN, G189.2+2.9, in IC443. We generate the PWN spectrum and the local BG spectrum from the ellipse region and the surrounding box region in figure B.1, respectively, subtracting the relevant NXBs. Then, we subtract the local BG from the PWN spectrum. Figure B.3 shows the resultant spectrum. The spectrum is well fitted with the absorbed power-law. The photon index and unabsorbed flux are 1.75 ± 0.04 and $(5.88 \pm 0.12) \times 10^{-12}$ ergs cm^{-2} s^{-1}, roughly consistent with those estimated by Gaensler et al. (2006).

We next perform the spatially resolved analysis of IC443 in order to examine the distribution of RP. We divide the SNR into 26 segmented regions as shown in figure B.1 left. The extracted spectra are shown in figure B.4. We analyze the spectra with the same model as Whole region, but we add the PWN component. The fit results are statistically acceptable for all the regions (χ^2_ν =1.0–1.4). The best-fit electron temperatures and ionization parameters are summarized in figure B.5.

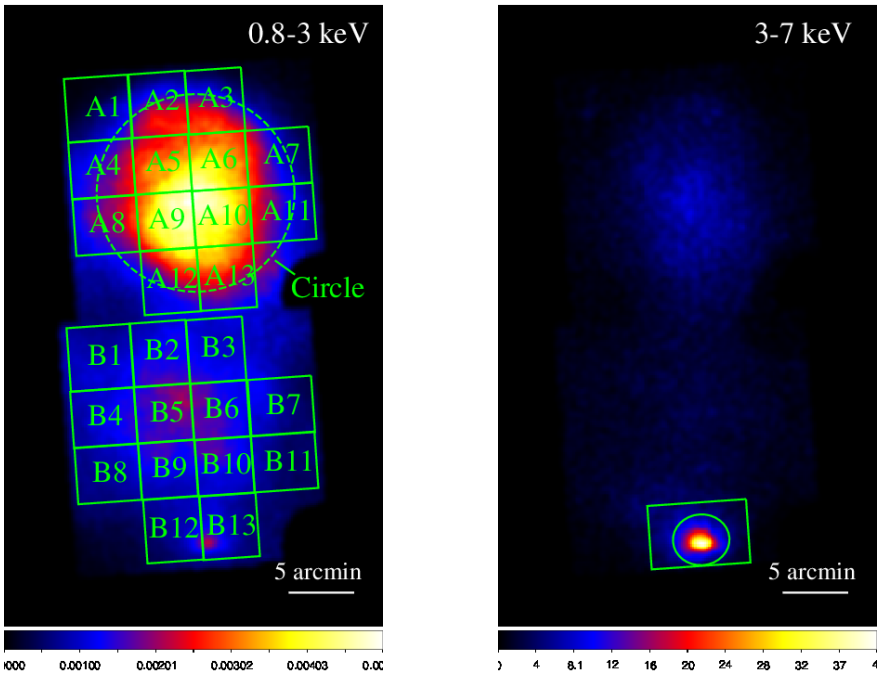

Figure B.1: XIS images of IC443 in the energy bands of 0.8–3 keV (left) and 3–7 keV (right). The spectral extraction regions are shown with the green lines.

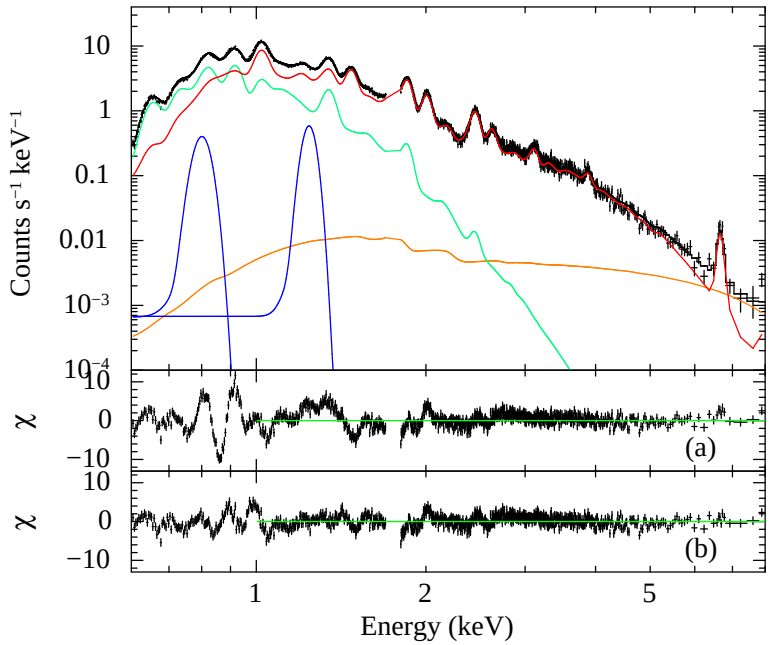

Figure B.2: Circle region spectrum (FI) of IC443. The spectrum is fitted with the model of RNEI (red) + APEC (green) in addition to the CXB (orange) and Gaussian lines (blue). The lower panels represent the residuals from the source models of (a) RNEI and (b) RNEI + APEC, respectively.

Table B.2: Best-fit parameters for the bright-region spectrum of IC443.

Component	Parameter	Value
Absorption	$N_{\rm H}$ ($10^{21}{\rm cm}^{-2}$)	5.42 ± 0.04
RNEI	$kT_{\rm init}$ (keV)	5 (fixed)
	$kT_{\rm e}$ (keV)	0.65 ± 0.01
	O	0.91 ± 0.25
	Ne	2.32 ± 0.20
	Mg	1.34 ± 0.11
	Si	1.67 ± 0.13
	S	2.14 ± 0.17
	Ar	1.29 ± 0.12
	Ca	1.00 ± 0.15
	Fe (= Ni)	0.38 ± 0.03
	$n_{\rm e}t$ ($10^{11}{\rm s\,cm}^{-3}$)	5.53 ± 0.05
	EM ($10^{13}{\rm cm}^{-5}$)	1.10 ± 0.10
APEC	$kT_{\rm e}$ (keV)	0.257 ± 0.003
	All elements	1 (fixed)
	EM ($10^{13}{\rm cm}^{-5}$)	1.96 ± 0.07
χ^2_ν (d.o.f.)		1.7 (2700)

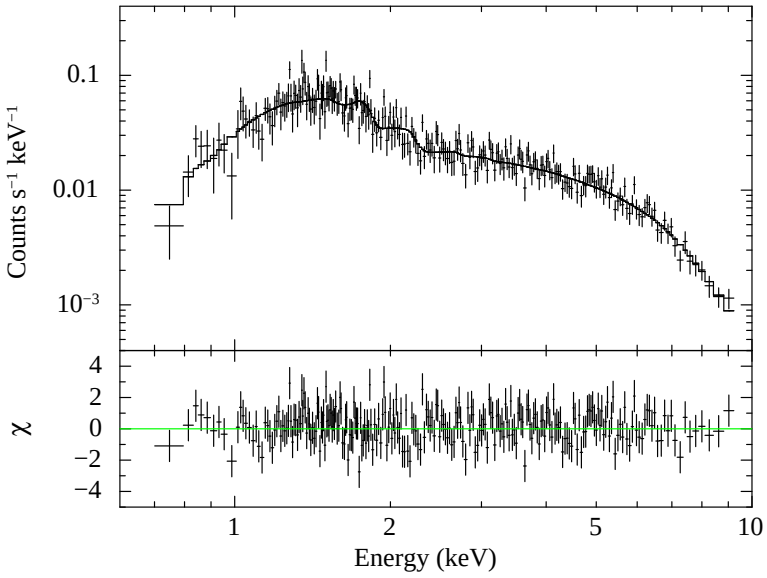

Figure B.3: Spectrum (FI) of the PWN G189.2+2.9 The spectrum is fitted by the power-law with the interstellar absorption. The lower panels shows the residual.

Table B.3: Best-fit parameters for the spectrum of the PWN G189.2+2.9.

Component	Parameter	Value
Absorption	$N_{\rm H}$ ($10^{21}{\rm cm}^{-2}$)	5.27 ± 0.37
Power-law	Photon index	1.75 ± 0.04
	Absorbed flux*	5.62 ± 0.11
	Unabsorbed flux*	5.88 ± 0.12
χ^2_ν (d.o.f.)		0.96 (722)

* Flux (10^{-12} ergs cm^{-2} s^{-1}) in the 2–10 keV.

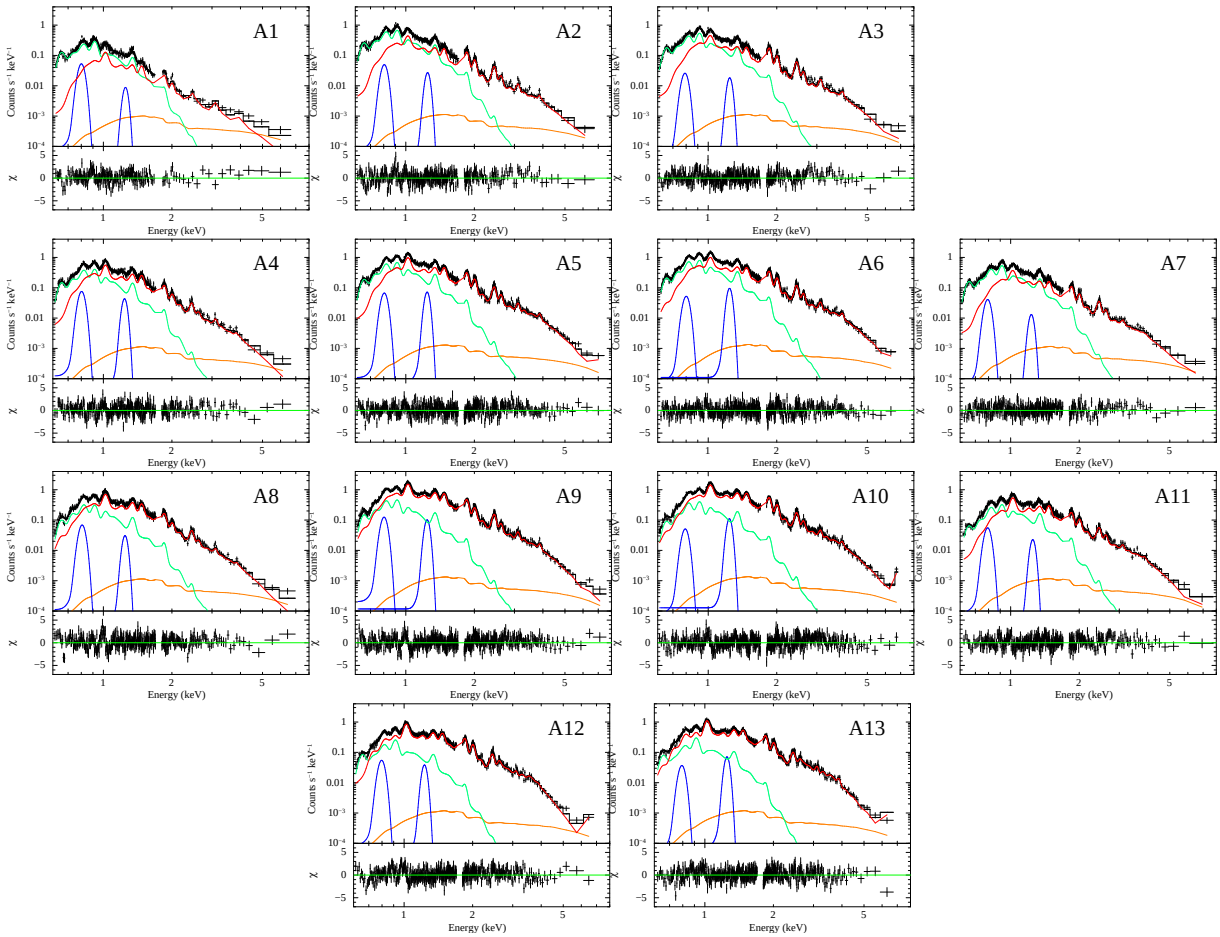

Figure B.4: Spatially resolved spectra (FI) of IC443. The spectrum is fitted with the same model in figure B.2, but added the PWN component (cyan).

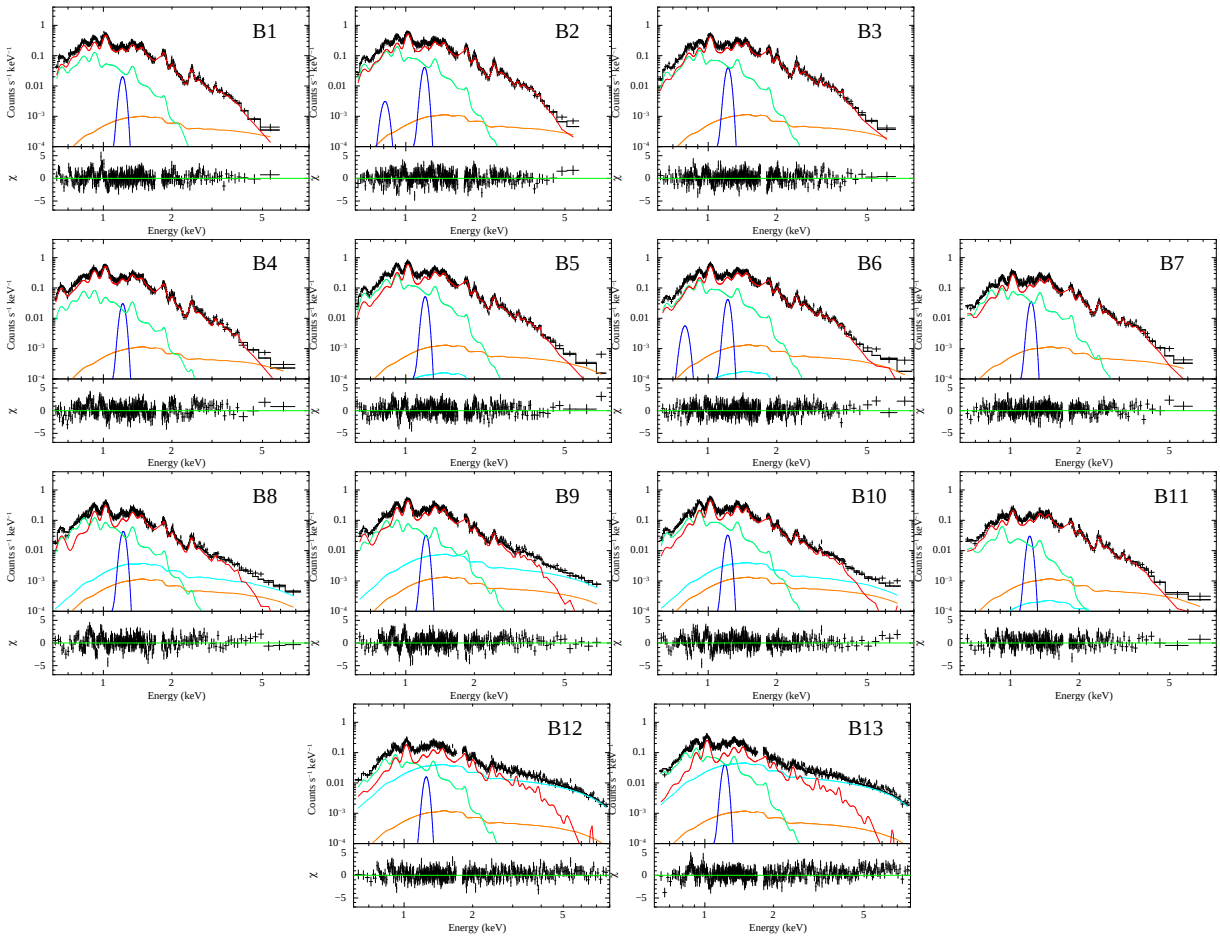

Figure B.4: Continued.

(a) $kT_{\rm e}$ (keV) (b) $n_{\rm e}t$ ($\rm cm^{-3}s$)

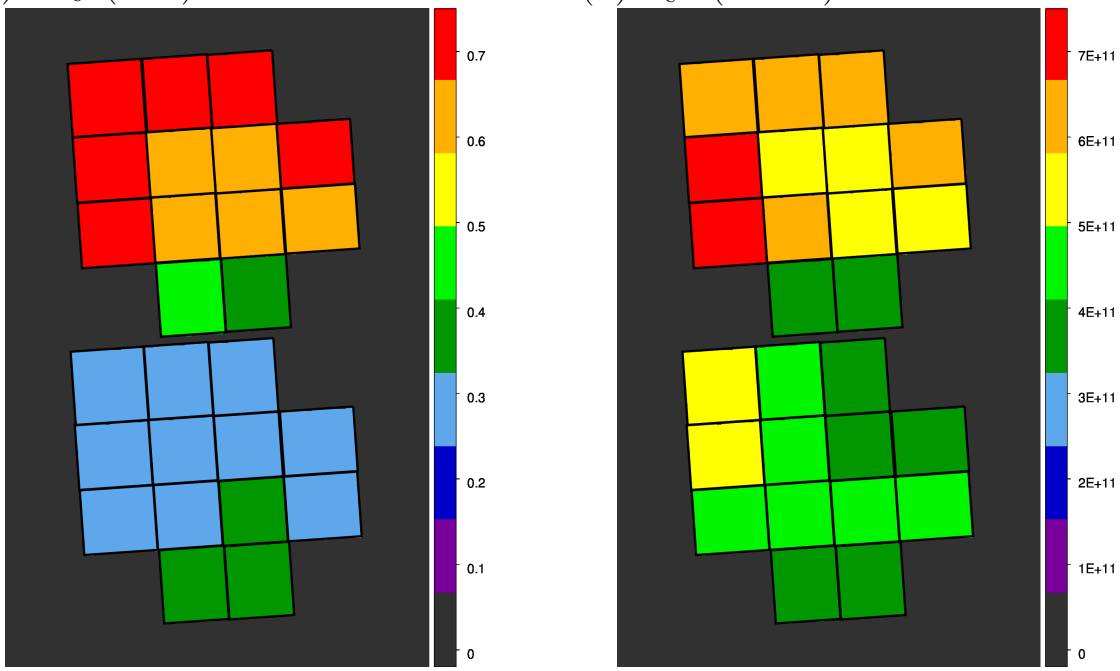

Figure B.5: Color maps representing the best-fit values of (a) electron temperature and (b) ionization parameter.

Acknowledgment

This work is supported by many collaborators. First of all, I express my deep gratitude to Prof. Hiroshi Tsunemi and Prof. Emer. Katsuji Koyama for their continuous guidance and encouragement throughout my graduate course. I have learned a lot from them, not only the basis of X-ray astronomy, but also the attitude toward the research and science.

I also greatly appreciate to Dr. Kiyoshi Hayashida. He has continuously guided me from my undergraduate period. I also owe a very important debt to the SNR team members, Drs. Hiroshi Nakajima, Koji Mori, Satoru Katsuda, and Hiroyuki Uchida, for invaluable guidances, comments, and discussions.

I would like to thank all the members of the X-ray astronomy group in Osaka University, especially to Drs. Naohisa Anabuki, Ryo Nagino, Hiroaki Takahashi, and Shutaro Ueda. Dr. Shutaro Ueda (now in ISAS/JAXA) gave me many "strict" guidances and comments (sometimes I misunderstood him.). Finally, I thank the *Suzaku* satellite, the XIS, and all the members of the *Suzaku* Science Working Group. This work is also supported by JSPS Research Fellowship for Young Scientists.

References

Abdo, A. A., Ackermann, M., Ajello, M., et al. 2010, ApJ, 712, 459

Allen, G. E., Chow, K., DeLaney, T., et al. 2015, ApJ, 798, 82

Arnett, W. D. 1969, Ap&SS, 5, 180

Aschenbach, B. 2002, in Society of Photo-Optical Instrumentation Engineers (SPIE) Conference Series, Vol. 4496, X-Ray Optics for Astronomy: Telescopes, Multilayers, Spectrometers, and Missions, ed. P. Gorenstein & R. B. Hoover, 8–22

Auchettl, K., Slane, P., Castro, D., Foster, A. R., & Smith, R. K. 2015, ApJ, 810, 43

Beiersdorfer, P., Phillips, T., Jacobs, V. L., et al. 1993, ApJ, 409, 846

Bionta, R. M., Blewitt, G., Bratton, C. B., Casper, D., & Ciocio, A. 1987, Physical Review Letters, 58, 1494

Blondin, J. M., Mezzacappa, A., & DeMarino, C. 2003, ApJ, 584, 971

Borkowski, K. J., Hendrick, S. P., & Reynolds, S. P. 2006, ApJ, 652, 1259

Borkowski, K. J., Lyerly, W. J., & Reynolds, S. P. 2001, ApJ, 548, 820

Brinkman, A. C., Gunsing, C. J. T., Kaastra, J. S., et al. 2000, ApJ, 530, L111

Burke, B. E., Mountain, R. W., Daniels, P. J., Cooper, M. J., & Dolat, V. S. 1993, in Society of Photo-Optical Instrumentation Engineers (SPIE) Conference Series, Vol. 2006, EUV, X-Ray, and Gamma-Ray Instrumentation for Astronomy IV, ed. O. H. Siegmund, 272–285

Burrows, A., Livne, E., Dessart, L., Ott, C. D., & Murphy, J. 2006, ApJ, 640, 878

Burrows, A., Livne, E., Dessart, L., Ott, C. D., & Murphy, J. 2007, ApJ, 655, 416

Camilo, F., Gaensler, B. M., Gotthelf, E. V., Halpern, J. P., & Manchester, R. N. 2004, ApJ, 616, 1118

Camilo, F., Manchester, R. N., Gaensler, B. M., & Lorimer, D. R. 2002, ApJ, 579, L25

Caswell, J. L., Murray, J. D., Roger, R. S., Cole, D. J., & Cooke, D. J. 1975, A&A, 45, 239

Chen, Y., Sun, M., Wang, Z.-R., & Yin, Q. F. 1999, ApJ, 520, 737

Chevalier, R. A. 1974, ApJ, 188, 501

Chevalier, R. A. 1982, ApJ, 258, 790

Cioffi, D. F., McKee, C. F., & Bertschinger, E. 1988, ApJ, 334, 252

Cordes, J. M., & Lazio, T. J. W. 2002, ArXiv Astrophysics e-prints, astro-ph/0207156

Dodson, R., Legge, D., Reynolds, J. E., & McCulloch, P. M. 2003, ApJ, 596, 1137

Doggett, J. B., & Branch, D. 1985, AJ, 90, 2303

Duncan, A. R., Stewart, R. T., Campbell-Wilson, D., et al. 1997, MNRAS, 289, 97

Dwarkadas, V. V., & Chevalier, R. A. 1998, ApJ, 497, 807

Dyer, K. K., & Reynolds, S. P. 1999, ApJ, 526, 365

Filipovic, M. D., Payne, J. L., & Jones, P. A. 2005, Serbian Astronomical Journal, 170, 47

Filippenko, A. V. 1997, ARA&A, 35, 309

Gaensler, B. M., Chatterjee, S., Slane, P. O., et al. 2006, ApJ, 648, 1037

Gaensler, B. M., & Wallace, B. J. 2003, ApJ, 594, 326

García, F., Combi, J. A., Albacete-Colombo, J. F., et al. 2012, A&A, 546, A91

Gonzalez, M., & Safi-Harb, S. 2003, ApJ, 583, L91

Gonzalez, M. E., Kaspi, V. M., Pivovaroff, M. J., & Gaensler, B. M. 2006, ApJ, 652, 569

Goss, W. M., Shaver, P. A., Zealey, W. J., Murdin, P., & Clark, D. H. 1979, MNRAS, 188, 357

Green, D. A. 2014, Bulletin of the Astronomical Society of India, 42, 47

Greiner, J., & Egger, R. 1993, IAU Circ., 5709, 2

Greiner, J., Egger, R., & Aschenbach, B. 1994, A&A, 286, L35

H. E. S. S. Collaboration, Abramowski, A., Acero, F., et al. 2012, A&A, 541, A5

Halpern, J. P., Tomsick, J. A., Gotthelf, E. V., et al. 2014, ApJ, 795, L27

Harrus, I. M., Hughes, J. P., & Slane, P. O. 1998, ApJ, 499, 273

Harrus, I. M., Slane, P. O., Smith, R. K., & Hughes, J. P. 2001, ApJ, 552, 614

Henley, D. B., & Shelton, R. L. 2013, ApJ, 773, 92

Hirata, K., Kajita, T., Koshiba, M., Nakahata, M., & Oyama, Y. 1987, Physical Review Letters, 58, 1490

Hughes, J. P., Ghavamian, P., Rakowski, C. E., & Slane, P. O. 2003, ApJ, 582, L95

Hughes, J. P., & Singh, K. P. 1994, ApJ, 422, 126

Hughes, J. P., Slane, P. O., Burrows, D. N., et al. 2001, ApJ, 559, L153

Hughes, J. P., Hayashi, I., Helfand, D., et al. 1995, ApJ, 444, L81

Hwang, U., & Laming, J. M. 2012, ApJ, 746, 130

Hwang, U., Petre, R., & Flanagan, K. A. 2008, ApJ, 676, 378

Ilovaisky, S. A., & Lequeux, J. 1972, A&A, 18, 169

Ishisaki, Y., Maeda, Y., Fujimoto, R., et al. 2007, PASJ, 59, 113

Itoh, H., & Masai, K. 1989, MNRAS, 236, 885

Jiang, B., Chen, Y., Wang, J., et al. 2010, ApJ, 712, 1147

Kaastra, J. S., Mewe, R., & Nieuwenhuijzen, H. 1996, in UV and X-ray Spectroscopy of Astrophysical and Laboratory Plasmas, ed. K. Yamashita & T. Watanabe, 411–414

Kamitsukasa, F., Koyama, K., Nakajima, H., et al. 2015a, PASJ, arXiv:1510.05265

Kamitsukasa, F., Koyama, K., Uchida, H., et al. 2015b, PASJ, 67, 16

Kamitsukasa, F., Koyama, K., Tsunemi, H., et al. 2014, PASJ, 66, 64

Kaneda, H., Makishima, K., Yamauchi, S., et al. 1997, ApJ, 491, 638

Kargaltsev, O., & Pavlov, G. G. 2008, in American Institute of Physics Conference Series, Vol. 983, 40 Years of Pulsars: Millisecond Pulsars, Magnetars and More, ed. C. Bassa, Z. Wang, A. Cumming, & V. M. Kaspi, 171–185

Katsuda, S., Hwang, U., Petre, R., et al. 2010, ApJ, 714, 1725

Katsuda, S., Mori, K., Tsunemi, H., et al. 2008a, ApJ, 678, 297

Katsuda, S., Tsunemi, H., & Mori, K. 2008b, ApJ, 678, L35

Katsuda, S., Mori, K., Maeda, K., et al. 2015, ArXiv e-prints, arXiv:1506.03135

Kawasaki, M. 2003, PhD thesis, Tokyo University

Kawasaki, M. T., Ozaki, M., Nagase, F., et al. 2002, ApJ, 572, 897

Kelley, R. L., Mitsuda, K., Allen, C. A., et al. 2007, PASJ, 59, 77

Keohane, J. W., Reach, W. T., Rho, J., & Jarrett, T. H. 2007, ApJ, 654, 938

Kesteven, M. J., & Caswell, J. L. 1987, A&A, 183, 118

Kesteven, M. J. L. 1968, Australian Journal of Physics, 21, 739

Khokhlov, A. M. 1991, A&A, 245, 114

Kishishita, T., Hiraga, J., & Uchiyama, Y. 2013, A&A, 551, A132

Koyama, K., Tsunemi, H., Dotani, T., et al. 2007, PASJ, 59, 23

Kushino, A., Ishisaki, Y., Morita, U., et al. 2002, PASJ, 54, 327

Lallement, R., Vergely, J.-L., Valette, B., et al. 2014, A&A, 561, A91

Lee, J.-J., Park, S., Hughes, J. P., & Slane, P. O. 2014, ApJ, 789, 7

Lee, J.-J., Park, S., Hughes, J. P., et al. 2010, ApJ, 711, 861

Lewis, K. T., Burrows, D. N., Hughes, J. P., et al. 2003, ApJ, 582, 770

Liebendörfer, M., Mezzacappa, A., Thielemann, F.-K., et al. 2001, Phys. Rev. D, 63, 103004

Lopez, L. A., Ramirez-Ruiz, E., Badenes, C., et al. 2009, ApJ, 706, L106

Lopez, L. A., Ramirez-Ruiz, E., Huppenkothen, D., Badenes, C., & Pooley, D. A. 2011, ApJ, 732, 114

Lu, F. J., & Aschenbach, B. 2000, A&A, 362, 1083

Lumb, D. H., Gondoin, P., Turner, M. J., et al. 2000, in Society of Photo-Optical Instrumentation Engineers (SPIE) Conference Series, Vol. 4140, X-Ray and Gamma-Ray Instrumentation for Astronomy XI, ed. K. A. Flanagan & O. H. Siegmund, 22–31

Lyne, A. G., & Lorimer, D. R. 1994, Nature, 369, 127

Maeda, K., Röpke, F. K., Fink, M., et al. 2010, ApJ, 712, 624

Masai, K. 1984, Ap&SS, 98, 367

Matsumoto, H., Nakajima, H., Yamaguchi, H., et al. 2006, in Society of Photo-Optical Instrumentation Engineers (SPIE) Conference Series, Vol. 6266, Society of Photo-Optical Instrumentation Engineers (SPIE) Conference Series, 41

McEntaffer, R. L., Grieves, N., DeRoo, C., & Brantseg, T. 2013, ApJ, 774, 120

McKee, C. F. 1974, ApJ, 188, 335

McKee, C. F., & Ostriker, J. P. 1977, ApJ, 218, 148

Mendoza, C., Kallman, T. R., Bautista, M. A., & Palmeri, P. 2004, A&A, 414, 377

Milne, D. K., Caswell, J. L., Kesteven, M. J., Haynes, R. F., & Roger, R. S. 1989, Proceedings of the Astronomical Society of Australia, 8, 187

Minkowski, R. 1941, PASP, 53, 224

Mitsuda, K., Bautz, M., Inoue, H., et al. 2007, PASJ, 59, 1

Muno, M. P., Clark, J. S., Crowther, P. A., et al. 2006, ApJ, 636, L41

Nakashima, S., Nobukawa, M., Uchida, H., et al. 2013, ApJ, 773, 20

Nomoto, K., Thielemann, F.-K., & Yokoi, K. 1984, ApJ, 286, 644

Ohnishi, T., Koyama, K., Tsuru, T. G., et al. 2011, PASJ, 63, 527

Ohnishi, T., Uchida, H., Tsuru, T. G., et al. 2014, ApJ, 784, 74

Ozawa, M., Koyama, K., Yamaguchi, H., Masai, K., & Tamagawa, T. 2009, ApJ, 706, L71

Palmeri, P., Mendoza, C., Kallman, T. R., Bautista, M. A., & Meléndez, M. 2003, A&A, 410, 359

Pannuti, T. G., Allen, G. E., Filipović, M. D., et al. 2010, ApJ, 721, 1492

Park, S., Hughes, J. P., Slane, P. O., et al. 2007, ApJ, 670, L121

Park, S., Hughes, J. P., Slane, P. O., et al. 2004, ApJ, 602, L33

Park, S., Roming, P. W. A., Hughes, J. P., et al. 2002, ApJ, 564, L39

Pavan, L., Bozzo, E., Pühlhofer, G., et al. 2011, A&A, 533, A74

Pavan, L., Bordas, P., Pühlhofer, G., et al. 2014, A&A, 562, A122

Petruk, O. 2001, A&A, 371, 267

Porquet, D., Mewe, R., Dubau, J., Raassen, A. J. J., & Kaastra, J. S. 2001, A&A, 376, 1113

Rampp, M., & Janka, H.-T. 2000, ApJ, 539, L33

Reynoso, E. M., Green, A. J., Johnston, S., et al. 2003, MNRAS, 345, 671

Reynoso, E. M., Johnston, S., Green, A. J., & Koribalski, B. S. 2006, MNRAS, 369, 416

Rho, J., & Petre, R. 1998, ApJ, 503, L167

Ruiz, M. T., & May, J. 1986, ApJ, 309, 667

Rybicki, G. B., & Lightman, A. P. 1979, Radiative processes in astrophysics

Safi-Harb, S., Dubner, G., Petre, R., Holt, S. S., & Durouchoux, P. 2005, ApJ, 618, 321

Safi-Harb, S., Petre, R., Arnaud, K. A., et al. 2000, ApJ, 545, 922

Sánchez-Ayaso, E., Combi, J. A., Bocchino, F., et al. 2013, A&A, 552, A52

Sato, T., Koyama, K., Takahashi, T., Odaka, H., & Nakashima, S. 2014, PASJ, 66, 124

Sawada, M., & Koyama, K. 2012, PASJ, 64, 81

Sedov, L. I. 1959, Similarity and Dimensional Methods in Mechanics

Serlemitsos, P. J., Soong, Y., Chan, K.-W., et al. 2007, PASJ, 59, 9

Seward, F. D. 1990, ApJS, 73, 781

Sezer, A., & Gök, F. 2012, MNRAS, 421, 3538

Shelton, R. L., Cox, D. P., Maciejewski, W., et al. 1999, ApJ, 524, 192

Slane, P., Chen, Y., Schulz, N. S., et al. 2000, ApJ, 533, L29

Slane, P., Smith, R. K., Hughes, J. P., & Petre, R. 2002, ApJ, 564, 284

Slane, P., Hughes, J. P., Temim, T., et al. 2012, ApJ, 749, 131

Stehle, M., Mazzali, P. A., Benetti, S., & Hillebrandt, W. 2005, MNRAS, 360, 1231

Suchy, S., Pottschmidt, K., Rothschild, R. E., et al. 2011, ApJ, 733, 15

Sumiyoshi, K., Yamada, S., Suzuki, H., et al. 2005, ApJ, 629, 922

Takahashi, T., Abe, K., Endo, M., et al. 2007, PASJ, 59, 35

Takata, A., Nobukawa, M., Uchida, H., et al. 2015, PASJ, doi:10.1093/pasj/psv025

Tammann, G. A., Loeffler, W., & Schroeder, A. 1994, ApJS, 92, 487

Tanaka, K. 1986, PASJ, 38, 225

Taylor, J. H., & Cordes, J. M. 1993, ApJ, 411, 674

Thompson, T. A., Burrows, A., & Pinto, P. A. 2003, ApJ, 592, 434

Uchida, H., Koyama, K., & Yamaguchi, H. 2015, ApJ, 808, 77

Uchida, H., Yamaguchi, H., & Koyama, K. 2013, ApJ, 771, 56

Uchida, H., Koyama, K., Yamaguchi, H., et al. 2012, PASJ, 64, 141

Uchiyama, H., Nobukawa, M., Tsuru, T. G., & Koyama, K. 2013, PASJ, 65, 19

Uchiyama, Y., Maeda, Y., Ebara, M., et al. 2008, PASJ, 60, 35

Vink, J. 2012, A&A Rev., 20, 49

Wang, C.-Y., & Chevalier, R. A. 2002, ApJ, 574, 155

Webbink, R. F. 1984, ApJ, 277, 355

Weiler, K. W., & Panagia, N. 1978, A&A, 70, 419

Weisskopf, M. C., Brinkman, B., Canizares, C., et al. 2002, PASP, 114, 1

Wheeler, J. C., Meier, D. L., & Wilson, J. R. 2002, ApJ, 568, 807

Whelan, J., & Iben, Jr., I. 1973, ApJ, 186, 1007

White, R. L., & Long, K. S. 1991, ApJ, 373, 543

Winkler, P. F., Twelker, K., Reith, C. N., & Long, K. S. 2009, ApJ, 692, 1489

Wolter, H. 1952, Annalen der Physik, 445, 286

Woosley, S. E., & Weaver, T. A. 1994, ApJ, 423, 371

Woosley, S. E., & Weaver, T. A. 1995, ApJS, 101, 181

Yamaguchi, H., Koyama, K., & Uchida, H. 2011, PASJ, 63, 837

Yamaguchi, H., Ozawa, M., Koyama, K., et al. 2009, ApJ, 705, L6

Yamaguchi, H., Koyama, K., Katsuda, S., et al. 2008, PASJ, 60, 141

Yamaguchi, H., Badenes, C., Petre, R., et al. 2014, ApJ, 785, L27

Yamaguchi, H., Badenes, C., Foster, A. R., et al. 2015, ApJ, 801, L31

Yamauchi, S., Minami, S., Ota, N., & Koyama, K. 2014, PASJ, 66, 2

Yamauchi, S., Nobukawa, M., Koyama, K., & Yonemori, M. 2013, PASJ, 65, 6

Yang, X. J., Tsunemi, H., Lu, F. J., & Chen, L. 2009, ApJ, 692, 894

Yang, X. J., Tsunemi, H., Lu, F. J., et al. 2013, ApJ, 766, 44

Yasumi, M., Nobukawa, M., Nakashima, S., et al. 2014, PASJ, 66, 68

Yusef-Zadeh, F., Wardle, M., Rho, J., & Sakano, M. 2003, ApJ, 585, 319

Zeldovich, Y. B., & Raizer, Y. P. 1966, Elements of gasdynamics and the classical theory of shock waves